INCLUSIVE PRODUCTION OF THE $\rho^{\pm}(770)$ MESON IN HADRONIC DECAYS OF THE Z^0 BOSON

Ph.D. Thesis

in

Engineering Physics

University of Gaziantep

Supervisor

Assoc. Prof. Dr. Ayda BEDDALL

Co-supervisor: Assist. Prof. Dr. Andrew BEDDALL

By

Ahmet BİNGÜL

April 2007

Approval of the Graduate School of Natural and Applied Sciences.

Prof. Dr. Sadettin ÖZYAZICI
Director

I certify that this thesis satisfies all the requirements as a thesis for the degree of Doctor of Philosophy.

Prof. Dr. Zihni ÖZTÜRK
Head of Department

This is to certify that we have read this thesis and that in our opinion it is fully adequate, in scope and quality, as a thesis for the degree of Doctor of Philosophy.

Assoc. Prof. Dr. Ayda BEDDALL
Co-supervisor: Assist. Prof. Dr. Andrew BEDDALL
Major Supervisor

Examining Committee Members:

Prof. Dr. Engin ARIK _____

Prof. Dr. Gülsen ÖNENGÜT _____

Assoc. Prof. Dr. Gülay TOHUMOĜLU _____

Assoc. Prof. Dr. Ramazan KOÇ _____

Assoc. Prof. Dr. Ayda BEDDALL _____

ABSTRACT

INCLUSIVE PRODUCTION OF THE $\rho^{\pm}(770)$ MESON
IN HADRONIC DECAYS OF THE Z^0 BOSON

BİNGÜL, Ahmet

Ph.D. in Engineering Physics

Supervisor: Assoc. Prof. Dr. Ayda BEDDALL
Co-supervisor: Assist. Prof. Dr. Andrew BEDDALL

April 2007, 143 pages

The inclusive production rate of the charged vector meson $\rho^{\pm}(770)$ in hadronic Z decays is measured with the ALEPH detector at the LEP collider. A total of 3,239,746 hadronic events are selected from data recorded by ALEPH from the 1991 to 1995 running periods. Decays of $\rho^{\pm} \rightarrow \pi^0 + \pi^{\pm}$ are reconstructed for $x_E > 0.05$ and $x_p > 0.05$ where $x_E = E_\rho / E_{beam}$ and $x_p = p_\rho / p_{beam}$. The $\rho^{\pm}$ multiplicity per hadronic event is evaluated to be:

$$\langle N_{\rho^{\pm}} \rangle = 2.59 \pm 0.03 \pm 0.15 \pm 0.04$$

where the first error is statistical and the second systematic. The third error is from the extrapolation to the $x_p = x_E = 0$. The rates and differential cross-section are compared with Monte Carlo model predictions and OPAL measurements.

Key words: $\rho^{\pm}$ meson production, ALEPH, LEP, hadronic Z decays.

ÖZET

Z^0 BOZONU'NUN HADRONİK BOZUNUMUNDA
$\rho^{\pm}(770)$ MEZONU ÖLÇÜMÜ

BİNGÜL, Ahmet

Doktora Tezi, Fiz. Müh.

Tez Yöneticisi: Doç. Dr. Ayda BEDDALL
Tez Yönetici Yardımcısı: Yrd. Doç. Dr. Andrew BEDDALL

Nisan 2007, 143 sayfa

Bu çalısmada, LEP'teki ALEPH detektöründe, hadronik Z bozunumlarından elde edilen yüklü $\rho^{\pm}(770)$ vektör mezonunun üretim hızı ölçüldü. 1991 ve 1995 yılları arasında ALEPH detektörü ile kaydedilen toplam 3,239,746 hadronik olay seçildi. $\rho^{\pm} \rightarrow \pi^0 + \pi^{\pm}$ bozumumları $x_E > 0.05$ and $x_p > 0.05$ deĝerleri icin bir araya getirildi; burada $x_E = E_\rho / E_{demet}$ ve $x_p = p_\rho / p_{demet}$ şeklindedir. Hadronik olay başına $\rho^{\pm}$ mezonun bolluĝu:

$$\langle N_{\rho^{\pm}} \rangle = 2.59 \pm 0.03 \pm 0.15 \pm 0.04$$

olarak hesaplandı. Burada birinci hata istatiksel, ikincisi sistematiktir. Üçüncü hata hesaplanmayan $x_p = x_E = 0$ deĝerleri için tahminde yapılan hatadır. Ölçülen üretim hızı ve diferansiyel tesir kesitleri Monte Carlo öngörüleri ve OPAL grubunun sonuçları ile karşılaştırıldı.

Anahtar kelimeler: $\rho^{\pm}$ mezon üretimi, LEP, hadronik Z bozunumları.

To my wife Meltem and our daughter Gülcenur

ACKNOWLEDGEMENTS

I would like to thank Assoc. Prof. Dr. Ayda Beddall and Assist. Prof. Dr. Andrew Beddall for their support and guidance during the preparation of this thesis.

Special thanks to my wife Meltem for her spiritual support.

TABLE OF CONTENTS

CHAPTER

1 INTRODUCTION 1

2 THEORY 4
2.1 The Standard Model 4
2.2 Quantum Chromodynamics 6
2.3 Hadron Production in Z Decays 6
2.3.1 The Electroweak Phase 8
2.3.2 Perturbative QCD 8
2.3.3 Hadronisation 9
2.3.4 Hadron Decays 15
2.4 Bose-Einstein Correlations 15

3 APPARATUS 17
3.1 Introduction 17
3.2 Large Electron-Positron Collider (LEP) 17
3.2.1 Beam Injection and Acceleration 19
3.3 Particle Detectors 20
3.4 The ALEPH Detector 21
3.4.1 Overview 21
3.4.2 The Central Tracking Chambers 23
3.4.3 The Principal Calorimeters 27
3.4.4 The Superconducting Solenoid 31
3.4.5 The Luminosity Monitors 31
3.4.6 ALEPH in Numbers 32
3.5 Trigger and Data Acquisition Systems 33
3.5.1 The Trigger System 33
3.5.2 The Data Acquisition System (DAQ) 34

4 EVENT RECONSTRUCTION AND SIMULATION 36
4.1 Introduction 36
4.2 Track Reconstruction 37
4.2.1 TPC Coordinate Determination 37
4.2.2 TPC Track Finding and Fitting 41
4.2.3 TPC-ITC-VDET Track Association 42
4.3 Ionisation Energy Loss 42
4.4 Calorimeter Reconstruction 42
4.5 Photon Reconstruction 43
4.5.1 G-clusters 43

4.5.2 Merged Photons . . . 45
4.5.3 Converted Photons . . . 45
4.6 Event Simulation . . . 46
4.6.1 KINGAL . . . 46
4.6.2 GALEPH . . . 46

5 EVENT SELECTION 48
5.1 Data Quality . . . 48
5.2 Hadronic Event Selection . . . 49
5.2.1 Track Cuts . . . 50
5.2.2 Event Cuts . . . 55
5.3 Event Background . . . 55

6 TRACK SELECTION FOR THE ANALYSIS 59
6.1 Introduction . . . 59
6.2 Charged Track Selection . . . 59
6.2.1 Impact Parameters . . . 60
6.2.2 Transverse Momentum . . . 61
6.2.3 Ionisation Energy Loss . . . 61
6.3 Neutral Pion Selection . . . 64
6.3.1 π^0 Reconstruction . . . 64
6.3.2 Photon Selection . . . 65
6.3.3 π^0 Energy . . . 66
6.3.4 π^0 Topology . . . 66
6.3.5 π^0 Mass Window . . . 67
6.3.6 π^0 Ranking . . . 67
6.3.7 π^0 Mass Constraint . . . 68
6.4 Reconstruction Performances . . . 69
6.4.1 Momentum and Energy Distributions . . . 69
6.4.2 Pion Purity . . . 70
6.4.3 Pion Efficiency . . . 70
6.4.4 Momentum and Energy Resolution . . . 73

7 π^0 CALIBRATION 75
7.1 Introduction . . . 75
7.2 Calibration . . . 75
7.3 Corrections . . . 80
7.4 Calibration Performance . . . 84

8 THE RANKING METHOD 85
8.1 Introduction . . . 85
8.2 π^0 Reconstruction . . . 85
8.3 The Standard Method . . . 86
8.4 π^0 Estimators . . . 87
8.5 Ranking . . . 90
8.6 Performance of the Ranking Method . . . 92
8.6.1 π^0 Estimator Effect . . . 92
8.6.2 π^0 Energy . . . 93
8.6.3 Mass Window . . . 93

8.6.4 Invariant Mass 94
8.7 Example Applications 95

9 EXTRACTION OF THE $\rho^{\pm}(770)$ SIGNAL 97
9.1 Introduction 97
9.2 Two-Pion Invariant Mass 97
9.3 Signal Reconstruction 98
9.4 Signal Extraction and Fitting Procedure 100
9.4.1 Signal Shape 100
9.4.2 Combinatorial Background 105
9.4.3 Reflections 105
9.4.4 Interference with Coherent Background 106
9.4.5 Total Fit Function 110
9.4.6 Signal Extraction 110
9.5 Rates and the Differential Cross Section 110
9.6 Comparison of Data and Monte Carlo 114

10 SYSTEMATIC ERROR ANALYSIS 116
10.1 Introduction 116
10.2 Source of Systematic Errors 116
10.2.1 Track Selection Cuts 116
10.2.2 Fitting Procedure 118
10.2.3 Reflection Models 119
10.2.4 Signal Function 119
10.2.5 Efficiency Correction 119
10.2.6 Extrapolation to $x_p = 0$ and $x_E = 0$ 119
10.3 Summary of Errors 120

11 RESULTS AND CONCLUSION 122
11.1 Results 122
11.1.1 Rates and Differential Cross-sections 122
11.1.2 Total Multiplicity 122
11.1.3 Isospin Dependence 126
11.1.4 The Cross-Section as a Function of ξ_p 127
11.2 Summary 127
11.3 Conclusion 128
11.4 Future Work 129

REFERENCES 130

APPENDIX

A π^0 FORMULAE 133
A.1 Two-Photon Invariant Mass Formula 133
A.2 π^0 Mass Resolution Formula 134

B DESCRIPTION OF THE π^0 REFITTING METHODS 135
B.1 Refitting Low Energy π^0s 135
B.2 Refitting High Energy π^0s 135
B.3 Multidimensional Optimisation 136
B.3.1 The Method of Lagrange Multipliers 136
B.3.2 The Newtonian Method 137

C π^0 MATCHING 138

D DETAILED REAL DATA FITS 140

LIST OF TABLES

Table

2.1 Particles and forces of the Standard Model 5

3.1 Tracking momentum and impact parameter resolution 26
3.2 ALEPH in Numbers 32

5.1 Selected hadronic events from each year of data taking 48
5.2 Decay modes of the Z Boson 50
5.3 Events contributions obtained from Monte Carlo 58

6.1 Some $\rho^{\pm}$ sources and their $c\tau$ values 60

7.1 π^0 calibration, mass and width parameters 80

9.1 Scaled momentum and energy intervals and ranges. 98
9.2 Scale parameters s_p and s_E for each x_p and x_E bin 105

10.1 Summary of the track cuts 118
10.2 Mass bounds applied to fitting ranges 118
10.3 Some estimated values in Monte Carlo programs 120
10.4 Systematic and statistical errors for the $\rho^{\pm}$ rate for x_p intervals . . 121
10.5 Systematic and statistical errors for the $\rho^{\pm}$ rate for x_E intervals . 121

11.1 Rates and differential cross-sections for x_p intervals 123
11.2 Rates and differential cross-sections for x_E intervals 123
11.3 Comparison of rates and isospin dependence 126

LIST OF FIGURES

Figure

1.1 Total cross-section for $e^+e^- \rightarrow q\bar{q}$. 2

2.1 The hadronic cross-section as a function of centre-of-mass energy . 5
2.2 Schematic diagram of the reaction $e^+e^- \rightarrow \mathrm{Z} \rightarrow q\bar{q}$. 7
2.3 Hadron production in the Field-Feynman model. 10
2.4 The string and the cluster hadronisation models 11
2.5 Electric and color field lines. 12

3.1 Schematic view of LEP 18
3.2 LEP injection system 20
3.3 Schematic view of the ALEPH detector 22
3.4 Configuration of the original (1991) vertex detector 24
3.5 A view of the time-projection chamber 25
3.6 The arrangement of the TPC sectors 26
3.7 ECAL modules 28
3.8 ECAL lead/wire-chamber layers 28
3.9 Energy resolution of the ECAL. 30
3.10 A simplified outline of the DAQ system 35

4.1 The flow of data in the ALEPH experiment 37
4.2 Reconstruction of tracks from coordinates in the TPC 38
4.3 A TPC pad row cluster formed by two nearby tracks 39
4.4 TPC pad row subclusters formed by two nearby tracks 40
4.5 Helix parameters used in the TPC tracking algorithms 41
4.6 Energy deposits of photons in the ECAL 44

5.1 Polar angle of the event axis 49
5.2 Reconstruction of a typical hadronic event 51
5.3 Number of TPC coordinates for selected tracks 52
5.4 Polar angle for selected tracks 53
5.5 Transverse impact parameter for selected tracks 54
5.6 Longitudinal impact parameter for selected tracks 54
5.7 Transverse momentum for selected tracks 55
5.8 Charged energy versus charged multiplicity for events in real data 56
5.9 Charge distributions for selected events 56
5.10 Event flow 57

6.1 d_0 distributions for $\rho^{\pm}$, K^0_S, and photon conversions 61
6.2 Measured dE/dx versus particle momentum 62

6.3 χ(dE/dx) distributions according to the $\pi^{\pm}$ hypothesis 63
6.4 Invariant mass of photon pairs around a π^0 signal 64
6.5 Energy distribution for photons 65
6.6 Polar angle distribution of photons 66
6.7 Four π^0 topologies 67
6.8 Pion momentum and energy spectra 69
6.9 Charged pion purity 71
6.10 Neutral pion purity 71
6.11 Charged pion efficiency 72
6.12 Neutral pion efficiency 72
6.13 Charged particle resolution 73
6.14 π^0 E_{rec}/E_{tru} distribution 74
6.15 π^0 energy resolution 74

7.1 Moving π^0-peak positions 76
7.2 Example peak position 77
7.3 Calibration functions for π^0 mass 78
7.4 Calibration functions for π^0 width 79
7.5 Example peak difference 81
7.6 All peaks MC and RD 82
7.7 All peak differences MC and RD 83
7.8 π^0 calibration performance 84

8.1 Invariant mass spectra of photon pairs 87
8.2 Effect of varying the mass window in the standard method 88
8.3 χ^2 and photon pair opening angle (for each candidate) 89
8.4 Performance of π^0 estimators (mass window varying) 92
8.5 Comparison of two π^0 selection methods (energy varying) 93
8.6 Comparison of two π^0 selection methods (mass window varying) . 94
8.7 Two-photon invariant mass before and after Ranking 95
8.8 Three-pion invariant mass spectra 96
8.9 Two-pion invariant mass spectra 96

9.1 Scaled momentum and energy spectra and reconstruction efficiencies 99
9.2 BW and RBW shapes 101
9.3 Sample fits to both Monte Carlo signals 102
9.4 Variation of m_{res} and Γ_{res} 103
9.5 Ratio of full and partial signals 104
9.6 An example of a fit to a Monte Carlo signal 104
9.7 Combinatorial background and reflection models 107
9.8 Mass shift between real data and Monte Carlo mass spectra . . . 108
9.9 C values as a funtion of x_p and x_E 109
9.10 Two-pion mass spectra for interference term subtracted data . . . 109
9.11 Fitted mass spectra and contributions 111
9.12 Extracted signal and interference term from the mass spectra . . . 111
9.13 Fits to real data for x_p intervals 112
9.14 Fits to real data for x_E intervals 113
9.15 Ratio of ALEPH data to Monte Carlo rates 115
9.16 Ratio of ALEPH data to OPAL rates 115

11.1 Differential cross-section as a function of x_p 124
11.2 Differential cross-section as a function of x_E 125
11.3 Comparison of the rates and isospin dependence 126
11.4 Differential cross-section as a function of ξ_p 127

C.1 λ distribution in π^0 matching 139

D.1 Fits to the real data for all x_p intervals 140
D.2 Extracted signals for all x_p intervals 141
D.3 Fits to the real data for all x_E intervals 142
D.4 Extracted signals for all x_E intervals 143

LIST OF SYMBOLS

e^- : Electron

e^+ : Positron

$\pi^\pm$: Charged pi-meson

π^0 : Neutral pi-meson

$\rho^\pm$: Charged rho-meson

ρ^0 : Neutral rho-meson

γ : Photon

θ_{12} : Opening angle between photon 1 and 2

m : Particle mass; invariant mass

E : Particle energy

$\vec{p}$: Particle space momentum vector

ω : Omega vector meson

η : Eta meson

$K^{*\pm}$: Charged K^* meson

σ : Resolution(mass, spatial or energy); cross-section

R : Region size; stochastic constant; ranking estimator

$\oplus$: Quadratic sum

$\mathcal{L}$: Luminosity

χ : Chi-value

χ^2 : Chi-square value

λ : Chaoticity parameter; π^0 matching parameter

Γ_0 : Resonance nominal width at FWHM

ε : Efficiency

$\mathcal{P}$: Purity

CHAPTER 1

INTRODUCTION

In the standard model of elementary particle physics, quarks and leptons interact via the exchange of photons and intermediate vector bosons, as described by the Glashow-Weinberg-Salam standard model of weak interactions [1, 2, 3]. In addition, quarks are subject to the strong interaction, described by quantum chromodynamics (QCD) [4].

The area of interest for this analysis is the transformation of quarks and gluons into observable hadrons (parton fragmentation) in high energy reactions. This transformation is governed by QCD which is predictive in high energy processes where perturbation theory can be used. However, the final stage of the transformation (hadronisation) occurs at low energy where perturbation theory is no longer applicable, therefore phenomenological models are constructed to describe the hadronisation.

A clean environment for the study of fragmentation has been provided by the Large Electron Positron Collider (LEP) in which the process $e^+e^- \rightarrow Z \rightarrow q\bar{q}$ can be selected with little contamination from background processes. Measurements of the hadronic final state are made in order to test the fragmentation models: parameters in the models are tuned to reproduce observed distributions such as event shape variables, jet production rates, and particle production rates.

The area of analysis presented in this thesis is inclusive particle production. Many particle species have been measured in previous e^+e^- annihilation experiments and a number of Monte Carlo programs based on QCD have been tuned so that the measured rates were reproduced. A comprehensive compilation of experimental data on inclusive particle production in e^+e^- interactions can be found in [5].

Since the construction of LEP as a Z boson factory much progress has been made, particularly in the area of resonant states. In previous experiments resonances were measured with poor statistical precision and there were, in addition, some considerable systematic disagreements among experiments. The

higher statistics obtainable at LEP are illustrated by Figure 1.1, which shows the much larger hadronic cross-section compared to the lower energy colliders: with a comparable luminosity, LEP has experienced much higher reaction rates and since the startup of LEP in 1989 each of the four experiments, ALEPH, DELPHI, L3 and OPAL, has collected several million hadronic Z decays.

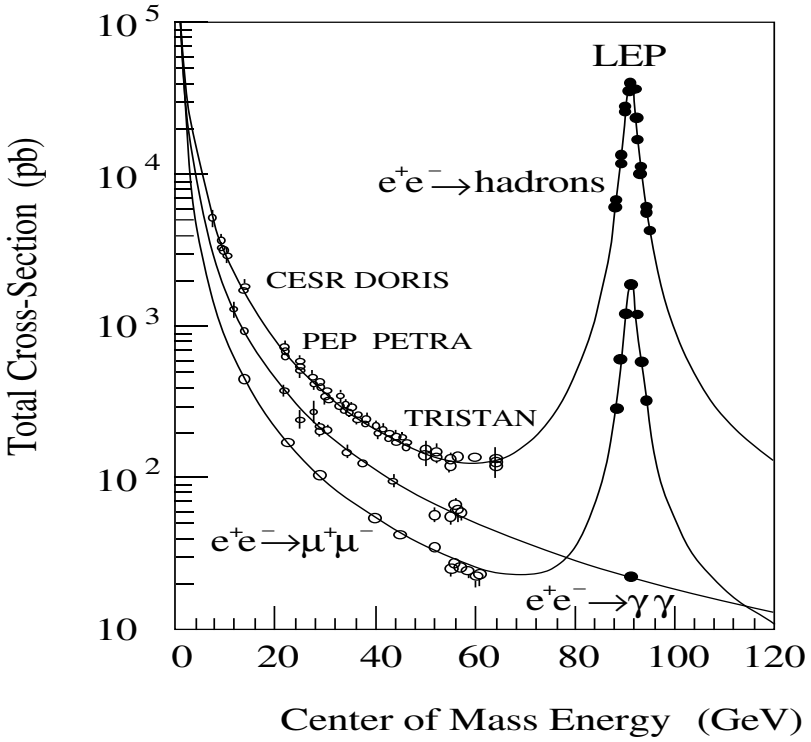

Figure 1.1: *Total cross-section for e^+e^- annihilation into hadrons and muon pairs as function of the centre-of-mass energy. Also given is the two-photon cross-section. Experimental data are compared with predictions from the standard model.*

More information can be gained by studying the production rates of resonances. Resonant states are particularly interesting because they are less likely than the lighter hadrons to be products of particle decays and therefore their dynamics are more closely related to those of the fragmenting partons. The light vector mesons are particularly well suited as they are copiously produced in hadronic events giving rise to a significant fraction of the observed stable particles. In addition, measurements of the vector mesons contribute to a more complete picture of particle production. Hence, the measurement of inclusive particle production cross sections of resonant states improve the description of the hadronisation process. The large sample of hadronic Z decays collected at LEP is ideal for this purpose.

This study presents the ALEPH measurement [6] of the rate and differential cross section of the $\rho(770)^{\pm}$ meson produced in hadronic Z decays. $\rho^{\pm}$ candidates are reconstructed from their daughter pions ($\rho^{\pm} \to \pi^0\pi^{\pm}$, BR $\approx 100\%$). The analysis described here is essentially similar to that of papers such as [7] and [8], and it is based on about 3.2 million selected hadronic events recorded by the ALEPH detector at centre-of-mass energies around $\sqrt{s} = 91.2\,\mathrm{GeV}$ in the running period of LEP between 1991 and 1995. The results of the evaluated rates and cross sections are compared with Monte Carlo programs JETSET 7.4, PYTHIA 6.4 and HERWIG 6.5, and the OPAL measurement which is the only other experiment at LEP to make this measurement.

This thesis includes a short summary of the Standard Model, a theoretical description of the fragmentation models and a brief description of the experimental apparatus including the data acquisition system, event reconstruction, and detector simulation. The analysis is presented in Chapters 5 to 10, and the results and conclusions are given in Chapter 11.

CHAPTER 2

THEORY

2.1 The Standard Model

The Standard Model is an attempt to describe the fundamental particles and their interactions. The model is a quantum field theory that includes the unified weak and electromagnetic interactions (electroweak) and the strong interactions (quantum chromodynamics). Gravity has not yet been included in the Standard Model; however, in the quantum world of particle interactions the effects of gravity are insignificant.

In the Standard Model the most fundamental particles in nature are divided into two groups: fermions and bosons. The two groups are summarised in Table 2.1. The fundamental fermions are spin-$\frac{1}{2}$ particles providing the building blocks of all matter, whilst the interactions between the fermions are provided by the exchange of bosons (spin-1); the electromagnetic interaction is mediated by photons, the weak interaction by the W^+,W^- and Z bosons, and the strong interaction by gluons. In addition, a Higgs boson is required to provide mass for the fermions and the Z and $W^\pm$ bosons.

Fermions can be further divided into two sub-groups: leptons which interact via the electroweak interaction, and quarks which in addition interact via the strong interaction. The leptons consist of the electron, the muon, the tau, and their corresponding neutrinos. The quarks and leptons can be arranged into groups, according to their coupling to the weak current, forming three generations. The three roes of fermions in Table 2.1 represent each generation, each containing heavier particles than its predecessor.

In the early running periods of LEP, the number of generations of light neutrinos was confirmed to be three. Figure 2.1 shows for ALEPH data from 1990 and 1991 the measured hadronic cross-section around the Z resonance. The theoretical predictions for two, three, and four generations of light neutrinos are shown. The data are consistent only with the hypothesis of three generations.

Table 2.1: *The particles and forces of the Standard Model.*

Fermions ($spin - \frac{1}{2}$)				*Bosons* ($spin$ 1)		
Quarks		*Leptons*		*em.*	*Weak*	*Strong*
u (*up*)	d (*down*)	e^-	ν_e	γ	$W^{\pm}$, Z	*gluons*(8)
c (*charm*)	s (*strange*)	μ^-	ν_μ			
t (*top*)	b (*bottom*)	τ^-	ν_τ			

Combining the data from the four LEP experiments a recent value for the number of light neutrino generations is 2.994 ± 0.012 [9]. However, whilst all known neutrinos are believed to have zero or negligible mass, the measurements do not rule out a fourth generation neutrino of mass greater than $M_Z/2$.

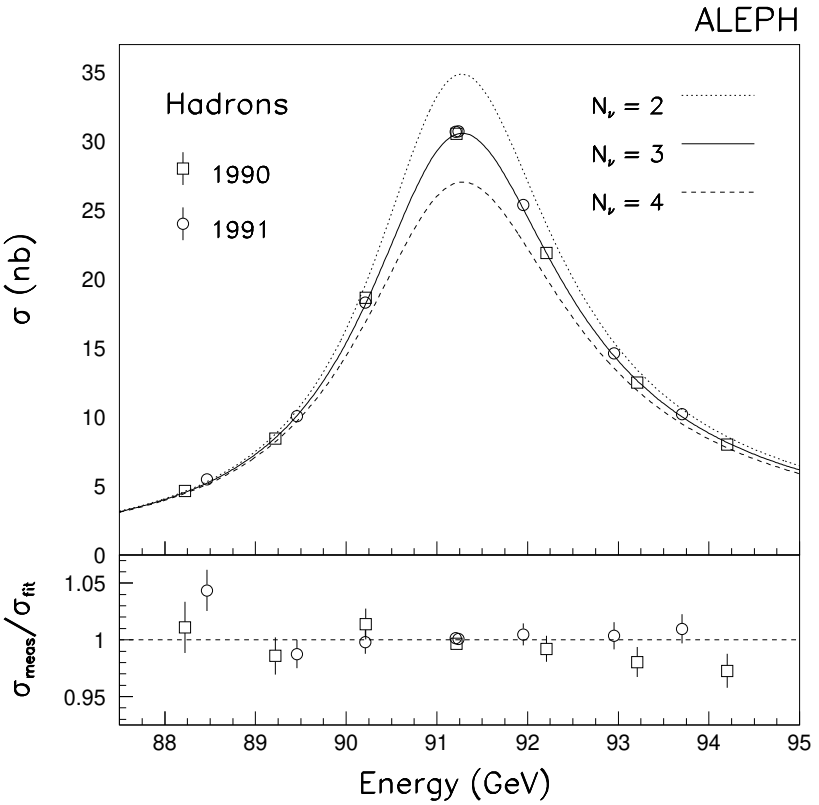

Figure 2.1: *The hadronic cross-section as a function of the centre-of-mass energy. The theoretical predictions are shown for the cases of two, three, and four generations of light neutrinos. The data are consistent only with the hypothesis of three generations.*

2.2 Quantum Chromodynamics

QCD was formulated in analogy to QED as a gauge theory which describes strong interactions between quarks via exchange of massless gauge bosons, the 'gluons'. The six quark flavours (u, d, s, c, b and t) carry a quantum number called colour (red, green or blue). This is analogous to the electric charge in QED. Eight gauge bosons (the gluons) are introduced to mediate the strong interaction. An important difference between QED and QCD is that the gluons also carry the colour charge and can therefore couple directly to other gluons unlike the photons in QED which do not carry electric charge. A consequence is that strong coupling, α_s, is energy dependent. To first order, α_s is given by the equation:

$$\alpha_s(Q^2) = \frac{12\pi}{(33 - 2n_f)\ln(Q^2/\Lambda^2)} \tag{2.1}$$

where Q^2 is the momentum transfer (on the Z peak $Q^2 = (91.2\,\mathrm{GeV})^2$), n_f is the available number of quark flavours ($n_f = 5$ at LEP), and Λ is a parameter determined by experiment. The strength of α_s therefore decreases for higher values of Q^2 (or alternatively very short interaction distances) leading to the property known as asymptotic freedom where the quarks and gluons behave like free particles. Conversely, for small values of Q^2 (large interaction distances) α_s diverges. This explains why quarks are not observed as free particles.

2.3 Hadron Production in Z Decays

Electron-positron annihilation at LEP energies results in the production of the Z boson which subsequently decays to a fermion-antifermion pair. The dominant decay mode is $\mathrm{Z} \rightarrow q\bar{q}$ (branching ratio = $69.91 \pm 0.06\%$ [9]), an illustration of the theoretical description of this reaction is shown in Figure 2.2. The development can be separated into four phases:

(1) Electroweak.

(2) Perturbative QCD.

(3) Hadronisation.

(4) Hadron decays.

The first phase describes the production of the initial hadronic partons, the remaining phases describe the fragmentation of these partons into the final state hadrons. These four phases are discussed below.

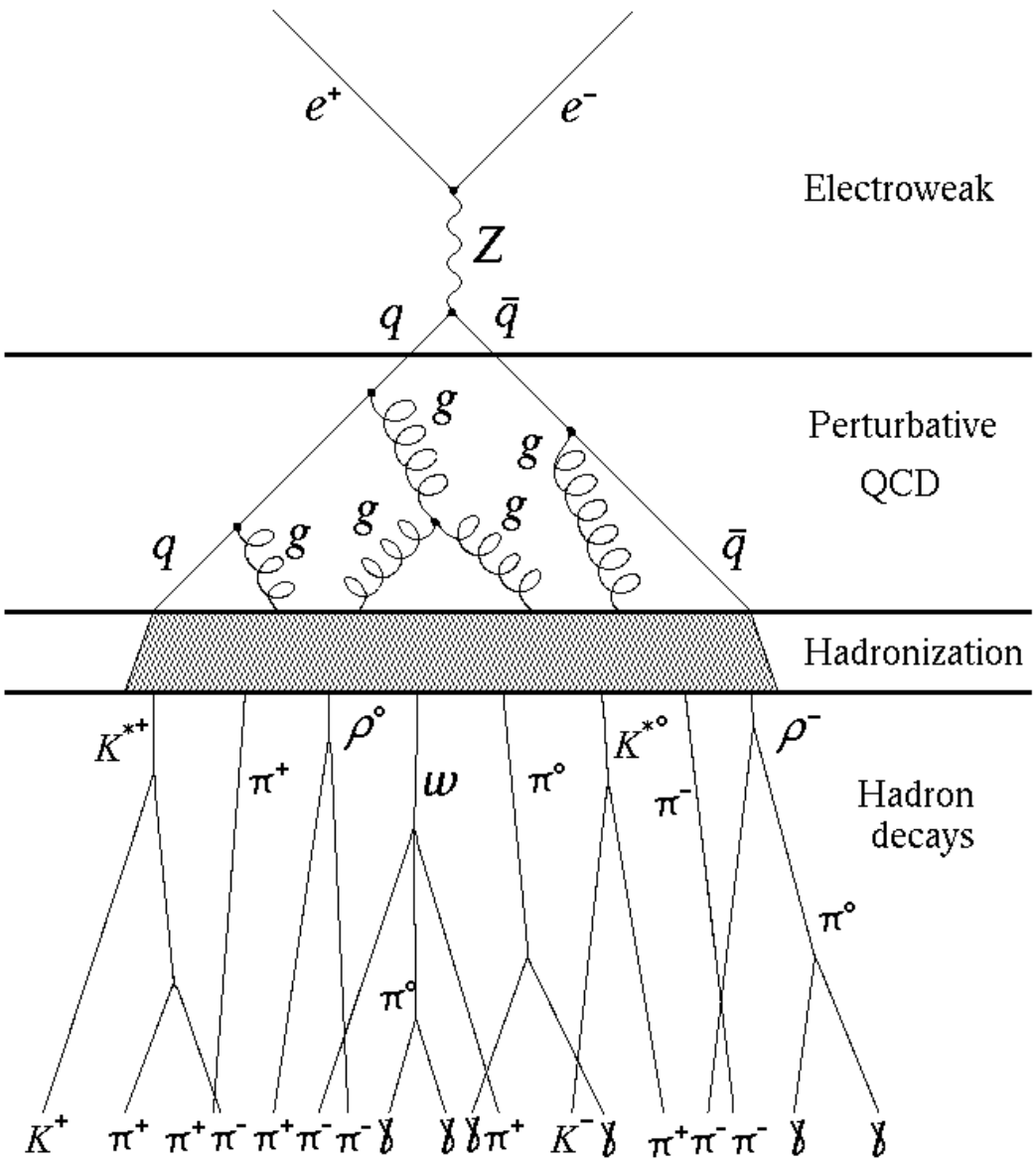

Figure 2.2: *Schematic diagram of the reaction* $e^+e^- \to \mathrm{Z} \to q\bar{q}$. *The development can be separated into four phases: electroweak, perturbative QCD, Hadronisation, and hadron decays.*

2.3.1 The Electroweak Phase

The first phase involves the annihilation of an e^+e^- pair (with the possibility of an initial bremsstrahlung radiation) and the creation of a Z boson and its subsequent decay to a $q\bar{q}$ pair. This phase is described by the electroweak theory.

2.3.2 Perturbative QCD

The initial quark-antiquark pair move apart with a relative speed close to the speed of light, each parton having the beam energy of $\approx 45\,\mathrm{GeV}$. These initial quarks start radiating gluons, which in turn can radiate further gluons or split into secondary quark-antiquark pairs. The early evolution of this process can be described by perturbative QCD. In this phase, momentum transfers involved in the interactions are sufficiently large, giving rise to a small value for the strong coupling constant, for perturbation theory to be applicable. There are two approaches which can be used to model perturbative QCD: the 'matrix element' method, and the 'parton shower' method.

In the matrix element method, available for example in the JETSET ME option of the Lund Monte Carlo [10], a fixed order QCD calculation is used to describe the perturbative phase by generating partonic final states according to the exact QCD matrix elements. The advantage of models based on this method is that interference effects are taken into account properly, and that α_s is well defined. However, as the models only use calculations of the matrix elements to $\mathrm{O}(\alpha_s^2)$, only 2, 3 and 4 parton final states can be generated. At PEP/PETRA energies the matrix element models work reasonably well; however, at LEP energies these do not generate final states with high enough parton multiplicity, resulting in an inability to simultaneously reproduce correctly both 3 and 4-jet rates.

In the parton shower approach the leading terms of the perturbation expansion are summed to all orders. These leading (logarithmic) terms are enhanced and correspond to infra-red or collinear parton emission. Parton shower algorithms are based upon an iterative use of the basic branchings $q \to qg$, $g \to gg$ and $g \to q\bar{q}$. Generally a primary 2, 3 or 4-parton final state is generated using the second order matrix element approach. The configuration is then allowed to shower in a tree-like fashion according to the various probabilities of the branchings given above. The process continues until the evolution variable reaches a predefined cut-off.

It is a general property of the popular shower algorithms that they produce 'coherent' showers. This is achieved, for example, by angular ordering the radi-

ated partons such that the production angle of each parton is never more than the production angle of the radiated parton which preceded it. This angular ordering has an important phenomenological implication as it predicts that the energy flow in the shower remains collimated around the direction of the initial partons. This explains why most hadronic Z decays exhibit a pronounced 2-jet structure. Furthermore, if in the initial stage of the parton shower a hard gluon is emitted at a large angle, it gives rise to a well separated jet.

The weakness of the parton shower approach, however, is that because it sums only the leading-log terms in the expansion it is limited in its predictions for wide-angle parton emission. In this case, the matrix element method is more suitable.

2.3.3 Hadronisation

Towards the end of the parton shower, the momentum transfer Q^2 becomes small and therefore the strong coupling constant becomes large rendering the predictions of perturbative QCD invalid. To model the final phase of fragmentation, i.e. the transformation of the partons into colourless hadrons (hadronisation), phenomenological models implemented as Monte Carlo programs are used. Three main models exist: independent hadronisation, string hadronisation, and cluster hadronisation. The latter two models are implemented in the JETSET and HERWIG programs respectively, and are used in the analysis presented in this thesis. The three models are described below.

Independent Hadronisation

One of the first models of the hadronisation process was the independent fragmentation model introduced in 1977 by R.D.Field and R.P.Feynman [11]. In this model, each original quark and antiquark independently transform into a jet of hadrons in the following way:

$$\begin{aligned} q_0 &\rightarrow h(q_0, \bar{q}_1) + q_1 \\ q_1 &\rightarrow h(q_1, \bar{q}_2) + q_2 \\ q_2 &\rightarrow etc., \end{aligned} \tag{2.2}$$

where q_0 is the quark from the original quark-antiquark pair. This process is illustrated in Figure 2.3. A new quark-antiquark pair $(q_1, \bar{q}_1)$ is created in the colour field of q_0 (from the vacuum) which results in q_0 and $\bar{q}_1$ combining to form a hadron $h(q_0, \bar{q}_1)$. The remaining quark q_1, which has less energy than q_0, then goes on to initiate another quark-antiquark creation $(q_2, \bar{q}_2)$ from which

another hadron is formed. This process of $q \rightarrow q + hadron$ is repeated until the remaining quark has insufficient energy to form a hadron.

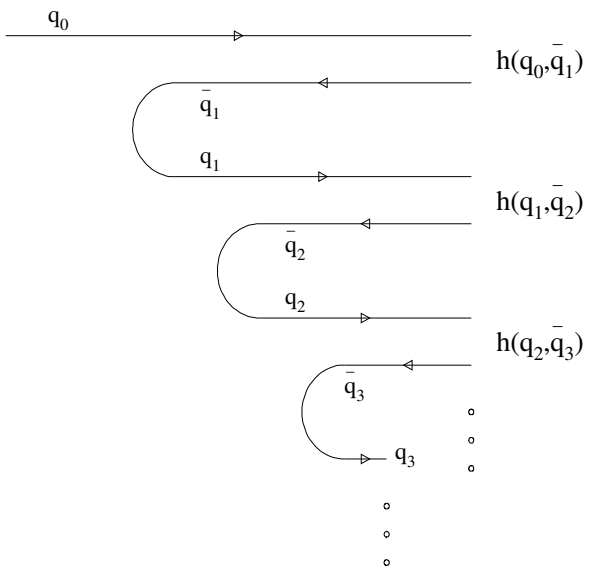

Figure 2.3: *Hadron production in the Field-Feynman model.*

The model involves one arbitrary function $f(\eta)$ which gives the probability that the hadron containing the original quark leaves the remaining jet a fraction η of its momentum. This ultimately determines the momentum distributions of the hadrons. Field and Feynman chose $f(\eta)$ to be of the form:

$$f(\eta) = 1 - a + 3a\eta^2 \tag{2.3}$$

where the parameter a is determined from experiment. It is assumed that this function applies to all iterations of the cascade.

In addition, three other parameters are required to determine the properties of the quark jets.

(1) The ratio of the production of strange quark to up or down quarks: Field and Feynman assumed the quark flavours u, d and s to be produced in the ratios $2 : 2 : 1$, i.e., strange quark production is suppressed due to the larger mass of the s quark.

(2) The spin of the primary mesons: Qualitatively one expects, from spin counting, the ratio of pseudoscalar to vector meson production to be 1:3 multiplied by some factor which disfavours heavier states. However, due to uncertainties in the knowledge of the quark masses the ratio cannot be calculated. Experimentally the ratio is typically one, and so in the model the two spin states are generated with equal probability.

(3) The mean transverse momentum given to the primary mesons: This is determined by requiring that the final hadrons (after decay) have a mean transverse momentum of about 330 MeV/c, to coincide with experimental observations.

To enable the production of baryons, an extension to the model was proposed by Meyer [12], in which it is assumed that occasionally two quark-antiquark pairs, instead of one, are produced from the vacuum. The quarks and antiquarks then align to form baryon-antibaryon pairs.

Although the Field-Feynman model does a reasonable job of parameterising experimental results, a number of problems prevent it from being regarded as a true theory of hadronisation. For example, the model is based on the cascade of a quark jet and so it is not obvious how one should model the cascade of a gluon jet, this is important at LEP energies where multi-jet events are a common occurrence. Also, at the end of the cascade there is always one quark and one antiquark left over, with no simple way of combining them together to form a hadron. This introduces problems with colour and energy-momentum conservation.

The Field-Feynman model has been surpassed by models with a stronger theoretical basis, two of which are the 'string model' and the 'cluster model'. A schematic illustration of these two models are given in Figure 2.4.

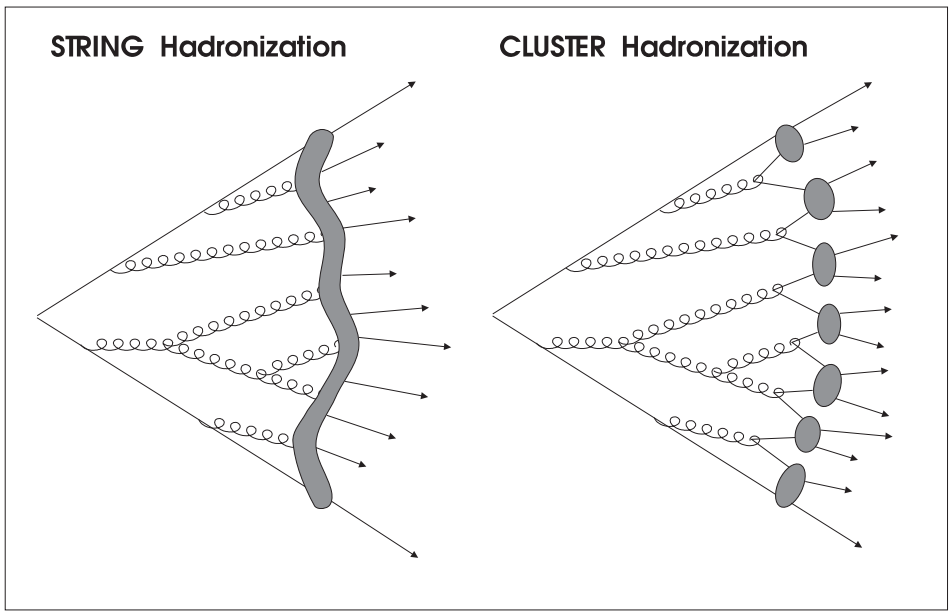

Figure 2.4: *Schematic representation of the string and the cluster hadronisation models.*

String Hadronisation

In the string model, hadron production is described in terms of the break-up of a one-dimensional relativistic string. This picture is motivated by the observation that due to the gluon self-coupling, the field lines of a static colour field attract each other to form a flux tube with a transverse dimension of $\sim 1\,\mathrm{fm}$. This can be compared to the electromagnetic case in which the field lines spread out to infinity; the two cases are illustrated in in Figure 2.5. The flux tube picture is the basis for the Lund model [13].

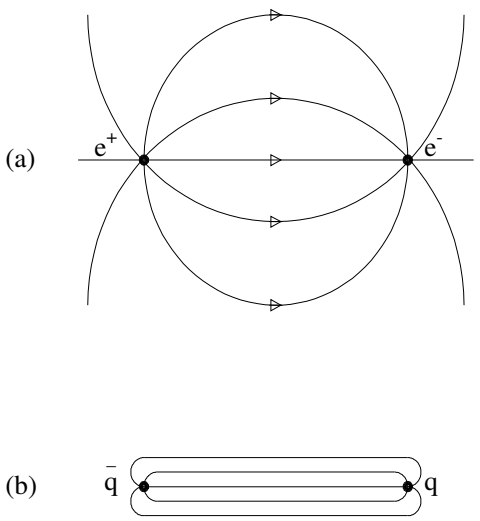

Figure 2.5: *(a) The electric field lines between an electron and positron, spreading out to infinity. (b) The colour field lines between a quark and antiquark, confined in a narrow flux tube with a transverse dimension of* $\sim 1\,\mathrm{fm}$.

If the tube is assumed to be uniform along its length, then this leads to a linearly rising potential and so the QCD potential grows linearly at large distances. Such large distance behaviour is supported by lattice calculations and provides a natural explanation for quark confinement.

In this string model the string is stretched between the original $q\bar{q}$ pair. As the partons move apart, the potential energy in the string increases until it breaks by the production of a new $q'\bar{q}'$ pair splitting the system into two colour-singlet systems $q\bar{q}'$ and $q'\bar{q}$. At large enough energies further breaks of the daughter-strings occur until only on-shell hadrons remain, each hadron corresponding to a small piece of string, with a quark at one end and an antiquark at the other. In this picture, gluons, having the colour structure of a quark-antiquark state, act as kinks in the original string often producing (at LEP energies) independent jets of hadrons clearly separated from the original quark and anti-quark jets.

In the Lund Monte Carlo, the $q'\bar{q}'$ pairs are generated using the idea of quantum mechanical tunnelling. This picture leads to a suppression of heavy-quark production, $u : d : s : c \approx 1 : 1 : 0.3 : 10^{-11}$. Therefore, charm (and heavier quarks) are not expected to be produced in the soft hadronisation, but only in perturbative parton shower branchings ($g \to q\bar{q}$) or in the original Z decay. Due to the uncertainty in the quark masses the suppression of $s\bar{s}$ production is left as a free parameter. As in the Field and Feynman model, vector mesons and pseudoscalar mesons are generated with equal probability, but, the ratio is left as an adjustable parameter for future tuning.

A tunnelling mechanism can also be used to explain the production of baryons. It is assumed that a break in the string can be caused by creation of a diquark-antidiquark pair. A suppression of baryon production comes from the assumption that the diquark mass is larger than the mass of a quark. However, the production of baryons still remains one of the least well understood aspects of particle production.

A spin-off of the Lund scheme has been proposed by the UCLA group [14]. In this model, all suppression of heavy hadron production enters through the hadron mass and so does not require the 'quark parameters' used in the Lund model, such as the s/u ratio. Spin counting is taken care of automatically by Clebsch-Gordan coefficients and no separate parameter for the relative production rates of vectors and pseudoscalars is introduced. The advantage of this model over Lund is therefore a reduction in the number of free parameters.

Cluster Hadronisation

In the cluster hadronisation model, the shower from the perturbative phase is stopped when the parton virtuality falls below some cut-off, $t_0 \approx 0.7\,\mathrm{GeV}$. Gluons are then split into quark-antiquark pairs. Colour-neutral pairs of quarks that are close in phase space then recombine into massive clusters which decay isotropically into observable hadrons. The fundamental parameters in this model are the virtuality cut-off, t_0, and the QCD scale parameter, Λ, which determines the scale of α_s (Equation 2.1).

In the framework of HERWIG, the hadronisation process is as follows. A cluster C with flavour composition $(q_a, \bar{q}_b)$ and mass M_C is decayed into two hadrons h_1 and h_2 with flavours $(q_a, \bar{q}_r)$ and $(q_r, \bar{q}_b)$:

$$C(q_a, \bar{q}_b) \to h_1(q_a, \bar{q}_r) + h_2(q_r, \bar{q}_b) \tag{2.4}$$

The quark (or diquark) flavour 'q_r' is selected randomly, and with equal probability, from the possibilities d, u, s, c, b with the condition that

$$M_C > [m(q_a, \bar{q}_r)]_{lightest} + [m(q_r, \bar{q}_b)]_{lightest} \tag{2.5}$$

where $[m(q_i, \bar{q}_j)]_{lightest}$ is the mass of the lightest hadron in the model that has flavour composition $(q_i, \bar{q}_j)$.

The decay daughters, h_1 and h_2, are selected randomly from a list of hadrons which have the correct quark content, with a probability proportional to their spin degeneracy. For example, an a_2^+ (spin 2) is five times more likely to be selected than a π^+ (spin 0), should the flavour composition be $(u, \bar{d})$. If the sum of the masses h_1 and h_2 is greater than the mass of the decaying cluster then the combination is rejected and another selection made with the above criteria. If accepted, the common 3-momentum p_{cm} of the two daughters in the rest frame of the cluster parent is evaluated. The final probability to select a given pair of hadrons is then proportional to the phase space weight W_{decay} given by

$$W_{decay} = p_{cm} \times (2S_1 + 1) \times (2S_2 + 1) \tag{2.6}$$

where S_1 and S_2 are the spin values of the two daughters h_1 and h_2. W_{decay} then determines whether the cluster decay $C \rightarrow h_1 + h_2$ is accepted or not. In the case of rejection, the process is started again with the selection of a new quark or diquark flavour. If the decay channel is accepted, the daughters are decayed isotropically in the rest frame of the parent cluster.

The model assumes that the process of hadronisation is dominated by the clusters decaying into hadrons according to the available phase-space and the hadrons permitted. This means that phase space alone has to account for the relative production rates of mesons and their corresponding momentum distributions. For example, vector meson production is suppressed due the larger phase space available for the lower mass pseudoscalar mesons, similarly strange meson production is suppressed due to the larger mass of s quarks.

In addition to the fundamental parameters t_0 and Λ, two additional parameters are introduced for the treatment of very low and very high mass clusters: clusters with a mass above a cut-off value (default value = 3.65 GeV/c^2) are split into two clusters which are then allowed to decay isotropically into hadrons. Clusters with a very small mass are allowed to decay into a single hadron. Baryon production is achieved by introducing a probability that a gluon may branch into a diquark-antidiquark pair.

The LPHD Model

An alternative approach to the hadronisation process is taken in the Local Parton-Hadron Duality model (LPHD), where it is assumed that the properties on the parton level are closely related to the corresponding hadronic properties. This implies that certain quantities, such as inclusive distributions, may be studied without making reference to a hadronisation process.

This idea of a local parton-hadron duality has been developed in particular by the St. Petersburg group [15]. In an extreme interpretation, a one to one correspondence is assumed between partons and hadrons, event by event, with a suitable choice of partonic cut-off parameter, Q_0. A 'softer' interpretation, however, is usually favoured in which there is no absolute correspondence event by event, but only in the average behaviour and in the fluctuations around that average. A prediction of this model is that the average momentum of a particle species is dependent on the hadron mass. This is related to the fact that the cut-off, Q_0, in a parton shower is not expected to be constant but correlated to the final state hadronic mass. If the Q_0 is increased then the probability of further parton branching is reduced implying that a final state parton, in addition to having a larger effective mass, will have a greater momentum.

2.3.4 Hadron Decays

In the final phase, the primary hadrons are decayed according to measured branching ratios and lifetimes. In the versions of JETSET used in this analysis, the generators include improved bottom and charm decay tables. The particles visible at the detector level are mainly pions, most of which are the results of decays, the fraction of pions directly from hadronisation being relatively small. Conversely, the fraction of resonances originating directly from hadronisation is high, and therefore inclusive resonance studies (for example, the $\rho^{\pm}$ vector meson study presented in this analysis) provide information which is more closely related to the dynamics of the fragmenting partons. However, inclusive resonance distributions are sensitive to heavy flavour decay tables. The vector resonances are, in addition, sensitive to tensor production; tensors occupy phase-space which would otherwise be occupied by vectors.

In this thesis, the rate of production and the momentum distribution of the $\rho^{\pm}$ vector meson is studied, providing a test of the fragmentation process implemented in the JETSET, PYTHIA and HERWIG Monte Carlos.

2.4 Bose-Einstein Correlations

The Bose-Einstein Correlation (BEC) leads to an enhancement of the two particle differential cross-section for bosons which are close in phase-space. Since most of the particles generated in hadronic events are pion triplets obeying Bose statistics, BECs have been studied in pairs of charged pions in hadronic Z decays [16], [17], and in the determination of $W^{\pm}$ mass as well [18]. The BEC is a quantum mechanical phenomenon that must appear during the fragmentation

state. Hence, the measurement of BECs can help the understanding of QCD studies.

The data are usually analysed interms of the correlation coefficient C_2. $\pi\pi$ correlation is generally parametrised in the phenomenological form:

$$C_2(Q) = 1 + \lambda \exp(-Q^2 R^2) \tag{2.7}$$

where Q^2 is the Lorentz invariant square of the 4-momentum difference of the form

$$\begin{aligned} Q^2 &= -(p_1 - p_2)^2 \\ &= (\vec{p_1} - \vec{p_2})^2 - (E_1 - E2)^2 \\ &= m^2 - 4m_\pi^2 \end{aligned} \tag{2.8}$$

here m is the $\pi\pi$ invariant mass. λ is called the chaoticity parameter, typically $\lambda \sim 1$, and R can be identified with a source radius.

There are some local and global approaches to model BECs in Monte Carlo simulations, [18]. The BEC algorithms is applied to the final state pions, for which the 4-momenta difference is calculated for each pair of identical pions. A shifted smaller Q' is then found such that C_2 of shifted to the original Q distribution. Under the assumption of a spherical phase-space ($d^3p/E \propto Q^2 dQ/\sqrt{Q^2 + 4m_\pi^2}$), Q' is the solution of the equation:

$$\int_0^Q \frac{Q^2 dQ}{\sqrt{Q^2 + 4m_\pi^2}} = \int_0^{Q'} C_2(Q) \frac{Q^2 dQ}{\sqrt{Q^2 + 4m_\pi^2}} \tag{2.9}$$

After applying the corresponding 4-momemtum shift to each pion pairs, the invariant mass of the the pairs are changed. So, it is not possible to conserve both energy and momentum simultaneosly, and so comprimises are necessary. The detailed study and results can be found in [18] and [19].

The experimental studies reveal that BECs affect the distribution of effective masses of $\pi^\pm\pi^\pm$ pairs. It is shown that residual BECs affect significantly the kinematics of very short lived resonances with decay lengths of $\approx 1\,\text{fm}$. This is the case for the ρ^0 meson [7], where BECs exits between the $\pi^+\pi^-$ of the ρ^0, and pions emitted directly from the string. Such BECs distort both the ρ^0 signal and the background shapes.

Residual BECs also appear to affect the $\rho^\pm$ line shape [8]. It has been shown in [16] that the background interference mechanisms (discussed in Section 9.4.4) can have similar phenomenological effects as the residual BEC. Since the interference term describes the distortion in real data very well, residual BECs are indirectly included in our study by the inclusion of a interference term to the fits.

CHAPTER 3

APPARATUS

3.1 Introduction

ALEPH (Apparatus for LEP pHysics) was one of the four detectors positioned around the LEP collider at CERN laboratory in Geneva/Switzerland [20]. LEP produced its first collisions in July 1989 and since then, millions of events have been recorded by the ALEPH particle detector. Its purpose was to explore the Standard Model of particle physics and search for manifestations of new physics. The ALEPH experiment was a large collaboration of several hundred physicists and engineers from 32 universities and national laboratories from around the world. The collaboration closed in 2004.

3.2 Large Electron-Positron Collider (LEP)

The experimental discovery of the neutral weak current in the early seventies verified the theoretical postulate of electroweak unification. In order to study the physics contained in this theoretical framework more precisely, the LEP collider was proposed, with its design parameters being more clearly defined after the discovery of the W and Z bosons by UA2 in 1983 [21, 22].

With a circumference of 27 km, the LEP collider at CERN is the largest e^+e^- collider ever built. LEP operated at the Z peak between 1989 and 1995 with e^+e^- collisions around the Z resonance (91.2 GeV center of mass) for the four LEP experiments ALEPH, DELPHI, L3 and OPAL, Figure 3.1. The collider was upgraded in 1995 and ran until 2000 in its second phase where the collision energy was doubled in order to produce pairs of on-shell $W^{\pm}$ bosons.

The machine enclosed in a tunnel situated between 50 to 170 meters below ground. It consists of eight straight sections joined by eight arcs forming an octagon with rounded corners. Electrons and positrons orbited in bunches (each bunch containing $\sim 10^{12}$ particles) inside an evacuated beam pipe, the positrons

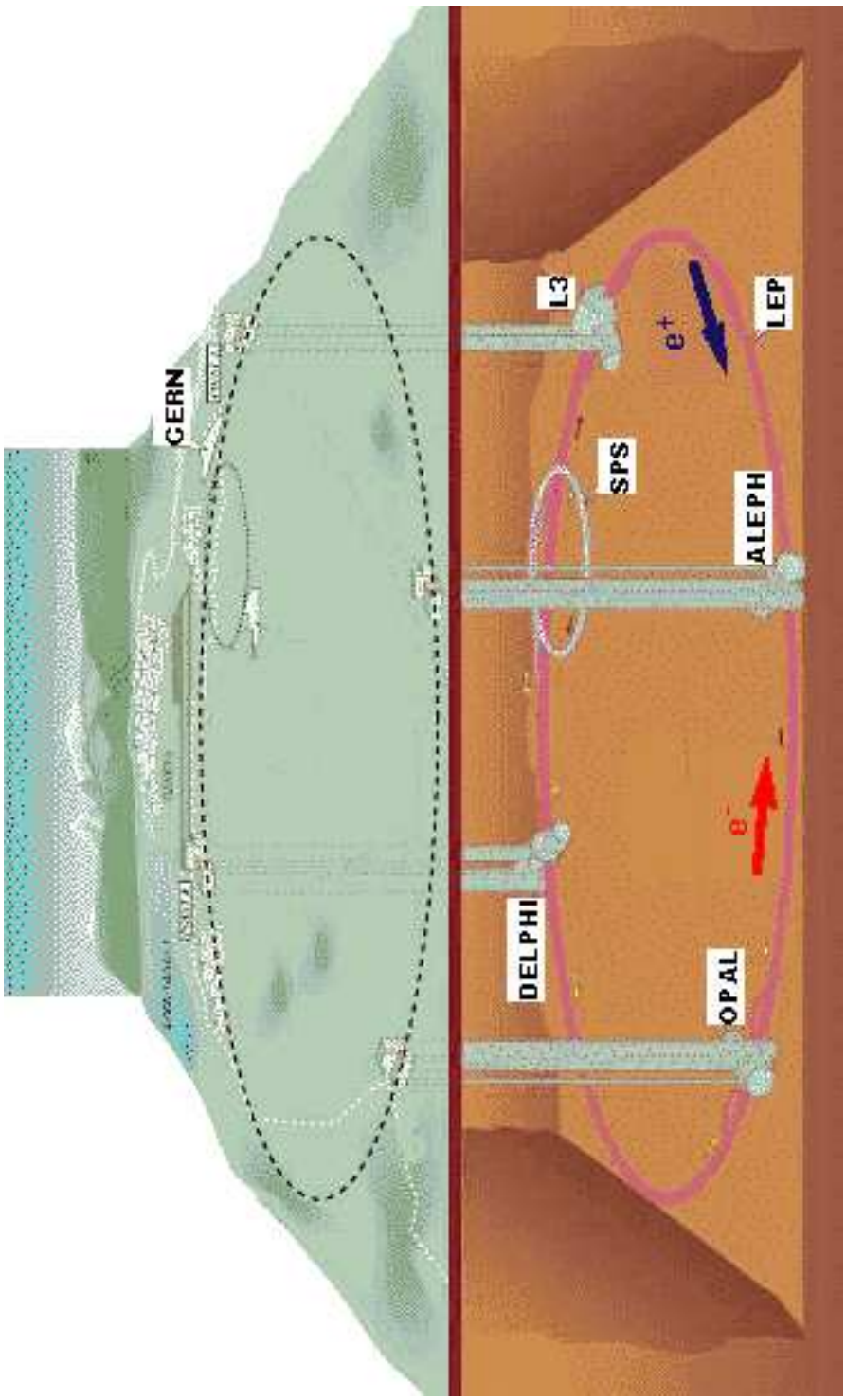

Figure 3.1: *Schematic view of LEP and the four detectors described in the text. It has a circumference of 27 km and is located in an underground 3.8 m diameter tunnel at a depth varying between 50 m and 170 m.*

orbiting clockwise (as viewed from above) and the electrons anticlockwise. The orbits are controlled by electromagnets; 1320 quadrupole and sextupole magnets focus the particles in all the sections, whilst 3392 dipoles bend the beams around the curved sections. The resultant energy loss due to synchrotron radiation is replaced by 128 copper radio frequency (RF) cavities positioned in the straight sections of LEP.

The large circumference of LEP was designed to keep the synchrotron radiation to a practical level, the rate of energy loss being inversely proportional to the radius of curvature. Under the circular acceleration, an electron emits synchrotron radiation, the energy radiated (power lost) per particle per turn being

$$P = \frac{4\pi}{3}\frac{e^2\beta^2\gamma^4}{r} \tag{3.1}$$

or expressing γ in terms of energy, E, and mass m, $\gamma = E/mc^2$

$$P = \frac{4\pi}{3}\frac{e^2\beta^2 E^4}{m^4c^8 r} \tag{3.2}$$

where r is the bending radius, β is the particle velocity, and $\gamma = (1-\beta^2)^{-1/2}$. The disadvantage of building large colliders is the very large cost; for this reason, larger circular e^+e^- colliders are not expected to be built in the future.

Originally there were 4 bunches of electrons and 4 bunches of positrons in circulation, this was increased to 8 bunches on 8 bunches in 1992, and finally running with bunch trains in 1995. In 8 bunch mode the two beams collide, at the center of each LEP detector, every 11 μs. The beams are focused by sextupoles, creating a luminous region (the beam spot) of length 18 mm (in the z-direction), and cross-section with $\sigma_x \approx 0.25$ mm, and $\sigma_y \approx 0.015$ mm (see Section 3.4.1 for a definition of the ALEPH coordinate system). The luminosity of LEP is $\sim 10^{32}\,\mathrm{cm}^{-2}\mathrm{s}^{-1}$, producing Z bosons at a rate of ~ 1 Hz (on peak).

3.2.1 Beam Injection and Acceleration

For part of the injection system, LEP exploited existing CERN installations, namely the Proton Synchrotron (PS) and the Super Proton Synchrotron (SPS). Two purpose-built linear accelerators (linacs) were added to these to complete the injection system shown in Figure 3.2. Electrons (from an electron gun) and positrons (from a tungsten converter) are accelerated to 600 MeV by the LEP injection linac (LIL), and stored in the electron-positron accumulator (EPA). Once a sufficient number of particles have been collected they are transferred to the PS and accelerated to 3.5 GeV. The particles are then injected into the SPS where they are accelerated to 20 GeV and finally injected into LEP. This cycle is repeated until enough particles have accumulated, thus completing the

'fill'. The electrons and positrons are then accelerated to collision energy by the RF cavities.

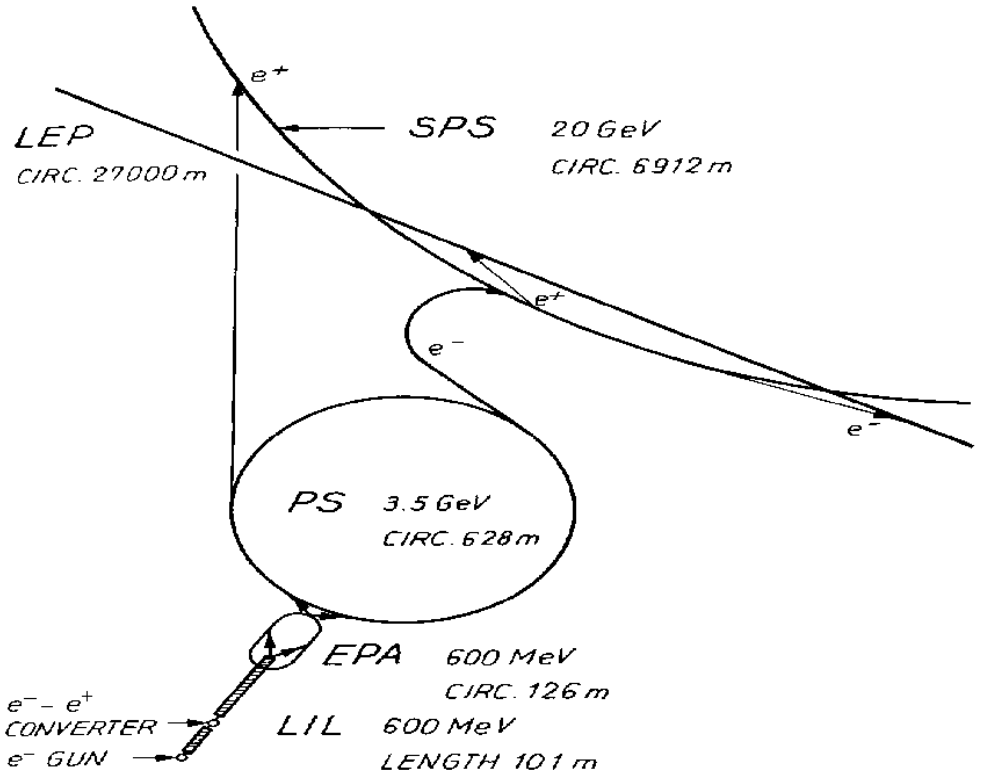

Figure 3.2: *The LEP injection system.*

3.3 Particle Detectors

The detectors employed in experiments in high-energy physics are required to record the position, arrival time, momentum (energy) and identity of charged and neutral particles. If we have an 'ideal' detector, we can reconstruct the interaction, ie. obtain all possible information on it. This is then compared to theoretical predictions and ultimately leads to a better understanding of the interaction/properties of particles. An ideal detector measures all produced particles, their energy, momentum and type (mass, charge, life time, spin, decays). Precise evaluation of position coordinates is required to determine the particle trajectory and, in particular, its momentum (from the deflection in a magnetic field); precise timing is often required in order to associate one particle with another from the same interaction, frequently in situations where the total interaction rate per unit time may be very high.

Neutral particles are detected through their decay (e.g., $K^0 \rightarrow \pi^+\pi^-$) and/or interaction with matter (e.g., $\pi^0 \rightarrow \gamma + \gamma, \gamma \rightarrow e^-e^+$), leading to secondary charged particles. Different particle types interact differently with matter (detector), e.g. photons do not feel a magnetic field. We need different types of detectors to measure different types of particles. Thus, there is no single detector to detect all kind of particles, so a combination of different detectors is employed. An example is the 'ALEPH' detector.

3.4 The ALEPH Detector

3.4.1 Overview

Figure 3.3 shows a schematic view of the ALEPH detector with the main subdetectors labelled.

ALEPH uses a coordinate system usually expressed in terms of Cartesian (x, y, z) or cylindrical (r, ϕ, z) coordinates. In both cases, the z direction is along the beam line with the e^- direction defining the positive axis. The positive x direction points to the center of LEP and the positive y direction is defined such that (x, y, z) forms a right-handed coordinate system.

The detector is designed to measure the momenta of charged particles, to measure the energy deposited in calorimeters by charged and neutral particles, to identify the three lepton flavours, and to measure the distance of travel of short-lived particles such as the tau lepton and the b and c hadrons.

Particular emphasis has been given to momentum resolution up to the highest energies (by means of a large tracking system in a 1.5 T magnetic field), to electron identification (by means of a highly segmented, projective electromagnetic calorimeter, as well as ionisation measurement in the tracking system), and to muon identification (with continuous tracking inside sufficient iron absorber to eliminate the hadrons). Hadron (π, K, p) identification was not emphasized but has turned out to be adequate for some analyses, examples of which can be found in [23].

The tracking system involves three subdetectors: a silicon vertex detector, a drift chamber with 30 cm outer radius, which is also important as part of the trigger system, and a time projection chamber with 180 cm outer radius. Calorimetry proceeds in two stages: electromagnetic and hadronic. A muon detection system of two double-layers of streamer tubes surrounds the whole detector. Finally, important for precise cross-section measurement are the highly segmented luminosity calorimeters.

Presented here is a summary of the main features of the apparatus, more

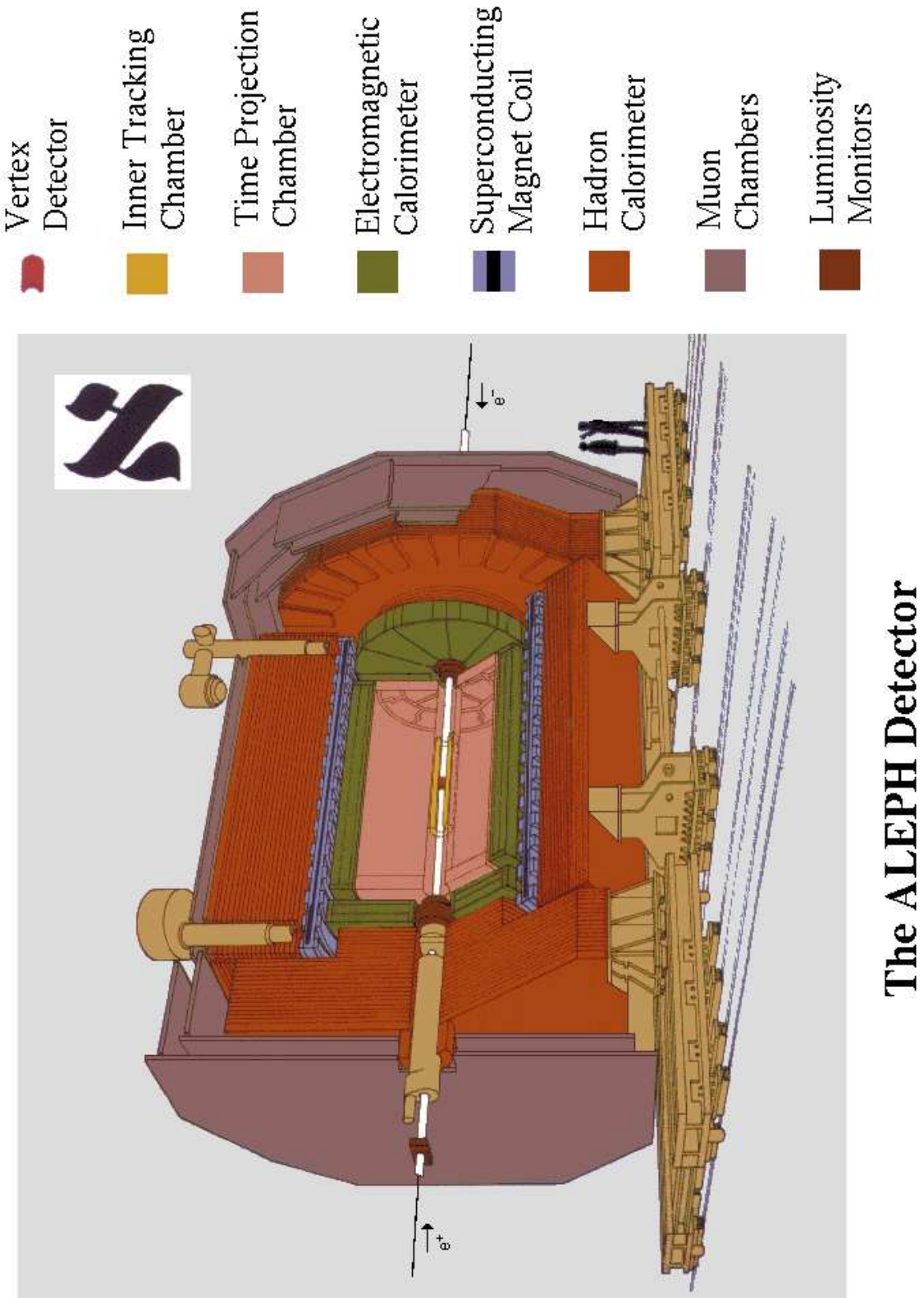

Figure 3.3: *Schematic view of the ALEPH detector. Subdetectors are indicated by different colors.*

detailed accounts can be found elsewhere [24, 25].

3.4.2 The Central Tracking Chambers

The Vertex Detector (VDET)

Close to the interaction point, tracking is performed by a silicon vertex detector. Vertex detector hits are used to provide additional precision for tracks already reconstructed in the outer tracking. From this, it is then possible to reconstruct the decay topologies of short-lived particles with typical decay lengths of as little as a few tenths of a millimetre. The configuration of the VDET is shown in Figure 3.4.

The device is formed from 96 silicon wafers each of dimensions ($5.12 \times 5.12 \times 0.03$) cm, arranged in two coaxial cylinders around the beam pipe. The inner layer has nine wafers in azimuth, with average radius of 6.5 cm, and the outer layer has 15 wafers with average radius 11.3 cm, both layers being four wafers long giving a total length of 20 cm. Each wafer has 100 μm strip readout both parallel ($r\phi$) and perpendicular (rz) to the beam direction. The spatial resolution, for normally incident tracks is: $\sigma_{r\phi} \approx 12\,\mu$m, $\sigma_z \approx 10\,\mu$m.

The Inner Tracking Chamber (ITC)

The vertex detector is surrounded by a conventional cylindrical multiwire drift chamber. It measures the $r\phi$ position of a track on eight concentric layers of hexagonal drift cells at radii between 16 and 26 cm, with adjacent layers staggered by half a cell width. The resolution depends on the drift length in the cell, with an average of 150 μm. The position of tracks along the beam direction (z) is determined by measuring the difference in arrival time of the signals at each end of the wires. This, however, only has a resolution of about 5 cm. The ITC tracking information is used to improve tracking resolution, and to provide information for the first level trigger decision (made within 2-3 μs after a beam crossing).

The Time Projection Chamber (TPC)

The TPC is ALEPH's principal tracking detector providing 21 3D space-point measurements for fully contained tracks at radii between 30 and 180 cm. A view of the TPC is given in Figure 3.5, it consists of a gas volume (at atmospheric pressure) bounded by inner and outer field cages and two end-plates. An electric field is created between a central membrane and the two end-plates (dividing the TPC chamber into two), giving a drift length of 2.2 m on each side. As charged

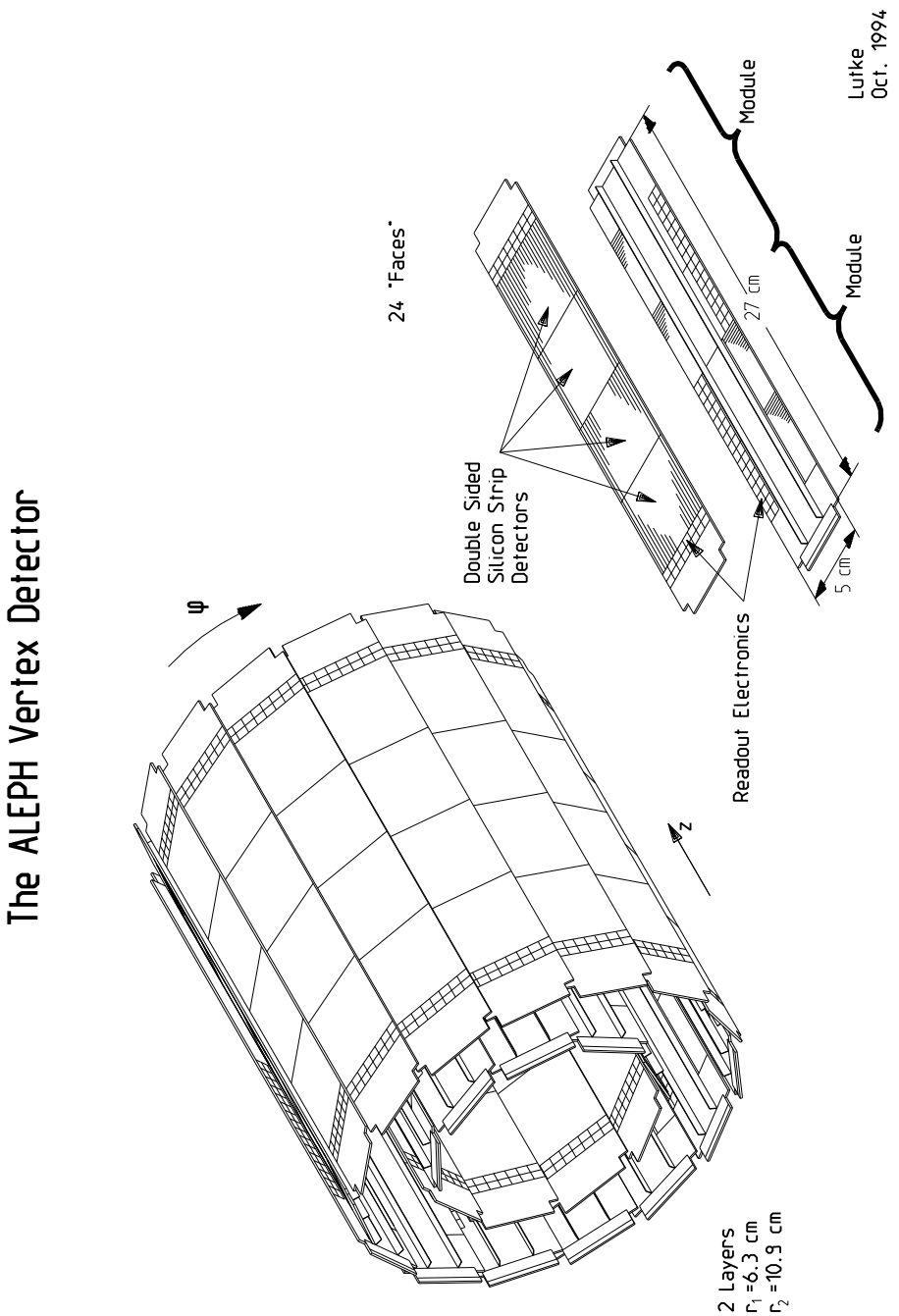

Figure 3.4: *Configuration of the original (1991) vertex detector. The VDET is very close to the beam pipe in order to identify very short-lived particles (such as τ leptons and B mesons) with a high resolution position. This detector consists of two concentric arrays of silicon wafers surrounding the beam pipe.*

particles pass through the chamber they leave a trail of ionised gas. The electrons drift along the electric field lines towards one of the end-plates where they induce ionisation avalanches in proportional wire chambers. These are detected as pulses on cathode pads. The ϕ coordinate is calculated by interpolating the signals induced on cathode pads and the r coordinate is given by the radial position of the pads involved in the measurement. The z coordinate of a point on a track's trajectory is obtained from the electron drift time and the drift velocity.

The pulse height information on the wires provides information about the energy lost by the particle as it traverses the TPC. The rate of energy loss (dE/dx) is dependent on the particle mass and so can be used to identify different particle species. Electron identification is good, with greater than 3σ separation up to $p \approx 8\,\mathrm{GeV/c}$. The π-K separation is roughly constant above $p \approx 2\,\mathrm{GeV/c}$ at about 2σ, while the K-p separation is only about 1σ. Therefore, kaon and proton identification can be accomplished only on a statistical basis; nonetheless, it is an important means of reducing combinatorial background in some analyses.

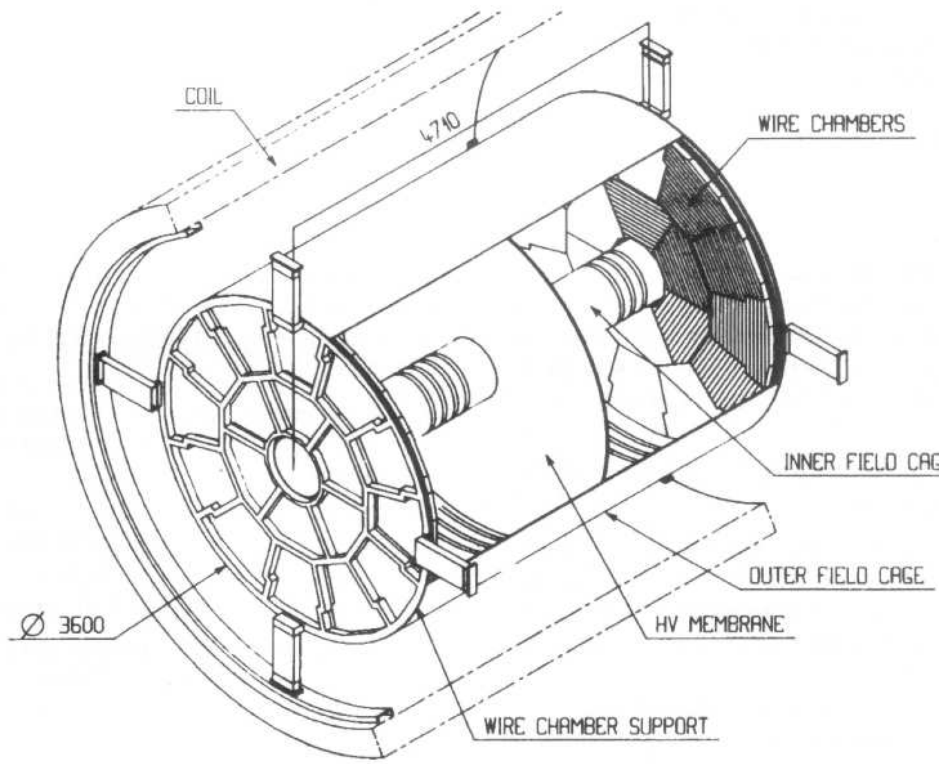

Figure 3.5: *A view of the time-projection chamber.*

Each end-plate of the TPC is subdivided into eighteen individual wire chambers (sectors), the arrangement is shown in Figure 3.6. The pad size is $6.2\,\mathrm{mm} \times 30\,\mathrm{mm}$ ($r\delta\phi \times \delta r$) and the pad pitch in azimuth is 6.72 mm. The geometry of the sectors is designed to minimise losses in track resolution due to

the cracks between the sectors. The resolution is dependent on the angles which a charged track makes with both the sense wires and the cathode pads. The azimuthal coordinated resolution is $\sigma_{r\phi} = 180\,\mu$m at 0° pad crossing angle. The z spatial resolution for wires is $\sigma_z = 1.2\,$mm (with a small z dependence), and 0.8 mm for pads (at $\theta = 90°$).

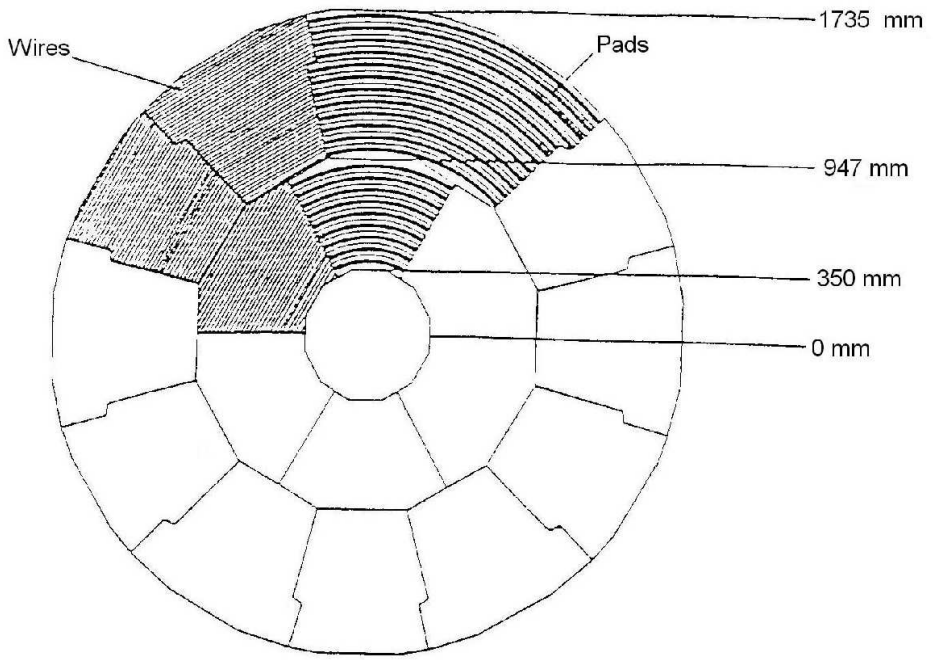

Figure 3.6: *The arrangement of the TPC sectors.*

The transverse momentum resolution and impact parameter resolution are shown in Table 3.1 for the TPC only, for the TPC and drift chamber, and for all three tracking detectors together. At low momentum (less than 0.4 GeV) a constant term of 0.5% should be added to the resolution due to multiple scattering.

Table 3.1: *Momentum and impact parameter resolution for the TPC, the TPC+ITC, and the TPC+ITC+VDET. At low momentum a constant term of 0.5% should be added to the momentum resolution due to multiple scattering.*

	Transverse momentum resolution (p_T in GeV)	Impact parameter resolution	
Detector	$\Delta p_T/p_T$	$\sigma_{r\phi}(\mu m)$	$\sigma_{rz}(\mu m)$
TPC	$1.2 \times 10^{-3}\ p_T$	310	808
+ ITC	$0.8 \times 10^{-3}\ p_T$	107	808
+ VDET	$0.6 \times 10^{-3}\ p_T$	23	28

3.4.3 The Principal Calorimeters

The energy and position coordinates of secondaries from high-energy interactions can also, under suitable conditions, be measured by total absorption methods. In the absorption process, the incident particle interacts in a large detector mass, generating secondary particles which in turn generate tertiary particles, and so on, so that all (or most) of the incident energy appears as ionisation or excitation in the medium−hence the term calorimeter.

For electrons and photons of high energy, a dramatic result of the combined phenomena of bremsstrahlung and pair production is the occurance of cascade showers. A parent will radiate photons, which convert to pair, which radiate and produce fresh pairs in turn, the number of particle increasing exponentially with depth in the medium. A measurement of the position and charge of a shower provides a measure of the position an energy of the electron or photon.

The Electromagnetic Calorimeter (ECAL)

The ECAL is a sampling proportional wire calorimeter consisting of lead sheets and proportional wire chambers covering the angular range $|cos\theta| < 0.98$. The calorimeter stops and measures the energy of electrons and photons. The ECAL is formed from a barrel surrounding the TPC, closed at each end by endcaps. These are divided into 12 modules, each covering an azimuthal angle of 30°, Figure 3.7. The cracks between the modules, where the ECAL is not sensitive to particles, constitute 2% of the barrel surface and 6% of the endcap surface. To ensure that the cracks in the endcaps and the barrel are not coincident the endcap modules are rotated through 15° azimuth.

The modules have 45 lead/wire-chamber layers, Figure 3.8, with a total thickness of 22 radiation lengths. The energy and position of each shower is read out using small cathode pads with dimensions $\approx (30 \times 30)$ mm, arranged to form towers pointing to the interaction point; each tower is read out in three segments in depth, known as storeys, with thicknesses of 4, 9, and 9 radiation lengths respectively. There are 74,000 such towers, corresponding to an average granularity of $0.9° \times 0.9°$. This fine segmentation is important in the identification of photons, electrons and neutral pions. The angular resolution of the ECAL is

$$\sigma_{\theta,\phi} = \left(\frac{2.5}{\sqrt{E}} + 0.25 \right) \text{ mrad}, \tag{3.3}$$

where E is measured in GeV. In addition, signals are also available from the wire planes of each module, providing redundancy in the energy measurement and a low-noise trigger.

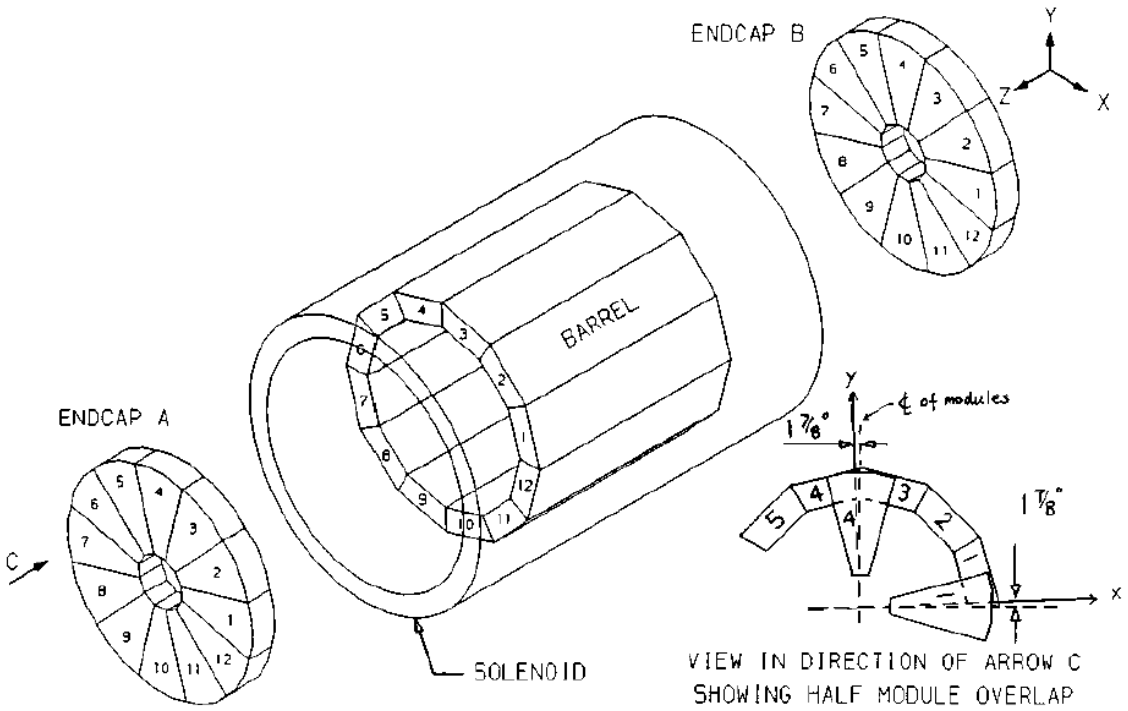

Figure 3.7: *Schematic view of the ECAL modules.*

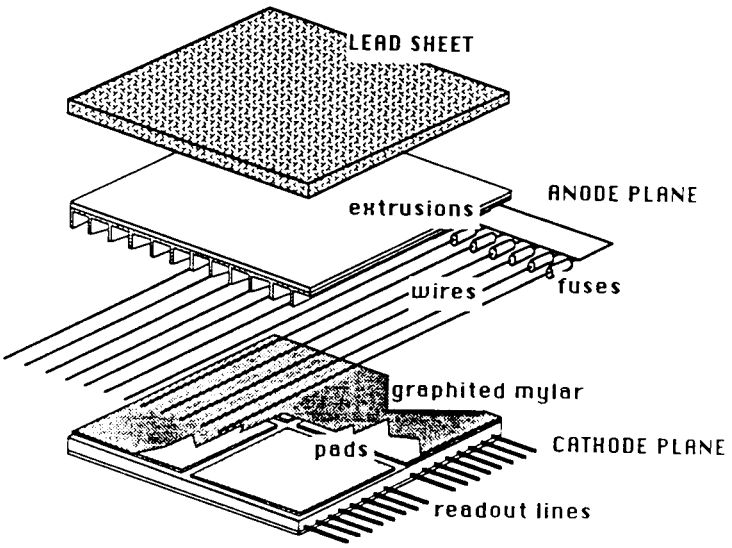

Figure 3.8: *ECAL lead/wire-chamber layers.*

The energy calibration procedure uses electrons from different sources covering the energy range from 1 to 45 GeV. These electrons originate from the reactions $e^+e^- \rightarrow e^+e^-e^+e^-$ for the 1 to 10 GeV energy range, $Z \rightarrow (\tau \rightarrow e\nu\bar{\nu})$ to cover the 10 to 30 GeV energy range, and Bhabha events for 45 GeV.

The energy resolution, determined by comparing the measured energy to the track momentum or beam energy, is shown in Figure 3.9a as a function of the electron energy. The corresponding fitted resolution is:

$$\frac{\sigma_E}{E} = \frac{0.18}{\sqrt{E}} + 0.009 \tag{3.4}$$

where E is measured in GeV. General form of the form of the Equation 3.4 is:

$$\frac{\sigma_E}{E} = \frac{R}{\sqrt{E}} + k \tag{3.5}$$

where R is called stochastic term (slope of Figure 3.9a) and k is the constant term (intercept of Figure 3.9a). This equation can be explained as follows. Energy measured, E, is proportional to number of electrons, n, which are counted in the ECAL shower, because the number of charges is related with energy deposition in any space. Thus:

$$E \propto n$$

But, this counting is a statistical process carrying a statistical uncertainty $\sqrt{n}$ and so the statistical uncertainty on the energy measurement, the statistical component of energy resolution, can be written as:

$$\sigma_E \propto \sqrt{n}$$

One can set up the ratio σ_E/E:

$$\frac{\sigma_E}{E} \propto \frac{1}{\sqrt{n}}$$

and use the relation $E \propto n$:

$$\frac{\sigma_E}{E} \propto \frac{1}{\sqrt{E}}$$

Hence the last relation can be written as an equality by using proportionality constant R,

$$\frac{\sigma_E}{E} = \frac{R}{\sqrt{E}} \tag{3.6}$$

It is clear why R is called the stochastic term. If we compare Equation 3.6 with 3.4, we see $R = 18\%$.

The energy resolution of the ECAL depends not only on stochastic term R but also on the constant term k. This term, however, is significant only at

very high energy (≥ 100 GeV). The value for R and k depend on the particular detector[1] .

The energy resolution as a function of polar angle is plotted in Figure 3.9b for electrons from Bhabha events. In the region around 40° in polar angle the energy resolution is degraded, this corresponds to the overlap region where the electromagnetic shower develops into both barrel and end-cap modules. In that region the total thickness decreases, reaching only 16 radiation lengths, and in addition there is more uninstrumented material due to end-plates of modules and cables.

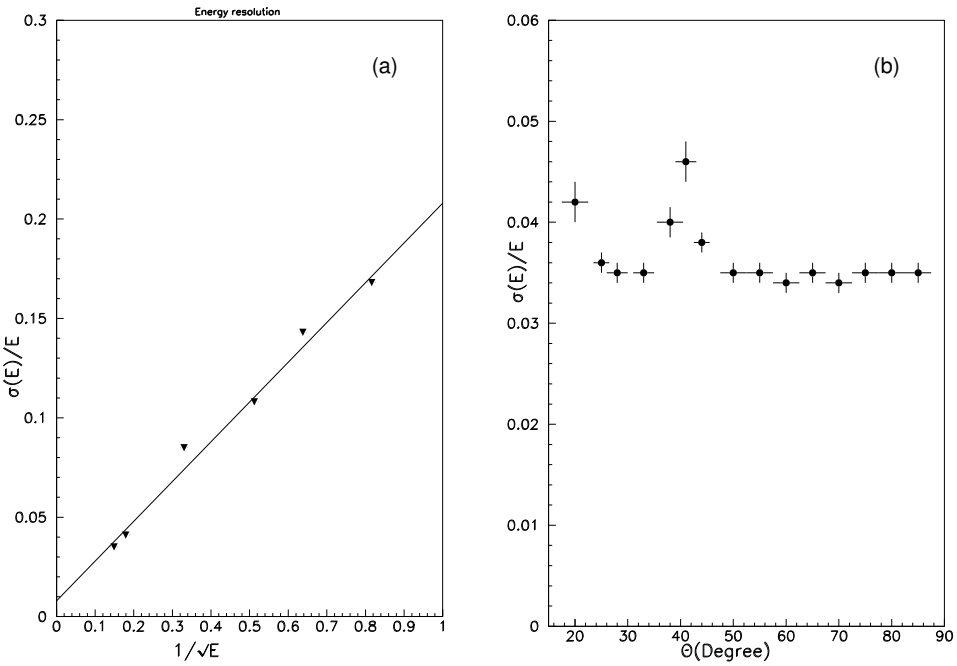

Figure 3.9: *Energy resolution of the electromagnetic calorimeter; (a) dependence on energy, (b) dependence on polar angle for electrons from $Z \rightarrow e^+e^-$ decays.*

The Hadron Calorimeter (HCAL) and Muon Chambers

The hadron calorimeter serves two purposes. It is used, together with the electromagnetic calorimeter, to measure hadronic energy deposits, and it is part of the muon identification system. It consists of 23 layers of plastic streamer tubes separated by 5 cm thick iron slabs, giving a total of 7.2 interaction lengths at 90 degrees. The calorimeter is constructed from 36 modules, 24 in the barrel and 6 in each end-cap, and is read out capacitatively in 4788 projective towers with a

[1] For example, new generation detectors for LHC, $R = 10$ % and $k = 0.7$ % for ATLAS ECAL, and $R = 4$ % and $k = 0.5$ % for CMS ECAL.

typical tower coverage of $3.7° \times 3.7°$, corresponding to 4×4 of the electromagnetic calorimeter towers. The streamer wire signals are summed and used as part of the trigger. The energy resolution of the hadron calorimeter for pions at normal incidence is

$$\frac{\sigma_E}{E} = \frac{0.85}{\sqrt{E}} \tag{3.7}$$

where E is measured in GeV.

Outside the HCAL are another two double layers of streamer tubes which form the muon chambers (acting as simple tracking devices). Two coordinates are obtained from cathode strips both parallel and perpendicular to the wires in each layer. In conjunction with HCAL, the muon chambers are used to identify muons and keep hadron/muon misidentification to a minimum.

3.4.4 The Superconducting Solenoid

The ALEPH magnet is a liquid helium-cooled superconducting solenoid with a magnetic field strength of 1.5 T at a current of 5000 A. The field provides the curvature to charged tracks from which the momentum and sign of charged particles can be determined.

3.4.5 The Luminosity Monitors

The precise measurement of electroweak parameters requires accurate knowledge of the beam luminosity. The reaction rate for a process is given by $\mathrm{R} = \sigma\mathcal{L}$ where σ is the interaction cross-section and $\mathcal{L}$ is the luminosity. Low angle elastic (Bhabha) scattering is used to measure the luminosity as it is almost a pure QED process with very little interference from the weak sector, and has a well known cross-section.

The Silicon Calorimeter

The Silicon Luminosity Calorimeter (SiCAL) is ALEPH's main detector for providing luminosity measurements. It is positioned around the beam pipe at each end of the detector and covers angles between 24 to 58 mrad from the beam axis.

The SiCAL uses 12 silicon/tungsten layers (23.3 radiation lengths) to sample showers produced by Bhabhas. Finely spaced pads determine the angle of an incident particle with a polar resolution of 0.15 mrad. The shower depth gives a measure of the energy deposited with a resolution of 3.4% at 45.5 GeV.

The Luminosity Calorimeter

The Luminosity Calorimeter (LCAL) is a lead/wire calorimeter, similar in design to the ECAL, comprising 38 layers (24.6 radiation lengths). Modules are positioned, on either side of ALEPH, just behind the SiCAL modules. The LCAL monitors polar angles from 45 to 190 mrad with a resolution of 0.5 mrad (at 45.5 GeV), and has an energy resolution of $\sim 0.15/\sqrt{E} + 0.01$, where E is measured in GeV.

BCAL

Online luminosity monitoring is provided by the Bhabha calorimeter (BCAL). This is a sampling calorimeter made of layers of tungsten and plastic scintillator, with a single plane of silicon strips to provide position measurements. The BCAL is positioned next to the beam pipe at 7.7 m from the interaction point, receiving a Bhabha hit rate of ≈ 7 Hz.

3.4.6 ALEPH in Numbers

The ALEPH detector dimensions and resolutions are summarised in Table 3.2. The data is taken from [26].

Table 3.2: *A summary table showing the sizes and resolutions of the some sub-detectors of the ALEPH detector.*

Detector	R_{inner} cm	R_{outer} cm	Length cm	Resolution
VDET	6.5	10.8	20	$\sigma(r,\phi) = 12$ μm $\sigma(z) = 10$ μm
ITC	12.8	28.8	200	$\sigma(r,\phi) = 20$ μm
TPC	31	180	470	$\sigma(r,\phi) = 180$ μm $\sigma(z) = 1$ mm $\sigma(p) = 1.2 \times 10^{-3} p^2$ GeV/c
ECAL	185	225	477	$\sigma(\theta,\phi) = 2.5/\sqrt{E} + 0.25$ mrad $\sigma(E) = 0.18E + 0.01\sqrt{E}$ GeV
HCAL	300	468	700	$\sigma(E) = 0.85E$ GeV
SICAL	6.0	14.6	12	$\sigma(\phi) = 0.3^o$ $\sigma(z) = 7$ cm $\sigma(E) = 0.23\sqrt{E}$ GeV
LCAL	10	52	42	$\sigma(\theta) = 2.5\sqrt{E} + 0.16$ mrad $\sigma(E) = 0.15E + 0.01\sqrt{E}$ GeV

3.5 Trigger and Data Acquisition Systems

3.5.1 The Trigger System

ALEPH employs a three-level triggering system in order to separate genuine e^+e^- interactions from background, to reduce the frequency of accepted events to a rate which can be written to tape, i.e. about 1-2 Hz, and to reduce the dead-time of the detector. The background events are mainly from three sources: beam-gas interactions, off-momentum particles from the beam hitting either collimators or the vacuum pipe, and cosmic rays.

The maximum output acceptable from the level 1 trigger is a few hundred Hertz in order to keep dead-time in the data acquisition to a minimum and to ensure there are no TPC gating problems. To enable the trigger to be sensitive to all areas of physics, it uses information from the HCAL, ECAL, LCAL and the ITC. After a bunch crossing, there is a level 1 *yes* if:

- there are track candidates in the ITC;
- there is energy in a 'trigger region' of the ECAL or HCAL;
- the total energy in the barrel, in either endcap, or entire detector is larger than given thresholds;
- there is a Bhabha event in the SiCAL.

Level 1 uses dedicated hardware to enable a decision to be reached in 5 μs, therefore a level 1 *no* can be reached before the next bunch crossing. The level 1 trigger has a 100% efficiency for hadronic Z decays and $(99.7 \pm 0.2)\%$ efficiency for Bhabha events.

The second level trigger decision is made within 50 μs of the bunch crossing and is used to verify the first level trigger. The trigger only involves the TPC; trigger pads on the TPC end-plates are used to check for the presence of charged particle trajectories in regions predicted by the Level-1 decision. Its aim is to stop and clear data acquisition if it cannot confirm the Level-1 decision. A *yes* decision initiates the readout from the front-end electronics and the data are transferred through the DAQ system. This rate should be kept below 10 Hz in order to keep the dead-time to a minimum; about 75% of the level 1 track-only triggers are removed.

The third level trigger is a 'software trigger' and is only applied after the readout of an event. The aim of this third-level event selection is to identify genuine e^+e^- interactions and separate them from the background triggers, and reduce the output frequency to the desired 1-2 Hz.

3.5.2 The Data Acquisition System (DAQ)

The role of the DAQ is to read the electronic signals of events and format the data so that they may be recorded for event reconstruction. A simplified view of the DAQ system is presented in Figure 3.10, illustrating the flow of data from the front-end electronics to the final stage of event reconstruction. The main steps in the data flow are as follows:

(1) A timing signal, synchronised with the LEP bunch crossings, is sent to the trigger supervisor from the T0 module.

(2) The trigger supervisor transmits the timing signal to the readout controllers (ROCs) which, for most of the subdetectors, initiates the digitisation in the front-end electronics. After compacting the data through 'zero-suppression', calibrations are applied and the reduced data formatted. The results are then stored in the ROCs' output buffers.

(3) The Level 1 and Level 2 trigger decisions are made and transmitted to the ROCs. A rejection halts the digitisation process and causes the ROCs to be reset and prepared for the next event. If a trigger is accepted at Level 2 then the whole event is digitized.

(4) After digitisation, each ROC sends a signal to the corresponding subdetector event builder (EB) for its data to be read out. These data are processed by the EB and stored in its output buffers.

(5) With an event in its output buffer an EB sends a request to the main event builder (MEB) to be read out. The MEB reads all the subdetector EBs and assembles the whole event. After testing for completeness, the event is passed to an event processor (EP) which performs the Level 3 trigger analysis. A Level 3 *yes* decision results in the event being written to a disk and then to tape. The data are now available for event reconstruction, this is the subject of the next chapter.

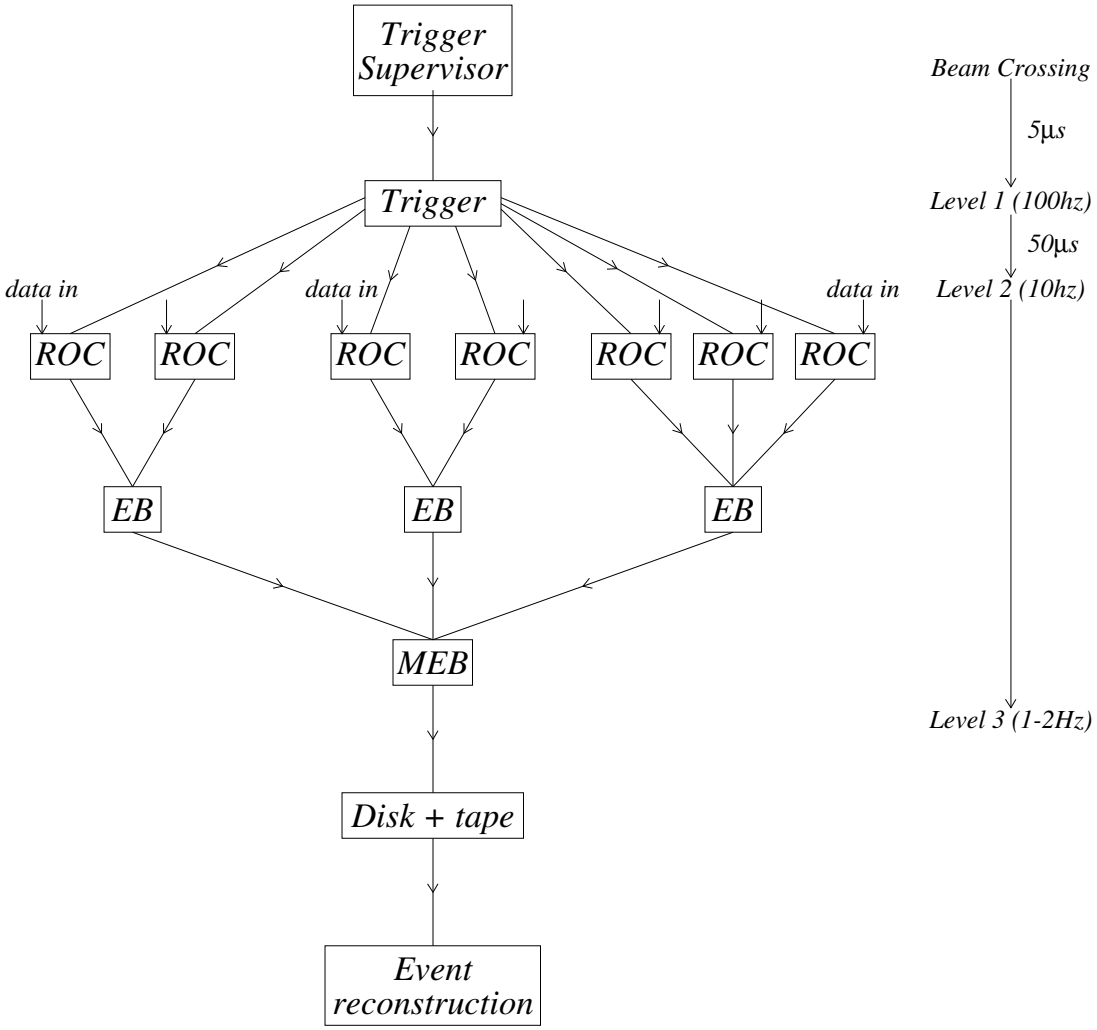

Figure 3.10: *A simplified outline of the data acquisition (DAQ) system, including the trigger sequence.*

CHAPTER 4

EVENT RECONSTRUCTION AND SIMULATION

4.1 Introduction

Recorded data containing the raw event information are reconstructed offline by the JULIA program. Tracking and calorimeter reconstruction is performed on both real and simulated data (simulated data will be discussed in Section 4.6). The results from JULIA are formed into BOS banks and written to Production Output Tapes (POTs) and then to Data Summary Tapes (DSTs) ready for physics analysis; DSTs contain almost all the information from the POTs, but with non-interesting events (i.e. noise and background) removed. Figure 4.1 illustrates the flow of data from event production to the storage of reconstructed events ready for physics analysis.

A more compact form of data storage is the Mini-DST, which is important for analyses which process a large number of events. Mini-DSTs contain less information and the data are integerised, so that these tapes can be staged to disk more quickly, or stored permenantly on disk, and read more quickly by the analysis program. Additionally, results of some time-consuming algorithms are already available on the Mini-DSTs, further reducing processing time. The Mini-DST is used in the analysis presented in this thesis. The total data (6.4 million Monte Carlo and 4.2 real data events) occupies 100 Gbyte of disk space.

The reconstruction of data by JULIA is described here with emphasis on track reconstruction in the TPC and γ/π^0 reconstruction in the ECAL. The final section describes event simulation.

4.2 Track Reconstruction

Figure 4.2 shows examples of the reconstruction of tracks from coordinates in the TPC. Each track is the result of fitting a helix to chains of 3-dimensional space coordinates which are consistent with the trajectory of a charged particle. Note that the tracks are curved in the xy projection, but straight in the z projection. The following sections describe details of TPC coordinate determination and track fitting.

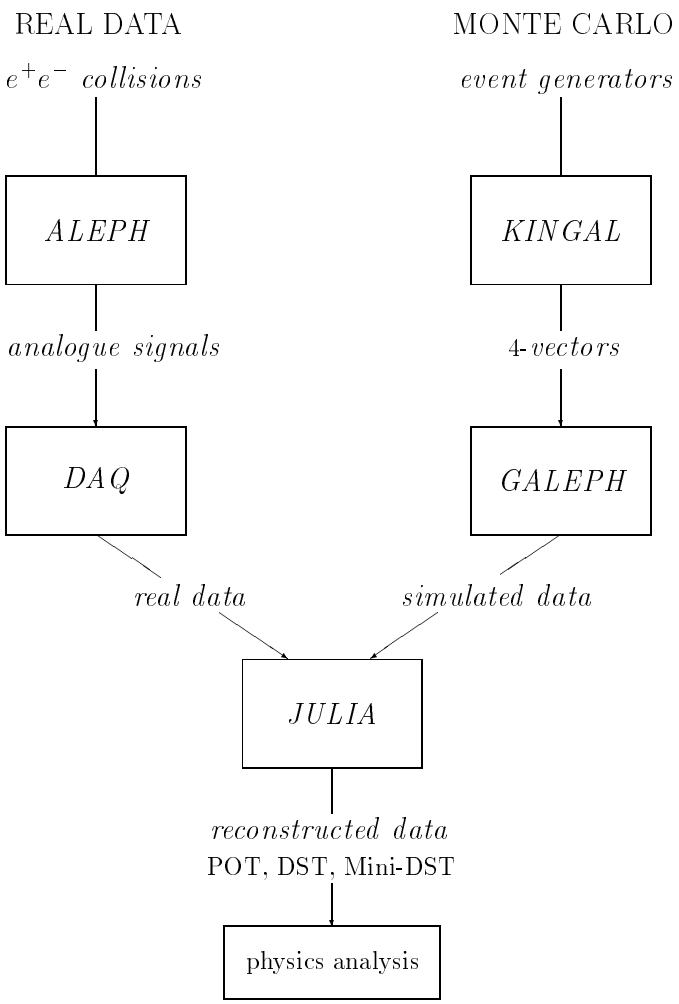

Figure 4.1: *The flow of data in the ALEPH experiment, including the simulated-data chain.*

4.2.1 TPC Coordinate Determination

The raw data collected from the TPC comes in two forms:

- The pad hits, which contain the pad number, arrival time and duration of the pulse.

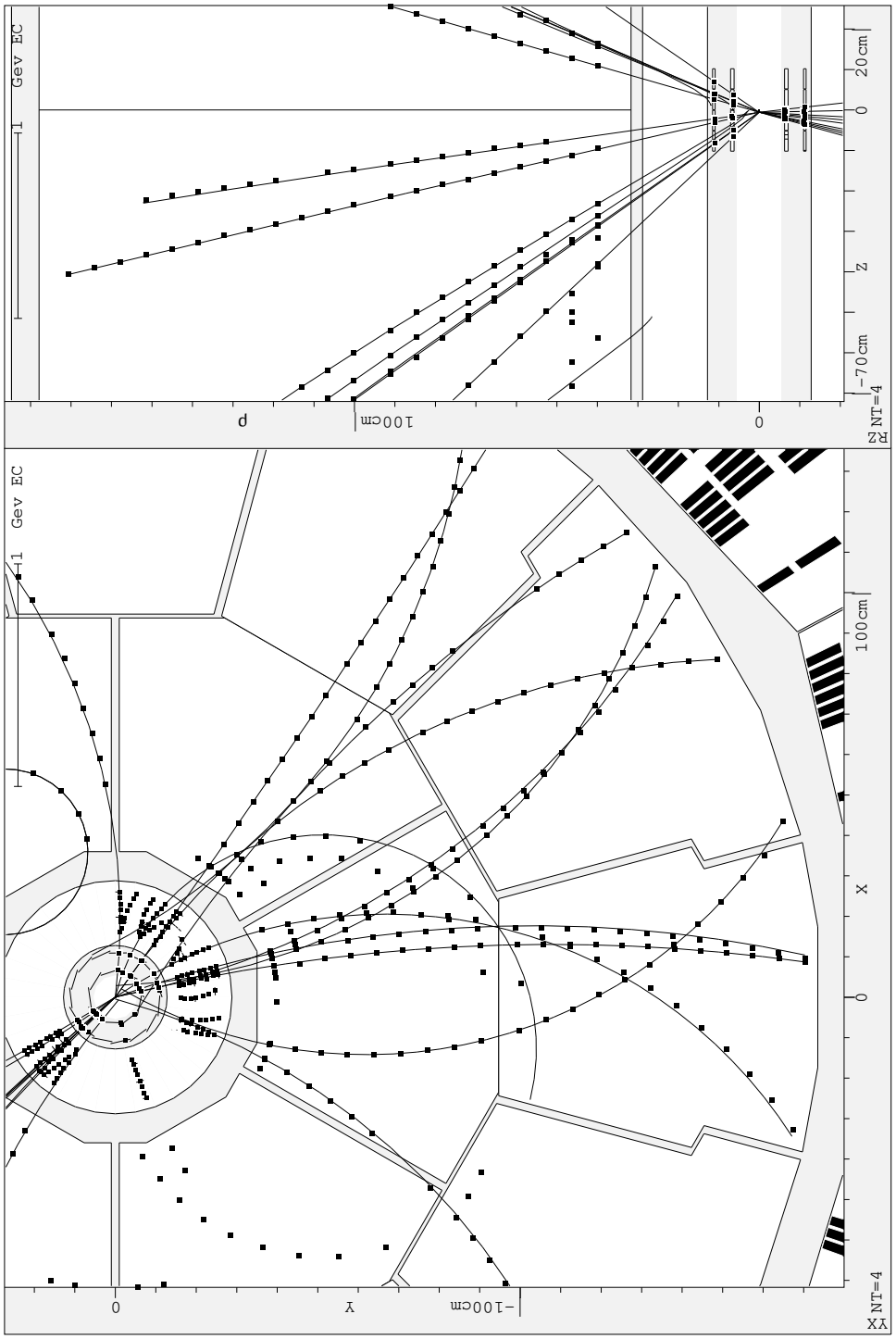

Figure 4.2: *Reconstruction of tracks from coordinates in the TPC. Two projections are shown: the xy projection, and the rz ($r^2 = x^2 + y^2$) projection.*

- Digitised pulse-heights per time-slice, or 'buckets', corresponding to each pad hit.

Clusters and Pulses

Coordinate determination begins with the identification of clusters of pad hits (pulses) on a given pad row in the plane of 'pad number' versus 'drift time'. A cluster is built, ignoring for the moment pulse-height information, by starting with one hit and including hits on adjacent pads if they overlap the first by at least one sample. An example of such a cluster is shown in Figure 4.3, the cluster is formed by two nearby tracks which are not clearly distinguishable at this stage.

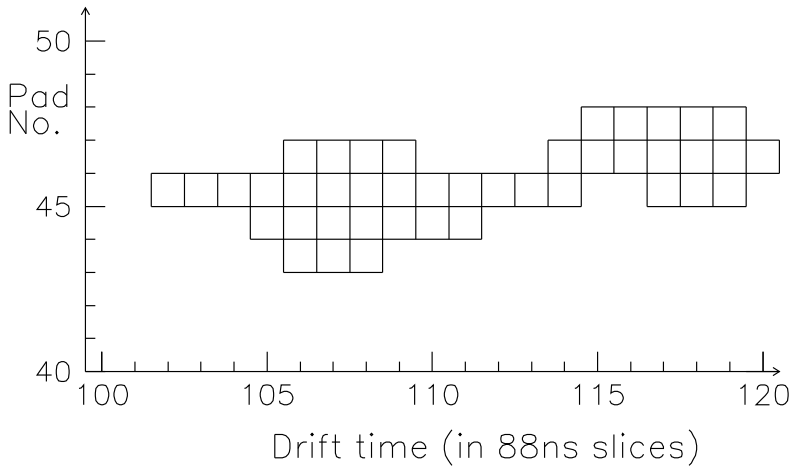

Figure 4.3: *A TPC pad row cluster formed by two nearby tracks.*

A good cluster satisfies the following criteria:

- A minimum of 2, and a maximum of 20 pads in the cluster.
- The minimum cluster length is 5 and the maximum is 35.

A rejected cluster is flagged as a 'bad' coordinate; such clusters are not included in track reconstruction.

Subclusters and Subpulses

Once clusters have been established they are analysed again with the pulse-height information included in order to separate, or at least recognise, within each cluster the contributions coming from different particles. Figure 4.4 illustrates an example of a cluster which is separated, in drift time (or z), into three subclusters by inspecting the pulse-heights. The charge profile of each pulse is analysed for evidence of multiple peaks. Peaks that are sufficiently isolated from others form

subpulses. Groups of subpulses on adjacent pads are aligned with respect to time (or z) and grouped into subclusters. Within a subcluster, each subpulse must be on a separate pad. The charge profiles of the resulting subclusters are also scanned for evidence of multiple peaks; if a valley between peaks is sufficiently low then such a subcluster can be broken in $r\phi$, otherwise it is flagged as being unusable. Examples of such unusable clusters are shown circled in Figure 4.2: the hits from the two tracks originating from a photon conversion in the TPC gas are only resolved when the tracks are separated by a sufficient distance. For each subpulse, both a charge estimate and a time estimate are made from the digitisations. These are used in the reconstruction of coordinates.

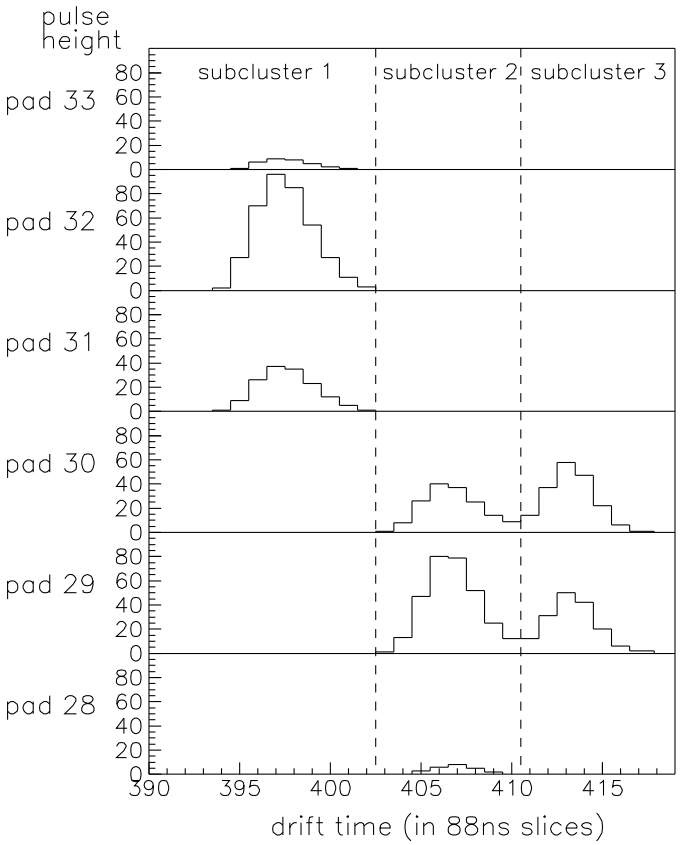

Figure 4.4: *An example of a complex cluster and how the reconstruction program has broken it down into three contributions from which three individual coordinates can be calculated.*

Coordinates

Each 'good' subcluster is used to calculate a z and $r\phi$ coordinate. For the $r\phi$ coordinate the sub-pulse charge estimator is used: a Gaussian fit is made if the subcluster has 3 or less pads, or a charge-weighted average of the pad position

is taken if the subcluster has more than 3 pads. The z coordinate is calculated using both the charge estimator and the time estimator.

4.2.2 TPC Track Finding and Fitting

Track candidates are formed from TPC coordinates as follows. Sets of coordinates which are consistent with an arc of a helix less than π radians are formed into 'chains'. Chains that are determined to belong to the same helix (e.g. multiple arcs of a spiral) are linked together into a single 'track candidate'. To account for multiple scattering, the coordinate error estimates are increased in accordance with the distance from the track origin. If an acceptable fit is not obtained, then up to two points are removed from the fit, corresponding to those that contribute the most to the χ^2 of the overall fit. If this does not result in an acceptable fit then a search is made for a kink in the track candidate, and if one is found the track is split. If no significant kink is found then a search is made for bad points by fitting a track candidate with one point at a time removed. If none of these methods leads to a good fit the track candidate is kept without modification. Details of the algorithms used to find and combine the chains into track candidates can be found in [27].

The track finding efficiency in the TPC has been studied using Monte Carlo simulation. In hadronic Z events, 98.6 % of tracks that cross at least four pad rows in the TPC are reconstructed successfully; the small inefficiency, due to track overlaps and cracks, is reproduced to better than 10^{-3} by the simulation.

The five helix parameters shown in Figure 4.5 are determined by fitting a helix to the pad coordinates within the first half turn of each track candidate. A

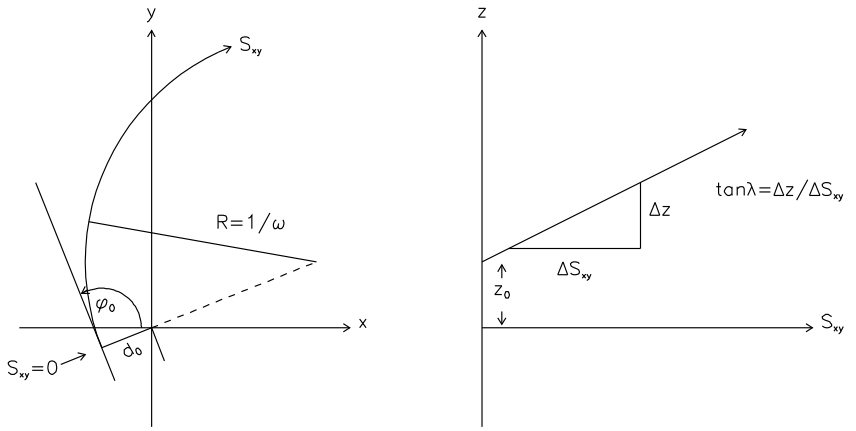

Figure 4.5: *Helix parameters used in the TPC tracking algorithms. For this case all parameters are positive.*

circle fit made in the xy plane yields ω (the inverse radius of curvature), d_0 (the impact parameter in the xy plane), and ϕ_0 (the emission angle in the xy plane).

A straight line fit in the s_{xy}-z plane yields z_0 (the z coordinate at the closest approach to the z axis) and tanλ (the tangent of the dip angle). The circle fit parameters are used to calculate the values of s_{xy}.

4.2.3 TPC-ITC-VDET Track Association

Once TPC tracks have been identified, ITC and VDET coordinates are added to improve the track measurement. The TPC tracks are projected back into the ITC and a search is made for ITC coordinates within a 'window' defined in z and ϕ around the trajectory. If no ITC hits are found in the first two outer layers then the search is abandoned. If more than three hits are found, a fit is performed and the ITC coordinates may be accepted, subject to a cut on the χ^2 of the fit. Finally VDET hits are associated to tracks which extrapolate close to them and the tracks are then refitted.

4.3 Ionisation Energy Loss

The TPC also provides information on a charged particle's rate of loss of energy due to ionisation (dE/dx). This information is obtained from the measured ionisation on the TPC sense wires and is calculated as follows:

(1) The raw digitisations for each wire pulse are reduced to time and charge estimates.

(2) The wire pulses are associated with the reconstructed TPC tracks. Individual wire pulses that match to more than one track are ignored, as are pulses which do not have a shape consistent with single track ionisation.

(3) The truncated mean dE/dx is calculated for each track: the dE/dx samples are distributed according to a Landau distribution and the mean is calculated after discarding the upper 40% and lower 8% of the sample. The upper truncation is to reject samples arising from hard scattering, and the lower one reduces the dependence of the dE/dx estimator on track angle and drift length.

4.4 Calorimeter Reconstruction

Data from the ECAL and HCAL are also processed by JULIA. This section describes briefly the formation of calorimeter objects, the following section describes in more detail the reconstruction and identification of photons in the ECAL.

Calorimeter Clusters and Objects

Clusters of energy deposition in the ECAL are formed by associating a group of spatially connected storeys (i.e. storeys which possess a common corner). All storeys which have an energy exceeding the threshold t_{low} (typically set to 30 MeV to minimise effects of noise) are used as input to the cluster finding algorithms. A topological cluster is only retained if it contains at least one storey above the threshold t_{high} (typically 90 MeV).

ECAL clusters are then associated with nearby charged tracks, clusters which are more than 3 cm (about one pad width) from the entry point of a charged track into the ECAL are considered to be neutral. Clusters associated with minimum ionizing tracks, electrons, and neutral particles are distinguished. Charged clusters with excess energy may have photons associated with them. A similar process is carried out to form HCAL clusters. Calorimeter objects are then formed from the calorimeter clusters with the possibility of more than one particle contributing to each object. ECAL and HCAL objects which overlap are merged into combined calorimeter objects. Further information on calorimeter reconstruction can be found in [27].

4.5 Photon Reconstruction

The clustering algorithm described above builds large clusters, often merging energy from photons and hadronic interactions. For the purpose of improving photon reconstruction, particularly in hadronic events, an extension to the above algorithm is implemented. It uses the facts that electromagnetic showers generally start in the first segment in depth of the electromagnetic calorimeter and that, unlike the cell patterns of hadronic clusters, storeys receiving energy from a photon have a compact arrangement and most of them share a face with another storey associated to the same photon. Figure 4.6 shows the energy deposits of three photons in the ECAL, the showers begin in stack 1 (the first picture), they have a maximum in stack 2, and have almost completely disappeared by stack 3. It is apparent from the figure that the large cluster contains two subclusters due to two photons, the algorithm for photon reconstruction described here attempts to resolve these clusters by forming 'G-clusters' as follows.

4.5.1 G-clusters

G-clusters are formed as follows. The storeys of stack 1 of the ECAL are scanned in the order of decreasing energy. A storey without a more energetic neighbour defines a new G-cluster. Other storeys in the same stack are assigned

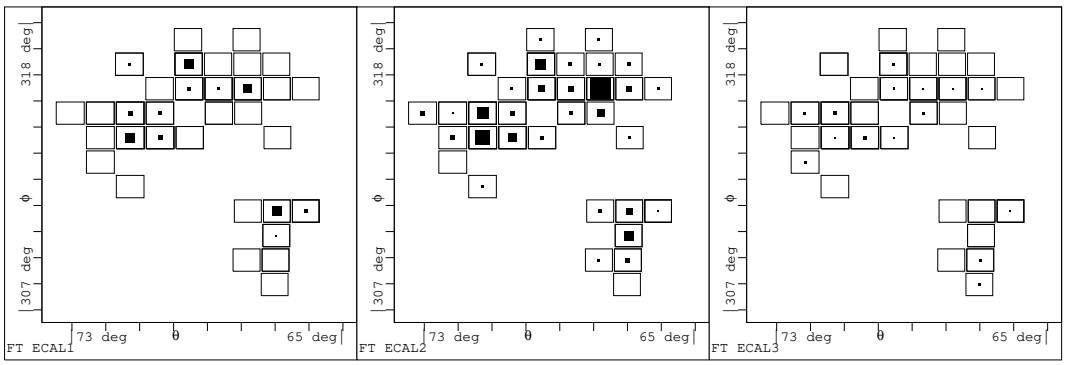

Figure 4.6: *Energy deposits of three photons in ECAL towers; the showers begin in stack 1 (the first picture), they have a maximum in stack 2, and almost completely disappear by stack 3. All towers contributing to the cluster are shown in each stack; empty boxes represent tower storeys containing zero energy.*

to the cluster of their highest energy neighbour, storeys are considered neighbours only when they share a common face. The procedure is repeated for storeys in the second and third stacks but, when processing a storey, the algorithm looks first for a neighbour in the previous stack. G-clusters found by the algorithm are retained as photon candidates only if their energy is greater than 0.25 GeV, and if there is no charged track impact at a distance of less than 2 cm from the G-cluster barycentre. The efficiency and background depend strongly on the density of particle impacts on the calorimeter.

Photon Position Calculation

The position of the photon impact point is given by the G-cluster barycentre i.e. the energy-weighted mean of the coordinates of each storey centre. This position is corrected for biases due to the finite size of the calorimeter cells.

Photon Energy Calculation

In order to reduce the sensitivity of the energy measurement to hadronic background and clustering effects, the photon energy is computed from the energy collected in the four central towers of the cluster, and the expected value of the fraction of energy in the four towers, F_4. This fraction is computed from the parametrisation of the shower shape for a single photon in the calorimeter. The computation takes into account the calorimeter pad area and the distance between the photon impact and the nearest tower corner, as well as the variation with energy of the expected F_4. Corrections to the energy are computed for energy losses before and after the ECAL and energy loss in the region where the

ECAL barrel and endcaps overlap.

π^0 Reconstruction

The reconstruction of neutral pions from G-clusters provides an improvement in purity and efficiency. The identification of subclusters is particularly useful for higher energy pions where the energy deposits of the daughter photons overlap. Discussion of π^0 reconstruction from G-cluster photons will be reserved until Chapter 6 where the methods will be shown in detail as part of the analysis presented in this thesis.

4.5.2 Merged Photons

The probability of resolving a π^0 into two G-clusters decreases for energies greater than 10 GeV. Further information is contained in the distribution, within a single cluster, of the energy in the calorimeter. To extract it, energy weighted moments of the two dimensional energy distribution are computed. Assuming that the cluster contains only two photons, by using moments up to the third order it is possible to reconstruct the two photon momenta and compute their effective mass. This allows a check of the π^0 hypothesis for unresolved high energy clusters. An example of the use of this method can be found in [28].

In this thesis, as the signal-to-background improves at high energy, we do not attempt to reconstruct unresolved high energy clusters.

4.5.3 Converted Photons

An alternative to taking photons from the ECAL is to take converted photons reconstructed in the TPC. About 7% of photons convert in the tracking chambers and are therefore not reconstructed as neutral objects in the ECAL. However, these photons may be reconstructed from their daughter particles identified in the TPC. This provides a much improved energy resolution[1] [29]. This method can be used to reconstruct, for example, Σ° baryons (decaying to $\Lambda\gamma$). However, the method suffers from very low efficiency. The efficiency can be significantly improved, particularly at low energy, by including single arm conversions (where one electron or 'arm' is retained in the material of the detector) though with a loss of energy resolution. Single arm conversions have been used in the reconstruction of B^* mesons (decaying to $B\gamma$) [30].

For neutral pion reconstruction at low energy, converted photons provide π^0 candidates of higher purity than that obtained from ECAL photons [31]. Again,

[1] For low energy photons the improvement is around an order of magnitude.

the problem is the very low efficiency; a combination of converted photons and ECAL photons regains some efficiency though with a reduction in purity.

In this thesis, as the $\rho^{\pm}$ signal width is dominated by its resonant width, the improved momentum resolution gained by reconstructing converted photons is not an advantage. We therefore do not attempt to reconstruct converted photons.

4.6 Event Simulation

For the purpose of model comparison, and as a means of measuring the detector acceptance, a sample of 6.4 million Monte Carlo events are generated with the JESTSET [32] program and passed through a full detector simulation and reconstruction program. After event selection, the number of Monte Carlo events is 4.9 million. The generator is tuned to describe the ALEPH data using the inclusive charged particle and event shape distributions [33].

For further model comparison and as a systematic check for the extrapolation into the unmeasured region, the measured spectra were compared to those of PYTHIA 6.4 [34] and HERWIG 6.5 [35]. The model parameters were tuned using ALEPH data in the same manner as mentioned above.

Event simulation proceeds in two steps: simulation of the physics under investigation (carried out by event generators and the KINGAL program), and simulation of the response of the detector to the KINGAL particles (carried out by the GALEPH program).

4.6.1 KINGAL

The KINGAL package is effectively an interface between the event generators and GALEPH. The event generators use Monte Carlo simulation techniques to produce the desired physics. The KINGAL output gives a 4-vector kinematic representation of each simulated particle. Short-lived resonances are decayed according to decay tables based on experimental data; longer-lived particles are retained so that secondary vertices can be generated in GALEPH.

4.6.2 GALEPH

The Generator for ALEPH (GALEPH) is a detector simulation, representing the interaction of particles with the material of the detector, and the response of the detector to the particles. It generates digitised pulses with the same format as those produced by the data acquisition system.

The GALEPH package uses the GHEISHA package to simulate hadronic showers. Electromagnetic shower simulation is carried out using the GEANT software [36]. Particle scattering as well as energy loss calculations are also carried out by the GEANT package. The quality of the simulation can be seen in the plots presented in Chapter 5, and is further discussed in Chapter 6.

CHAPTER 5

EVENT SELECTION

Approximately 4.2 million hardonic Z^0 decays at center-of-mass energies within ± 2 GeV of the Z^0 peak mass where recorded by ALEPH in the period between 1991 and 1995. After event selection cuts, described in the following sections, the total number of events selected for the analysis is about 3.2 million. Table 5.1 shows the contribution from each year of data taking.

Table 5.1: *Selected hadronic events from each year of data taking.*

Year	Number of hadronic events	LEP Energy $peak-2$, $peak-1$, $peak$, $peak+1$, $peak+2$
1991	223,963	4%, 4%, 82%, 6%, 4%
1992	548,356	100%
1993	528,854	11%, 0%, 72%, 0%, 17%
1994	1,345,422	100%
1995	593,151	8%, 0%, 78%, 0%, 14%
	total: 3,239,746	

Event selection covers two main areas: the first is a selection on event quality, the second is the selection of the hadronic signal $Z \rightarrow q\bar{q}$. These two areas are discussed below in Sections 5.1 and 5.2.

5.1 Data Quality

Several checks are made in an attempt to ensure events are of reasonable quality for analysis. For the real data 'run quality' is assigned to each run period based on checks at various levels. From this information, runs which are passed as good quality for the ECAL and TPC are selected. This includes runs with software fixes for TPC track distortions. Individual events are selected only if the relevant subdetectors have their high voltage on. A small fraction of the selected events (2.6% in 1992 and 0.4% in 1993) have the VDET high voltage off.

Whilst the absence of the VDET in these events produces a visible degradation in tracking performance, particularly the impact parameter resolution, the effect is considered small enough for them to be included.

To remove events which suffer from a low geometric acceptance, a cut is applied on the polar angle of the event axis (with respect to the beam axis) as defined by sphericity. Events are accepted if this angle is in the range $35° < \theta < 145°$ ($|cos\theta| < 0.82$). Figure 5.1 shows the event polar angle distribution for selected[1] hadronic events. The cut ensures that most tracks in an event are well

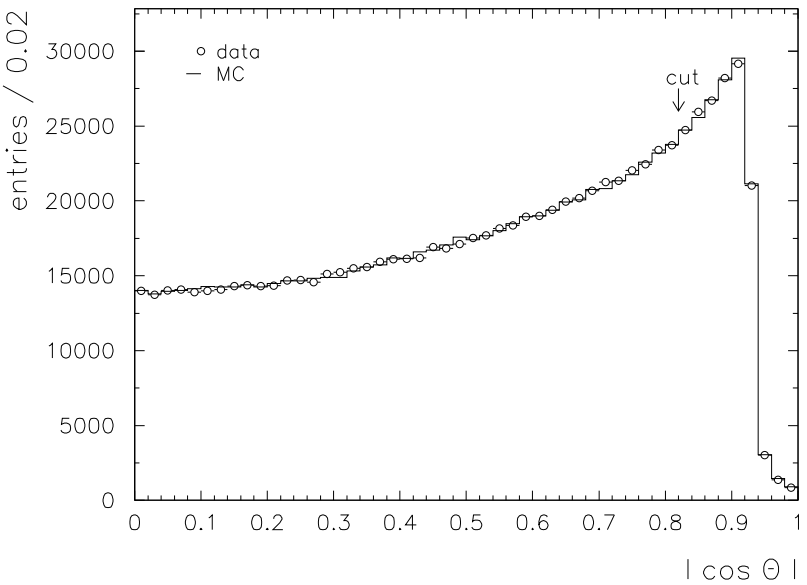

Figure 5.1: *Polar angle of the event axis (with respect to the beam axis) as defined by sphericity for selected hadronic events. For event selection the polar angle θ is required to be in the range;* $35° < \theta < 145°$ *($|cos\theta| < 0.82$).*

contained within the sensitive regions of the detector and therefore gives rise to a large, well defined, acceptance. The sphericity angle cut dominates the efficiency with which hadronic events are selected, reducing the number of hadronic events by 18.6%.

5.2 Hadronic Event Selection

The ALEPH detector records a variety of events, most of which are decays of the Z to its various modes, $\gamma\gamma$ events, and t-channel scattering of electrons. The Z can decay via several channels: $Z \to q\bar{q}$, $Z \to \ell^+\ell^-$ and $Z \to \nu\bar{\nu}$. The reaction $Z \to q\bar{q}$ is suppressed by the invisible reaction $Z \to \nu\bar{\nu}$, and so the more

[1] Here 'selected' means events passing the complete event selection as described in this chapter with the exception of the polar angle cut itself.

species of neutrinos there are, the greater process the $Z \rightarrow q\bar{q}$ is suppressed. Table 5.2 lists the decay modes of the Z [9]. In addition to these there are a small num-

Table 5.2: *Dominant decay modes of the* Z *Boson.*

Z Decay Mode	Fraction (%)
e^+e^-	3.363 ± 0.004
$\mu^+\mu^-$	3.366 ± 0.007
$\tau^+\tau^-$	3.370 ± 0.008
hadrons	69.910 ± 0.060
invisible	20.000 ± 0.060

ber of background processes such as beam-gas interactions, stray beam electrons, cosmic rays and synchrotron radiation. Figure 5.2 shows the reconstruction of a typical hadronic event in the ALEPH detector. The distinguishing feature of hadronic events is the large multiplicity of visible particles, and the large fraction of the center of mass energy that they carry. The hadronic event selection applied here is that used in the Neutral Vector Meson paper [7] and is typical of the hadronic selection which can be found in many ALEPH QCD papers.

5.2.1 Track Cuts

Hadronic events are selected on the basis of the total charged multiplicity and energy within an event. For this, cuts are applied to select 'good' charged tracks, removing some badly reconstructed tracks and ensuring track momenta are well measured and that the tracks originate from the interaction point. This gives rise to a more reliable estimate of the total charged multiplicity and energy and a reasonable agreement with the Monte Carlo.

The selection of 'good' charged tracks is as follows. A track must have:

- at least 4 TPC coordinates
- a polar angle in the range $20^\circ < \theta < 160^\circ$
- a transverse impact-parameter $|d_0| < 2\,\mathrm{cm}$
- a longitudinal impact-parameter $|z_0| < 5\,\mathrm{cm}$
- a transverse momentum $p_t > 200\,\mathrm{MeV}/c$.

After all these cuts the ratio Monte Carlo / real data for the number of tracks selected is 1.0042 ± 0.0002. This agreement illustrates the global tuning

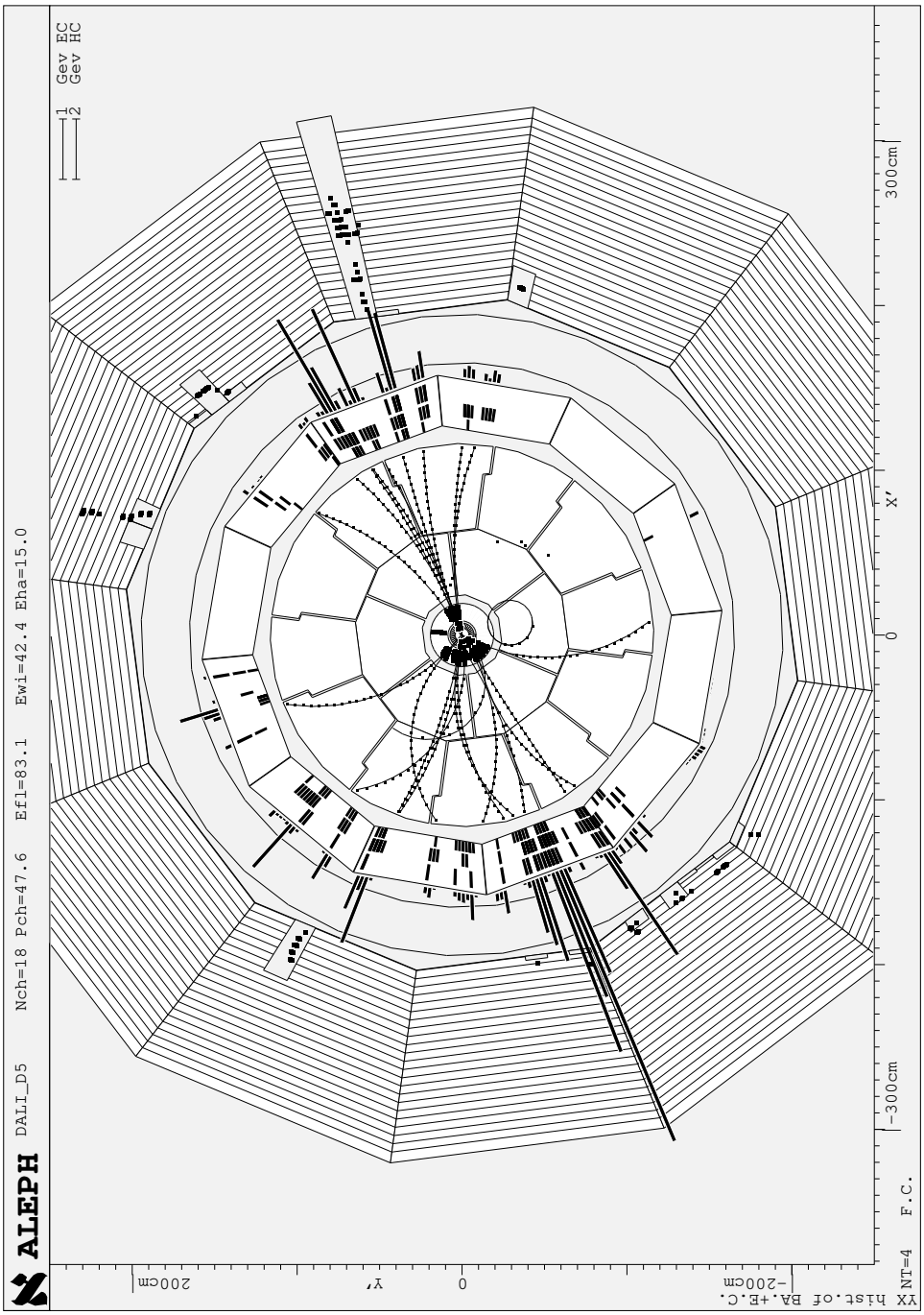

Figure 5.2: *Reconstruction of a typical hadronic event in the ALEPH detector. The distinguishing feature of hadronic events is the large multiplicity of visible particles, and the large fraction of the center of mass energy that they carry. The overall reconstructed energy in this event is 83*GeV*, the charged component totals 48*GeV *from 18 selected tracks.*

of JETSET to fit the ALEPH data. The distributions of the track cuts are shown in Figures 5.3 to 5.6 for selected[2] tracks. The distributions are discussed next.

Number of TPC Coordinates

Figure 5.3 shows the distribution of the number of TPC coordinates for selected tracks. Tracks with no TPC coordinates are those reconstructed only in the ITC, such tracks tend to have a poorly measured z component of their momentum vector. A cut of at least 4 TPC hits provides a starting point for the selection of 'good' charged tracks.

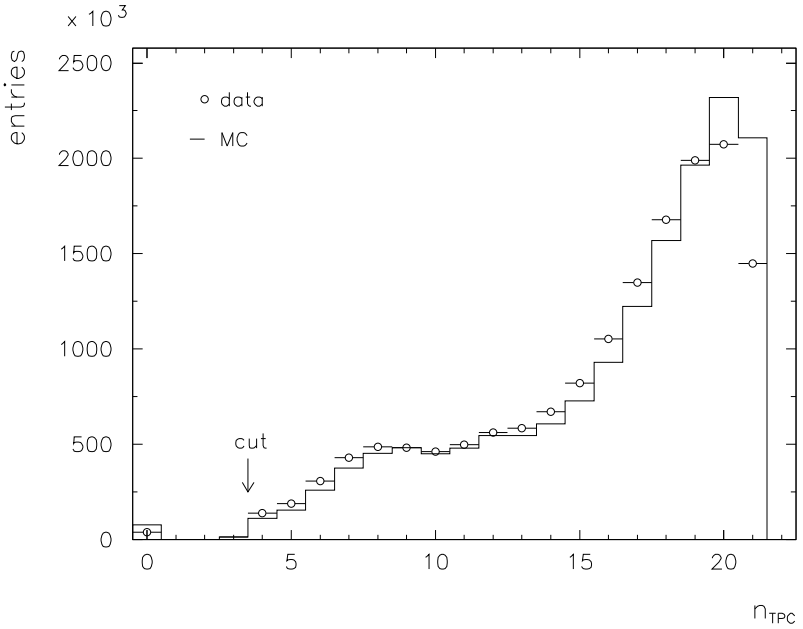

Figure 5.3: *Number of TPC coordinates for selected tracks.*

Polar Angle

Figure 5.4 shows the distribution of the polar angle for selected tracks. The cut is mostly redundant but removes the few tracks whose momentum resolution is very poor due to a small path length in the xy plane of the TPC.

Impact Parameters

Whilst hadronic events typically have a high charged multiplicity, background events normally of low multiplicity can gain additional charged particles, thereby mimicking low multiplicity hadronic events, due to a variety of processes. These processes involve interactions with the material of the detector

[2] Here 'selected' means tracks passing all other track cuts and events are selected as described in Section 5.1.

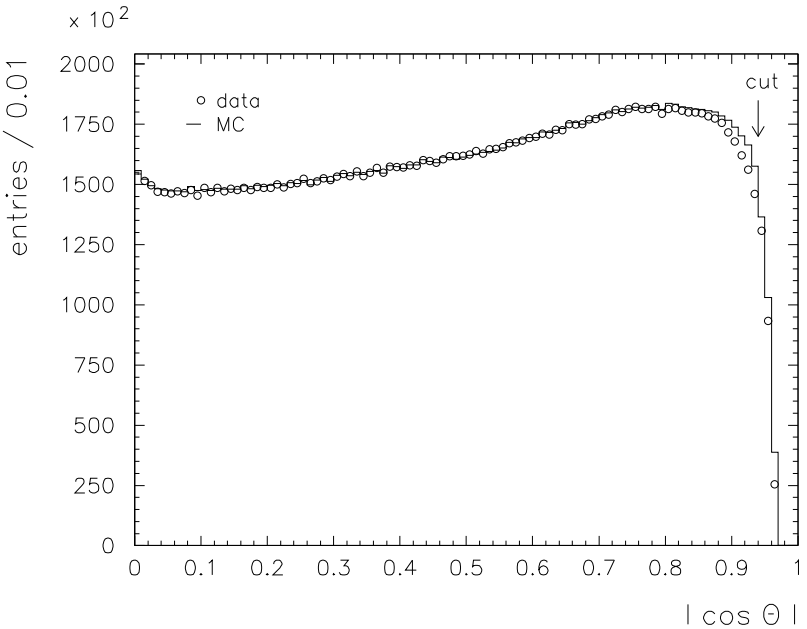

Figure 5.4: *Polar angle for selected tracks.*

such as nuclear interactions, photon conversions, back-scatter of particles from the ECAL. Tracks can also be gained by the failure to link successive turns of spirals, the decay of charged tracks, the return of spiraling tracks into the TPC, and 'imaginary' tracks constructed by JULIA from bad or incorrectly assigned TPC hits. These processes usually result in tracks which do not point back to the interaction point, thus their effects can be minimised by making cuts on the track impact parameters d_0 and z_0.

Figures 5.5 and 5.6 show the distribution of the impact parameters for selected tracks. The cuts are loose (Figures 5.5b and 5.6b) allowing tracks originating from decays away from the interaction point, for example B meson decays, to be selected. Figures 5.5c and 5.6c show the ratio real data / Monte Carlo for the distributions. The Monte Carlo has a tighter distribution for both d_0 and z_0. For the d_0 cut the real data initially selects $\approx 5\%$ less tracks in the $\pm 0.05\,\mathrm{cm}$ region, an excess is seen for larger values of d_0 and by $|d_0| = 0.5\,\mathrm{cm}$ the number of tracks in the Monte Carlo compared to the number in the real data agrees to $\approx 0.7\%$, by $|d_0| = 2.0\,\mathrm{cm}$ the agreement is $\approx 0.1\%$. The z_0 distribution shows a similar behaviour though this is less sensitive due to its much wider distribution.

Transverse Momentum

Figure 5.7 shows the distribution of the transverse momentum for selected tracks. Applying a p_t cut of $200\,\mathrm{MeV/c}$ removes tracks which turn tightly in the TPC. Since such tracks do not transverse many TPC pad rows, they therefore suffer from a poor momentum resolution.

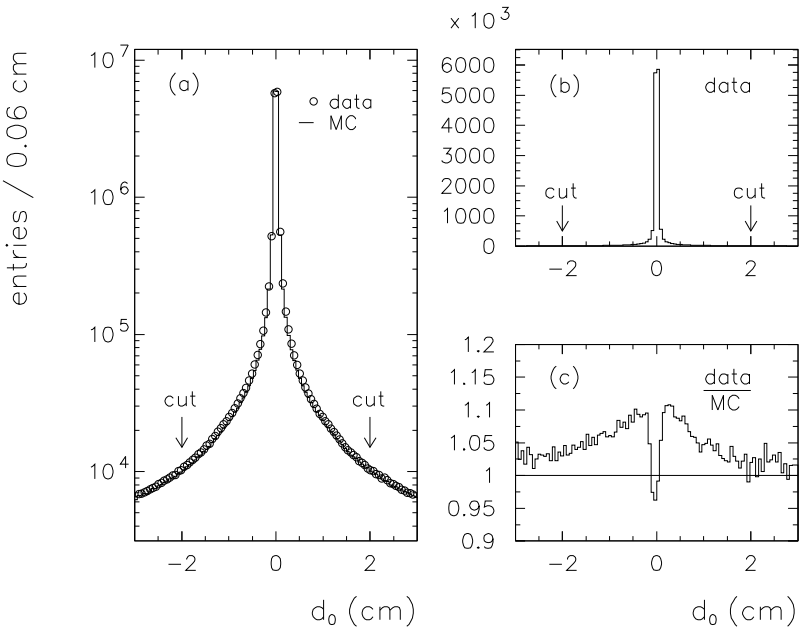

Figure 5.5: *Transverse impact parameter for selected tracks. (a) Monte Carlo and real data compared: the distribution in real data is wider than that in the Monte Carlo. (b) The cut of* 2 *cm is loose allowing tracks from heavy flavour decays away from the interaction point to be selected. (c) the ratio real data / Monte Carlo shows the wider distribution in the real data.*

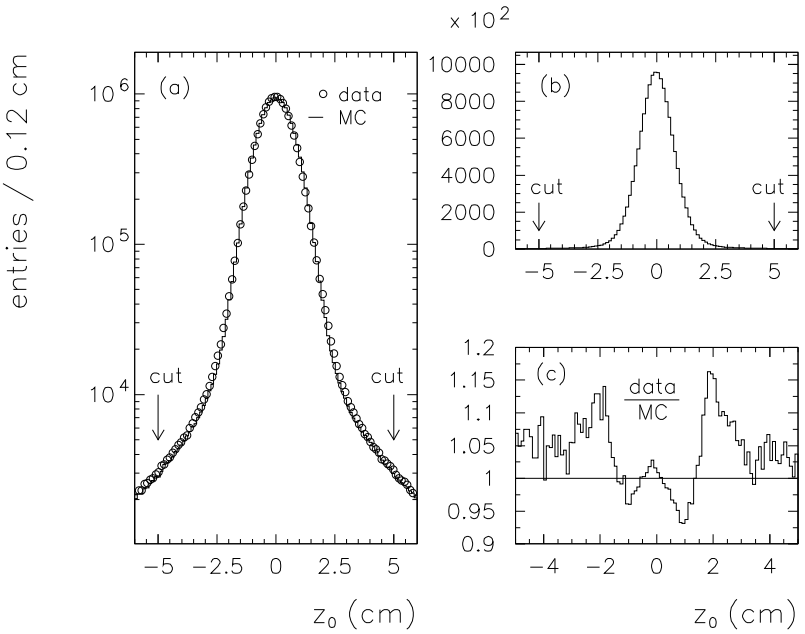

Figure 5.6: *Longitudinal impact parameter for selected tracks. Figures (a), (b) and (c) follow the same form as Figure 5.5. The ratio real data / Monte Carlo shows the wider distribution in the real data. The cut is loose reducing the effect of the discrepancy.*

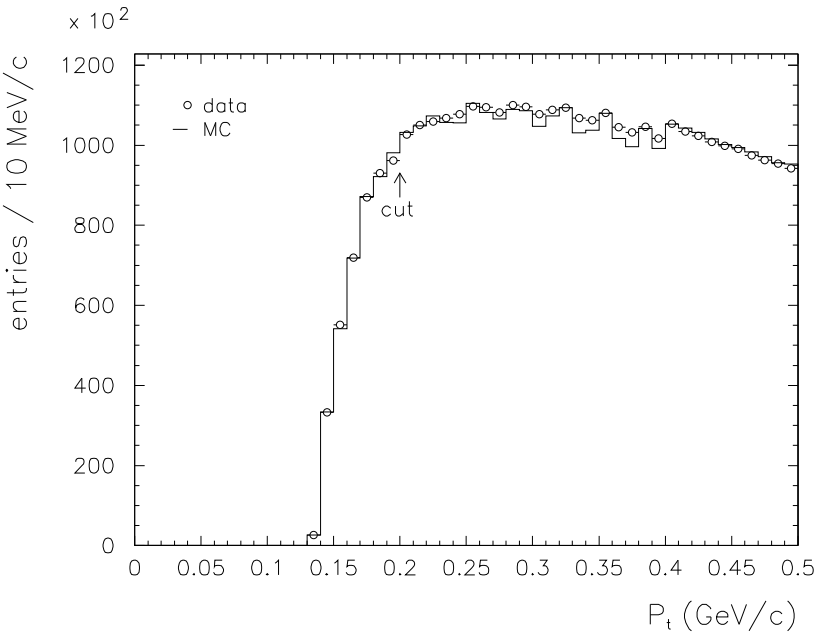

Figure 5.7: *Transverse momentum for selected tracks. a cut of 200 MeV/c is applied to ensure a reasonable momentum resolution.*

5.2.2 Event Cuts

Figure 5.8 shows the event charged energy[3] versus the event charged multiplicity for events in the real data after applying the event sphericity angle cut. A clear separation of the hadronic event types can be seen. The hadronic signal is selected with an efficiency of 94.9% and a purity of 99.6% by requiring events to have:

- a minimum of 5 'good' charged tracks, and
- a minimum of 15 GeV total 'good' charged energy.

The track multiplicity cut removes $Z \rightarrow l\bar{l}$ events. Most $\gamma\gamma$ events are removed with the event polar angle cut, the rest are removed by the charged energy cut. Figures 5.9a and 5.9b show a good agreement between Monte Carlo and real data for the charged energy and multiplicity distributions for the selected events[4] . All event selection criterias has been summarised in Figure 5.10.

5.3 Event Background

The level of background after event selection is dominated by tau events with a small contribution from $\gamma\gamma$ events. Background from other processes such

[3] The pion mass is assumed for all charged tracks.

[4] A good agreement is expected as the tuning of the Monte Carlo relies to a great extent on measurements in the real data of charged track distributions.

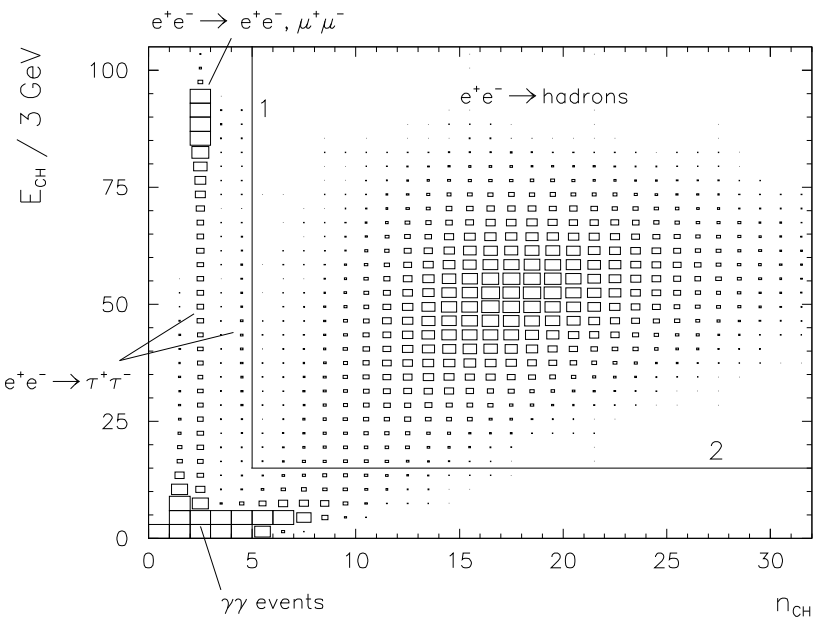

Figure 5.8: *Charged energy, E_{CH}, versus charged multiplicity, n_{CH}, for events in real data after 'good' charged track and event polar angle cuts have been applied. The hadronic signal is selected by requiring at least* 5 *good charged tracks (cut 1) and a charged energy of at least* 15 *GeV (cut 2).*

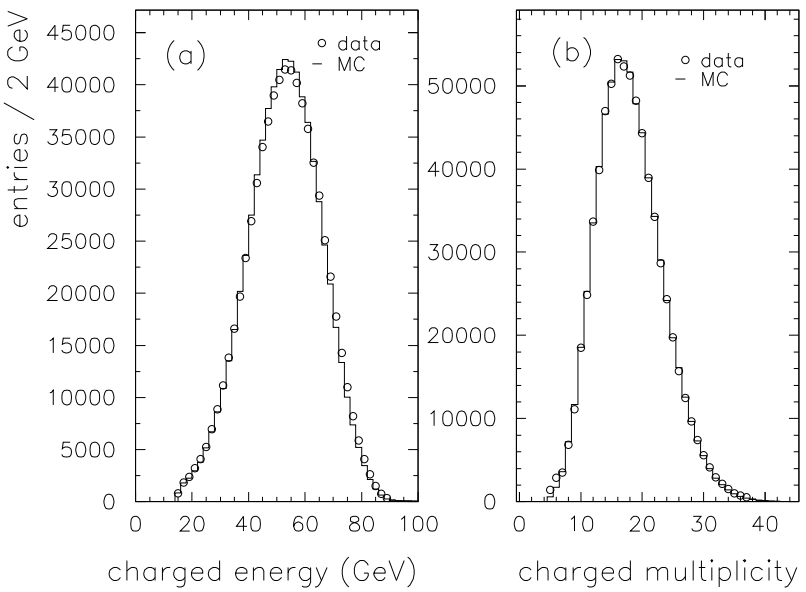

Figure 5.9: *Charge distributions for selected events, a) charged energy, and b) charged multiplicity. The Monte Carlo is in good agreement with the real data.*

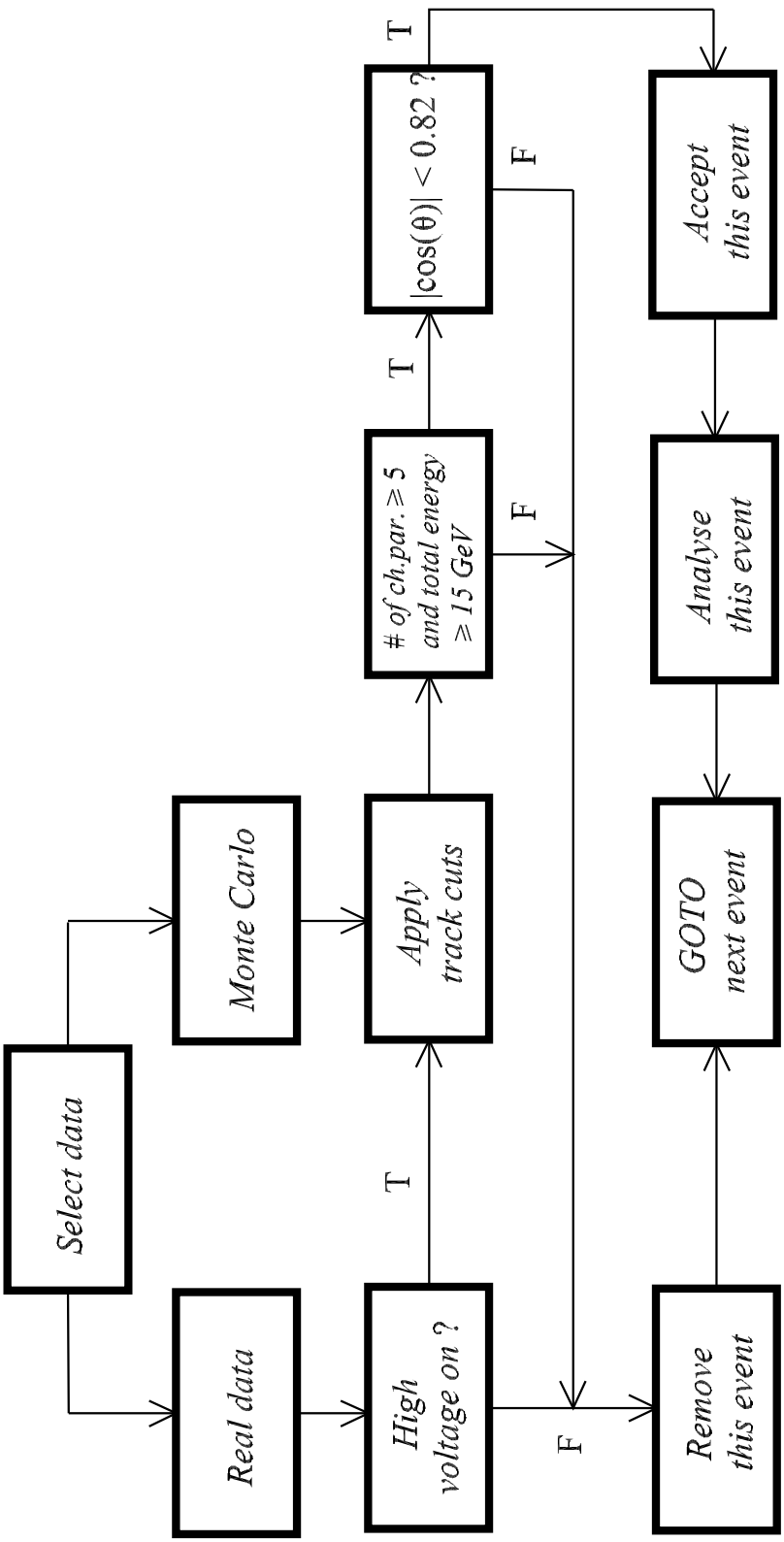

Figure 5.10: *Flow chart of hadronic event selection.*

as decays of the Z to e^+e^- and $\mu^+\mu^-$, t-channel scattering of beam electrons, beam-gas, and cosmic rays are much smaller [37]. From Monte Carlo studies the contributions to the selected events are given in Table 5.3.

Table 5.3: *The contributions of the hadronic and background events obtained from Monte Carlo.*

Selected event	Contribution in %
Hadronic	99.625 ± 0.001
Tau	0.325 ± 0.002
$\gamma\gamma$	0.050 ± 0.004

Without the cut on the event angle, the contribution from $\gamma\gamma$ events would be comparable with that from tau events. The rate of $\rho^{\pm}$ production in tau events is much smaller than that in hadronic events.

CHAPTER 6

TRACK SELECTION FOR THE ANALYSIS

6.1 Introduction

Particle identification is important to reduce the combinatorial background and the size of reflections. In this chapter, the selection of charged and neutral pions for the analysis of $\rho^{\pm}$ mesons, in decay channel $\rho^{\pm} \rightarrow \pi^{\pm} + \pi^{0}$, is described, and the results are presented. The selection of charged pions is relatively trivial, while neutral pion selection and reconstruction is much more complicated. All selection performances are determined from Monte Carlo studies with aim to maximise both *purity* and *efficiency*.

6.2 Charged Track Selection

The charged track selection for analysis involves cuts on the same parameters as in the track selection for event selection. The polar angle and TPC coordinate multiplicity cuts are kept the same. The impact-parameter cuts are tightened considerably to increase the purity of selected charged pions originating from $\rho^{\pm}$ decays. A small increase in the p_t cut is introduced to improve the agreement in the impact parameter distributions and remove poorly measured tracks. Additionally, two cuts are applied to the χ of ionisation energy loss, dE/dx, so as to remove some kaon and proton backgrounds. The charged track selection for the analysis is as follows:

- at least 4 TPC coordinates
- a polar angle in the range $20^{\circ} < \theta < 160^{\circ}$
- a transverse impact-parameter $|d_0| < 0.5$ cm

- a longitudinal impact-parameter $|z_0| < 3.0$ cm
- a transverse momentum $p_t > 250\,\mathrm{MeV}/c$.
- if available, $-2 < \chi(\mathrm{dE/dx}) < 3$ (with the $\pi^{\pm}$ hypothesis)

After all these cuts the ratio Monte Carlo / real data for the number of tracks selected is 1.0031 ± 0.0002. The details of applying the cuts are described in the following sections.

6.2.1 Impact Parameters

Tight cuts on the impact parameters are introduced to increase the reconstructed purity of $\pi^{\pm}$ mesons from $\rho^{\pm}$ mesons owing to the following reasons:

(1) About 60% of the $\rho^{\pm}$ mesons originate from the string (interaction point). The mean lifetime of a $\rho^{\pm}$ meson is $\tau = 4.3 \times 10^{-24}$ s and corresponding $c\tau$ value is 1.3 fm, that is originating from the interaction point. The remaining 40% are originating from decays such as B and D mesons having $c\tau$ less than 0.5 mm. The list of dominant $\rho^{\pm}$ sources and their $c\tau$ values are given Table 6.1. Charged pions from $\rho^{\pm}$ in all these sources are expected to have small d_0 values. This is illustrated in Figure 6.1 where the Monte Carlo are shown after all other track cuts applied except for $\chi(\mathrm{dE/dx})$ cut.

(2) The tight cuts remove tracks from the decays of neutral hadrons away from the interaction point, mostly K^0_S, and tracks from photon conversions. Figure 6.1 shows the Monte Carlo d_0 distributions, for background particles are much wider than for pions from $\rho^{\pm}$ decays.

According to Monte Carlo studies, the hard cuts $|d_0| = 0.5$ cm and $|z_0| = 3.0$ cm remove significant number of electron, muon and pion backgrounds, but remove less than 2% of pions from $\rho^{\pm}$.

Table 6.1: *Some $\rho^{\pm}$ sources and their $c\tau$ values.*

Particle	Sample decay channel	$c\tau$ (mm)
$B^{\pm}$	$B^{\pm} \to \overline{D^0} + \rho^{\pm}$	0.49
B^0	$B^0 \to D^{\mp} + \rho^{\pm}$	0.46
$D^{\pm}$	$D^{\pm} \to \overline{K^0} + \rho^{\pm}$	0.31
D^0	$D^0 \to K^{\mp} + \rho^{\pm}$	0.12

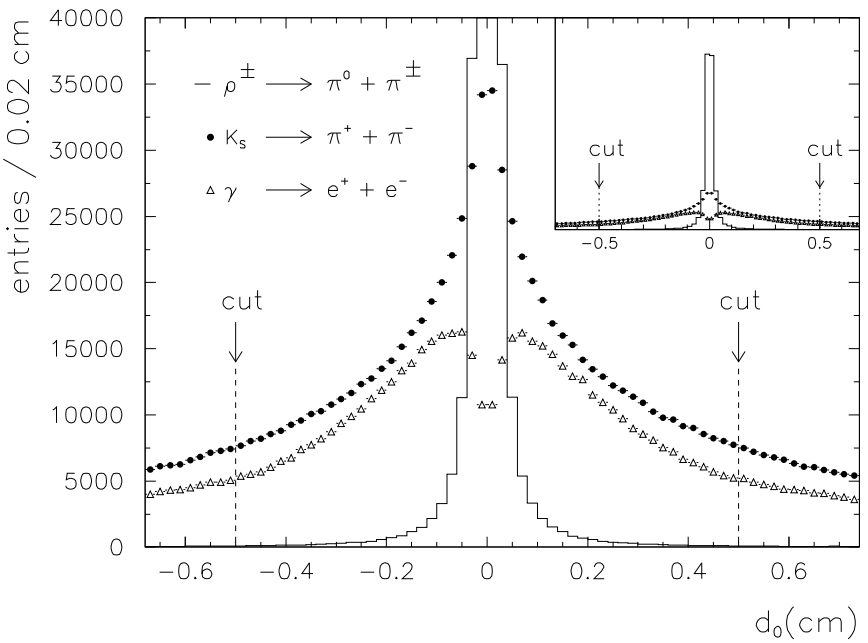

Figure 6.1: *Transverse impact parameter distributions for reconstructed tracks from $\rho^{\pm}$, K^0_S, and photon conversions, after all other track cuts, execpt for* χ(dE/dx)*, have been applied.*

6.2.2 Transverse Momentum

The cut on the transverse momentum is increased from 200 MeV/c to 250 MeV/c. The cut improves the average reconstructed momentum resolution (see Section 6.4.4) and the agreement between Monte Carlo and real data for the impact parameter distributions.

6.2.3 Ionisation Energy Loss

Charged particle identification is performed by the measurement of ionisation energy loss, dE/dx. A particle's energy loss is sampled in the TPC by up to 338 wires. The deviation from an assumed hypothesis is expressed as χ(dE/dx):

$$\chi(\mathrm{dE/dx}) = \frac{(\frac{\mathrm{dE}}{\mathrm{dx}})_{\mathrm{measured}} - (\frac{\mathrm{dE}}{\mathrm{dx}})_{\mathrm{expected}}}{\sigma_{\mathrm{dE/dx}}} \tag{6.1}$$

where $\sigma_{\mathrm{dE/dx}}$ is the expected dE/dx resolution normalised with a sample of minimum ionising pions. Note that, not all charged tracks have dE/dx information. Figure 6.2 shows the measured dE/dx as a function of particle momentum for electrons, muons, poins, kaons and protons.

Figure 6.3a shows χ(dE/dx) distributions of all charged particles for Monte Carlo and real data according to the $\pi^{\pm}$ hypothesis[1] , the Monte Carlo predictions

[1] i.e. the mass of charged pion is assigned to all charged particles.

for the pions, kaons and protons are demonstrated as well. In Figure 6.3b, the χ(dE/dx) distribution for charged pions from $\rho^{\pm}$ decays are compared to the distributions for non-pionic charged particles. Two cuts are applied in the selection of $\pi^{\pm}$ candidates. The cut positions are optimised such that the product of the selection efficiency (ε) $\times$ purity ($\mathcal{P}$) of the pions is maximum. The optimum cuts correspond to a selection of the charged particles within $-2 < \chi(\mathrm{dE/dx}) < 3$.

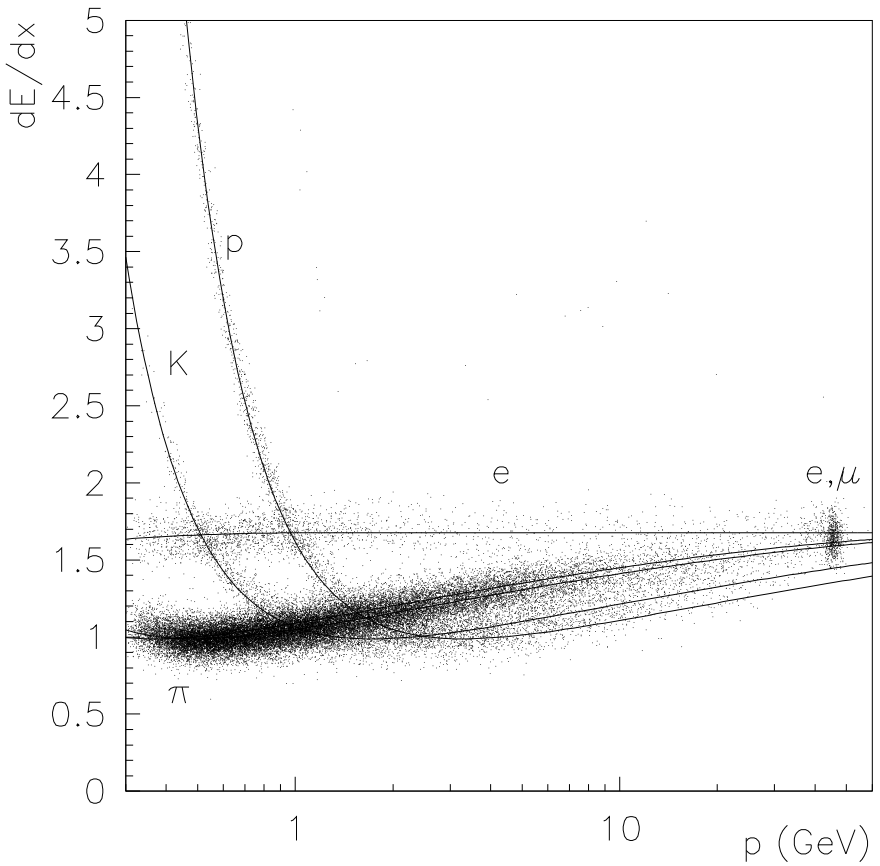

Figure 6.2: *Measured* dE/dx *versus particle momentum for electrons, muons, poins, kaons and protons.*

After the cuts of χ(dE/dx) are applied, about 40% of kaons and 65% of protons are removed, and only 2% of pions from $\rho^{\pm}$ are removed. This is illustrated in Figure 6.3b. Together, the cuts applied on impact parameters and χ(dE/dx) allow us to select pions from $\rho^{\pm}$ mesons with 96% efficiency.

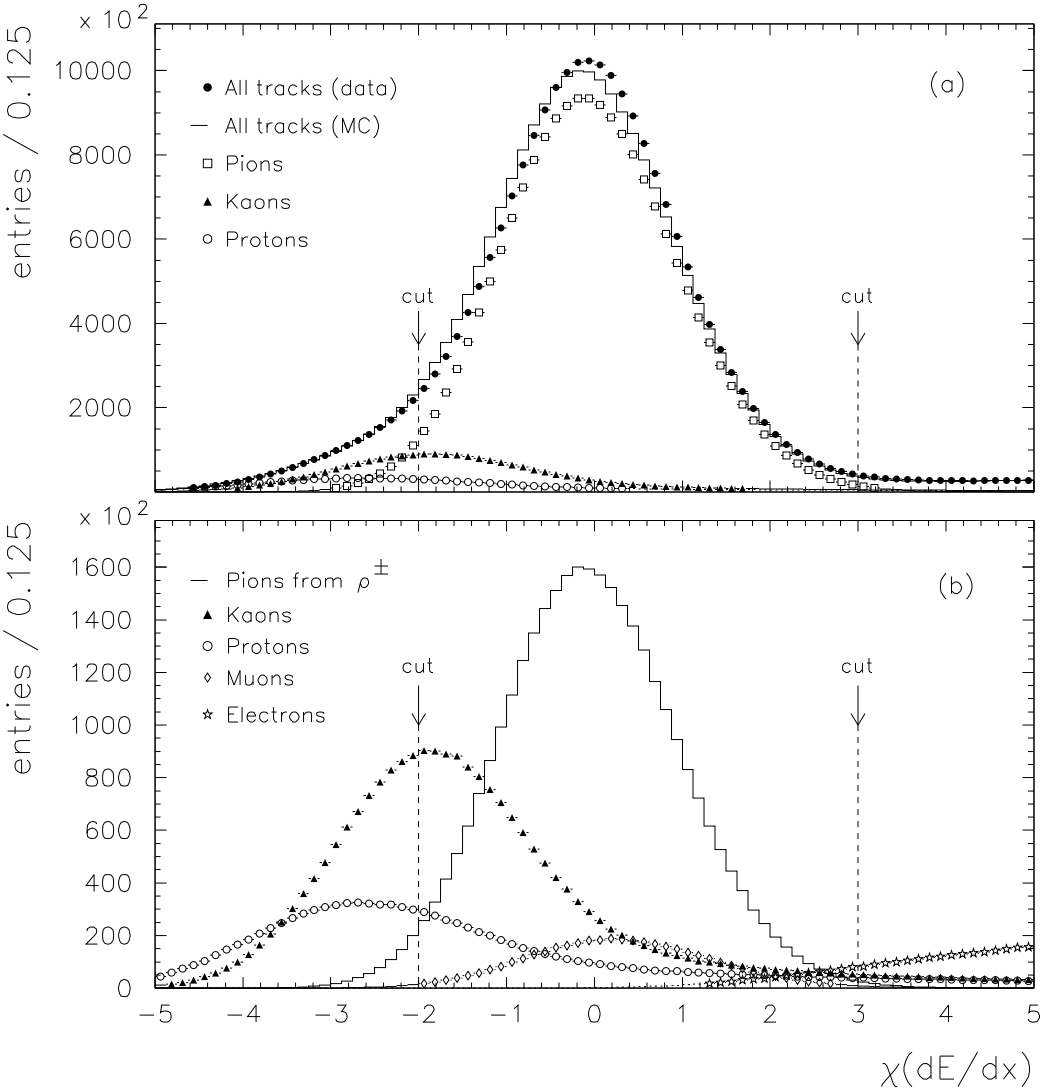

Figure 6.3: χ(dE/dx) *distributions according to the* $\pi^{\pm}$ *hypothesis, and the optimum cuts selecting pions from* $\rho^{\pm}$ *with 98% efficiency. (a) Comparison of Monte Carlo and real data, and Monte Carlo predictions for all tracks* $\pi^{\pm}$, $K^{\pm}$ *and* $p\overline{p}$. *(b) Monte Carlo predictions for each species. After these cuts a large number of the kaons, protons and electrons are removed while keeping most of the pions. However, muons cannot be eliminated since the muon mass is very close to pion mass.*

6.3 Neutral Pion Selection

6.3.1 π^0 Reconstruction

Neutral pions decay to two photons ($\pi^0 \rightarrow \gamma\gamma$) with a branching ratio of $98.798 \pm 0.032\%$ [9]. For this analysis, photons are reconstructed using the ECAL; photons converting to an e^+e^- pair within the material of the detector, 7% on average, are not selected. π^0 candidates are selected from invariant mass distributions of pairs of photons. Invariant mass spectra are formed using the equation[2]

$$M^2 = 2E_1E_2(1 - \cos\theta_{12}) \tag{6.2}$$

where M is the invariant mass of the reconstructed photons whose energies are E_1 and E_2 measured in the ECAL, and θ_{12} is the angle between two photons. Candidates are either true, forming a pion signal, or false, forming a combinatorial background. This is illustrated in Figure 6.4.

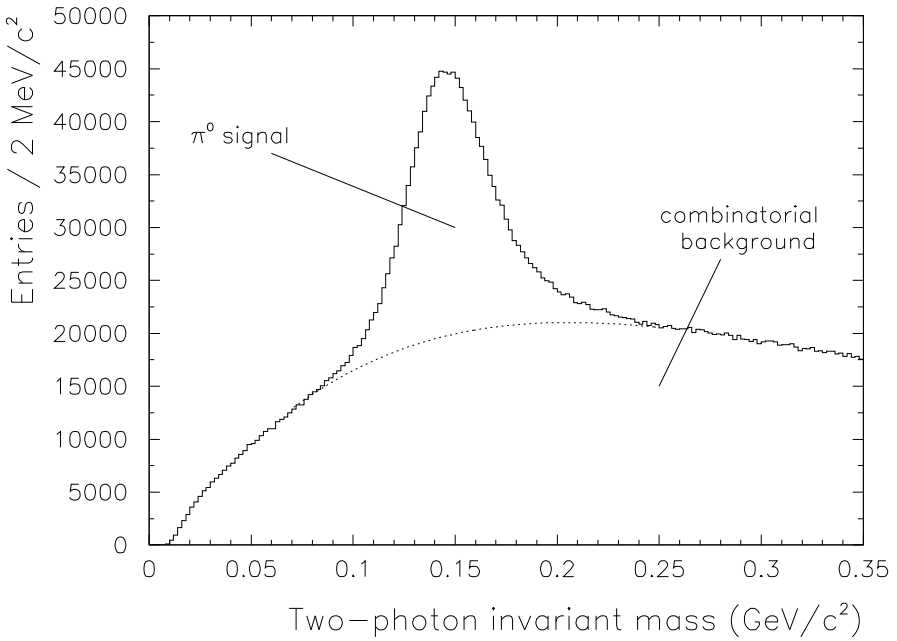

Figure 6.4: *An example of the invariant mass of photon pairs around a π^0 peak. Correct combinations of photon pairs result in a peak representing the π^0 signal, incorrect combinations result in a combinatorial background (doted line).*

[2] The derivation can be found in Appendix A.

6.3.2 Photon Selection

Photon candidates are selected from electromagnetic clusters. A 1 GeV cut on the photon energy is applied for both barrel and endcap regions of the ECAL in order to gain a reasonable agreement between the Monte Carlo and real data to avoid large systematic errors in the efficiency correction. A cut on photon energy also improves π^0 purity, especially importrant for the reconstruction of the $\rho^{\pm}$ at low momentum. Figure 6.5 shows the energy spectrum of photons in the ECAL, barrel, and endcap regions. In the lower energy zone, the distributions differ significantly between Monte Carlo and real data. After 1 GeV, distributions are in much better agreement each other.

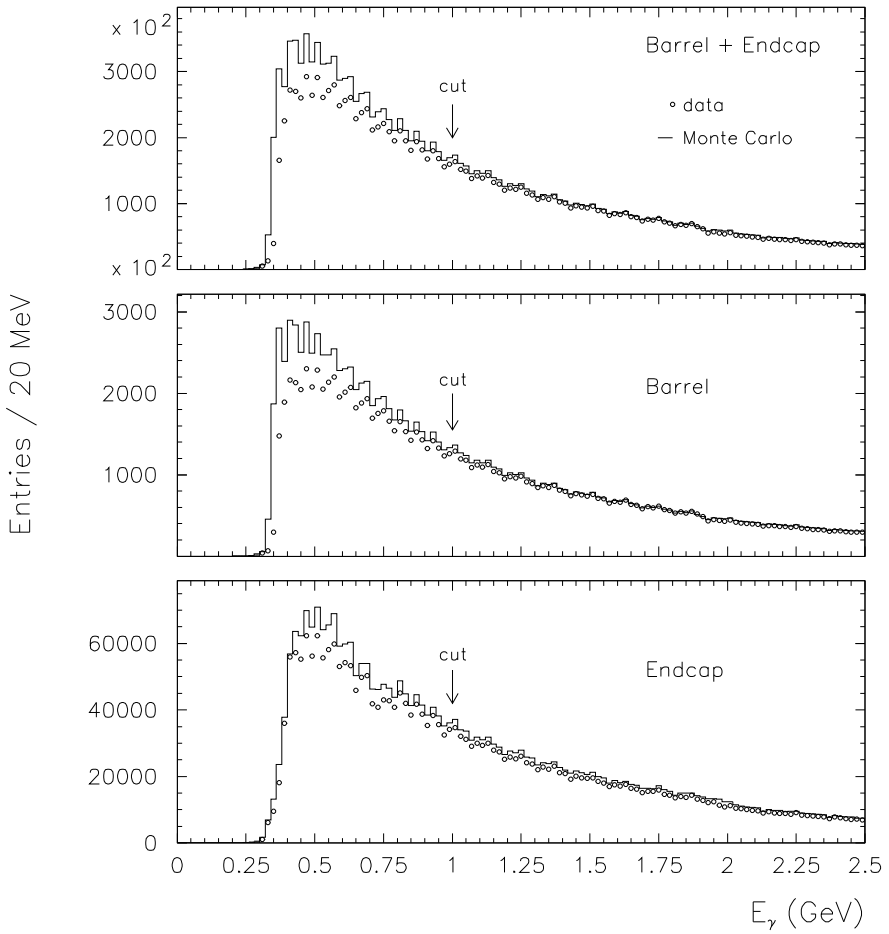

Figure 6.5: *Energy distributions for photons in (a) the ECAL, (b) the endcap and (c) the barrel regions. Low energy photons are not modelled very well, especially in barrel region.*

Improvements in the agreement between the Monte Carlo and real data after the 1 GeV photon energy cut are also clear in the polar angle distribution for photons, Figure 6.6.

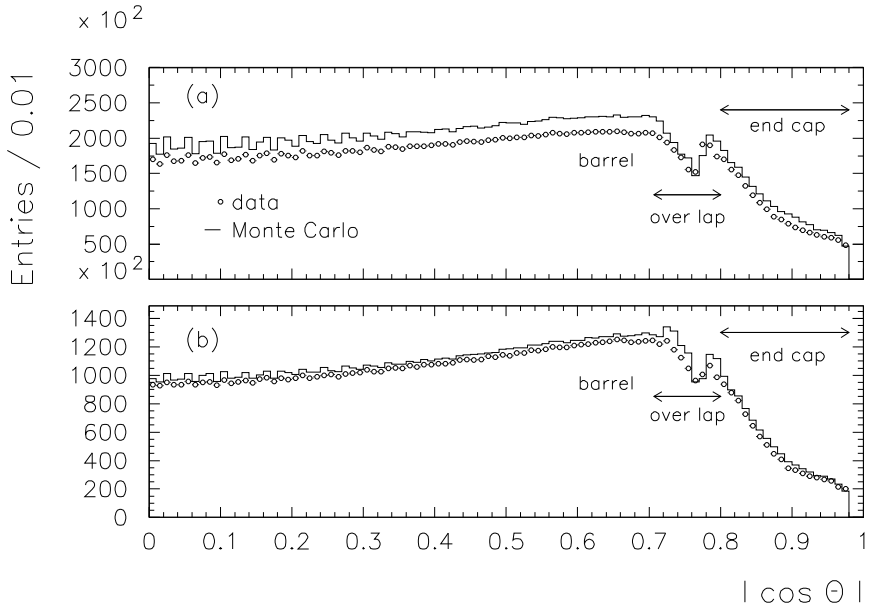

Figure 6.6: *Polar angle distribution of photons, (a) before the cuts on photon energy, (b) after the photon energy cut of 1 GeV.*

6.3.3 π^0 Energy

The lower energy bound for π^0 candidates is 2 GeV, i.e. twice the photon energy cut. An upper bound of 18 GeV is introduced to remove the uncertainties in the efficiency correction for very high energy π^0s. The determination of π^0 efficiencies is discussed in detail in Chapter 10.

6.3.4 π^0 Topology

Invariant mass spectra are formed from pairs of photons passing the photon selection criteria. The topology of the reconstructed π^0 is found to be important. Four topologies, illustrated in Figure 6.7, are defined[3] as follows:

- topology 1: photon pairs taken from one ECAL cluster within which two subclusters are resolved.
- topology 2: photon pairs taken from one ECAL cluster within which more than two subclusters are resolved.
- topology 3: photon pairs taken from two ECAL clusters, within each of which no subclusters are resolved.

[3] For these definitions, 'resolved subclusters' are counted if they have at least 0.3 GeV energy.

- topology 4: photon pairs taken from two ECAL clusters, within one or both of which more than one subcluster is resolved.

Topologies 1 and 3 are known as 'clean' topologies as they have no additional subclusters associated to them. Topologies 2 and 4 are 'unclean' as they are contaminated by the chance merging of photons from different π^0s or 'fake' photons from various processes such as fragmenting showers and remnants of neutral hadrons whose shower begins in the ECAL.

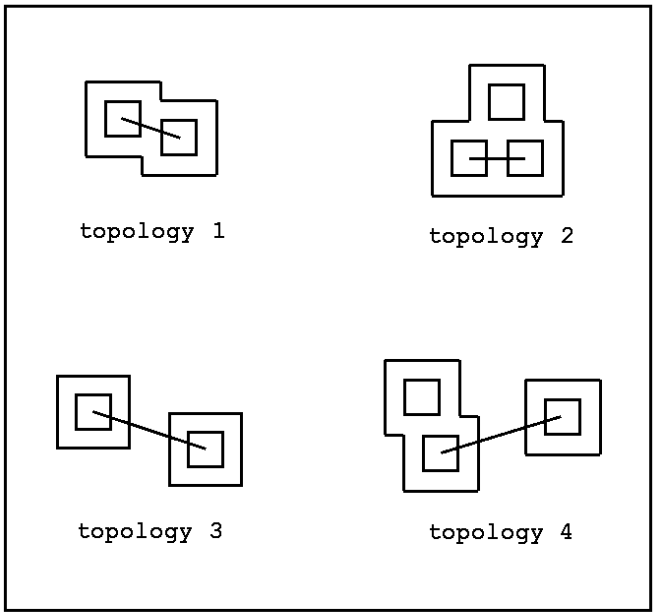

Figure 6.7: *Geometric representation of four possible π^0 topologies.*

6.3.5 π^0 Mass Window

The π^0 signal is selected from a mass window whose peak position and width vary as a function of the reconstructed π^0 energy and topology. The width of the window is taken as $\pm\ 2\sigma$, where σ is the half width at half height for the reconstructed π^0 signal. The reconstructed mass and width must be carefully calibrated, this procedure is discussed in detail in Chapter 7.

6.3.6 π^0 Ranking

A crucial step in the extraction of the $\rho^{\pm}$ signal is the improvement in the purity of selected π^0 candidates. The poor purity at low momentum is due to the large multiplicity of low energy photons giving rise to a large combinatoric background. The purity is improved by a 'ranking' method; all π^0 candidates that share photons with other candidates are ranked in an order determined by

a π^0 estimator based on the photon pair opening angle θ_{12} and the χ^2 value from the mass constraint. The details of Ranking can be found in Chapter 8.

6.3.7 π^0 Mass Constraint

Uncertainties in the reconstructed momentum vector of a π^0 are introduced due to the finite ECAL spatial and energy resolution. By making use of the relation:

$$m_r^2 = 2E_1E_2\,(1 - \cos\theta_{12}) \tag{6.3}$$

relating the reconstructed π^0 mass m_r to the reconstructed photon energies E_1 and E_2 and their opening angle θ_{12}, the momentum of π^0 candidates can be refitted [38] by constraining their mass to the nominal π^0 mass, 135 MeV/c^2. This improves the momentum resolution and leads to a significant increase in the signal significance. Two different refitting methods are used depending on the topology of the π^0 candidate. Detailed mathematical formulations can be found in Appendix B.

Method 1

For π^0 topologies 3 and 4 (low energy π^0s) the photon opening angle is large, and the uncertainty in the reconstructed momentum is almost entirely due to the photon energy resolution. For the refitting, only the photon energies E_1 and E_2 are allowed to vary, whilst their directions are kept fixed. The calculation is done with the technique of Lagrange multipliers (see App. B.3.1). The photon energies are re-evaluated by minimising χ^2. Since the exact solutions to the minimisation are complex only approximate solutions are taken. The photon energies are rescaled and the π^0 invariant mass recalculated. The whole procedure is repeated until the reconstructed invariant mass is within $\pm 10^{-4}$ MeV/c^2 of the nominal π^0 mass. If the original reconstructed invariant mass is close to the nominal π^0 mass then usually only one iteration is required, the number increases for reconstructed masses further away from the nominal mass.

Method 2

For topologies 1 and 2 (high energy π^0s) the photon pair opening angle is small and so the angular resolution is no longer negligible compared to the energy resolution. Also, for these topologies the opening angle is overestimated, resulting in an underestimate of the π^0 energy. The effect increases with energy and is corrected for in the refit. In the refitting procedure E_1, E_2 and $\cos\theta_{12}$

are allowed to vary. The minimisation of the χ^2 is performed by the Newtonian method (see App. B.3.2).

6.4 Reconstruction Performances

Details of reconstruction efficiency, purity and momentum resolution, have a direct effect on the reconstructed $\rho^{\pm}$ signal significance. Reconstruction performances for selected pions are determined from Monte Carlo studies, some distributions are presented in the following sections.

6.4.1 Momentum and Energy Distributions

The momentum spectra of generated and reconstructed $\pi^{\pm}$, and energy spectra of π^0s, are given in Figure 6.8. For these plots, no upper energy is applied to the π^0s. The distributions help us to form the purity and efficiency distributions of the pions.

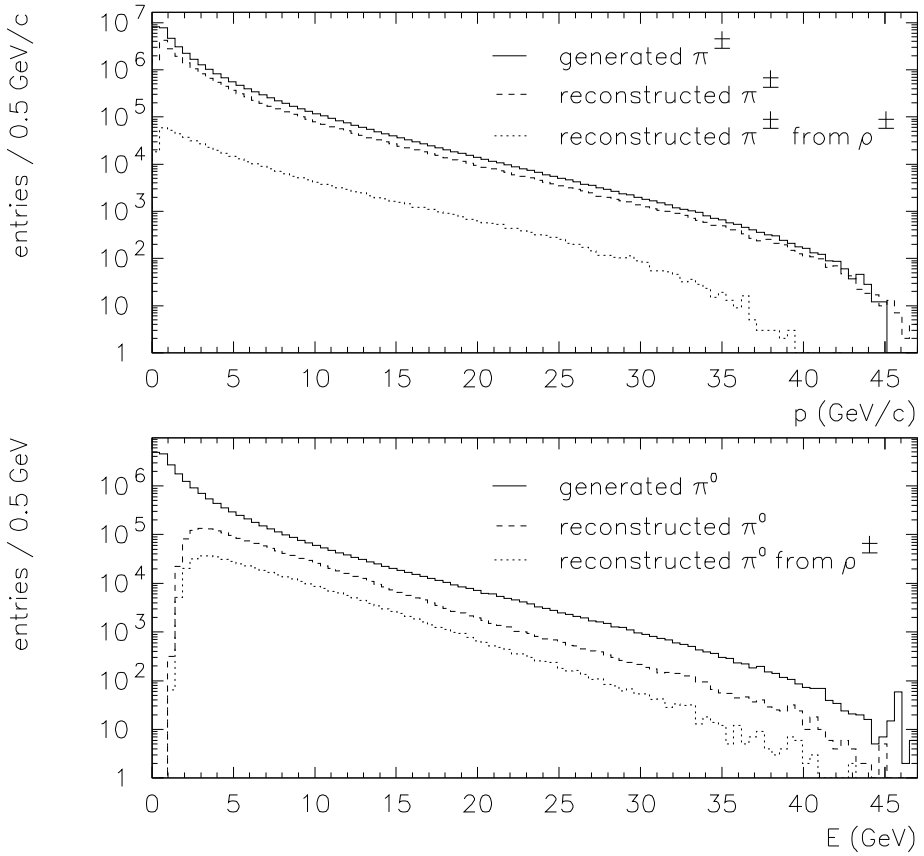

Figure 6.8: *Momentum distributions of $\pi^{\pm}$s, and energy distributions of π^0s.*

6.4.2 Pion Purity

The purity, $\mathcal{P}$, of the selected $\pi^{\pm}$s and π^0s are defined as follows:

$$\mathcal{P}_{\pi^{\pm}} \equiv \frac{\text{number of reconstructed good charged tracks matched to } \pi^{\pm}}{\text{number of reconstructed good charged tracks}}$$

$$\mathcal{P}_{\pi^0} \equiv \frac{\text{number of reconstructed } \pi^0 \text{ candidates matched to } \pi^0}{\text{number of reconstructed } \pi^0 \text{ candidates}}$$

In Figure 6.9 the purity of the selected charged pions is shown. The purity is initially about 100% falling gradually with increasing momentum. For charged pions from $\rho^{\pm}$ decays, the purity is initially 1% increasing slowly with increasing momentum and decreasing rapidly at very high energy.

In Figure 6.10 the purity of selected neutral pions is shown. The purity is initially very low due to the large combinatorial background at low energy. The purity rises with energy peaking at 80%. A similar behavior is seen for π^0s from $\rho^{\pm}$ decays.

6.4.3 Pion Efficiency

The selection efficiency, ε, of $\pi^{\pm}$s and π^0s can be defined as follows:

$$\varepsilon_{\pi^{\pm}} \equiv \frac{\text{number of reconstructed good charged tracks matched to } \pi^{\pm}}{\text{number of } \pi^{\pm} \text{ generated at the truth level}}$$

$$\varepsilon_{\pi^0} \equiv \frac{\text{number of reconstructed } \pi^0 \text{ candidates matched to } \pi^0}{\text{number of } \pi^0 \text{ generated at the truth level}}$$

The selection efficiency for charged and neutral pions are shown in Figure 6.11 and 6.12. The generated and reconstructed $\pi^{\pm}$ momentum and π^0 energy spectra are shown in Figure 6.8.

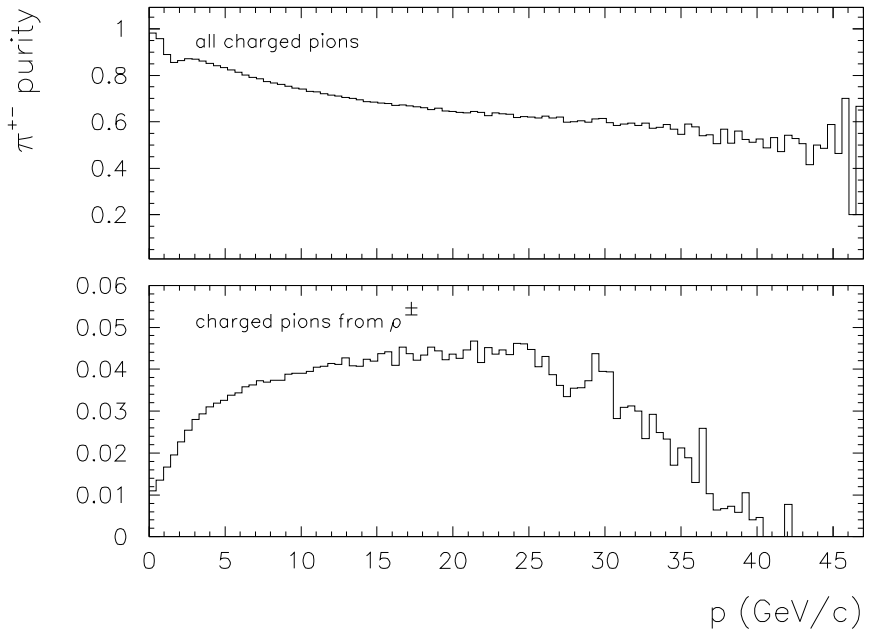

Figure 6.9: *Purity of reconstructed charged pions as a function of momentum for all pions, and pions from the $\rho^{\pm}$ meson. The maximum $\rho^{\pm}$ pion purity is about 4% and falls rapidly to zero at 40 GeV/c.*

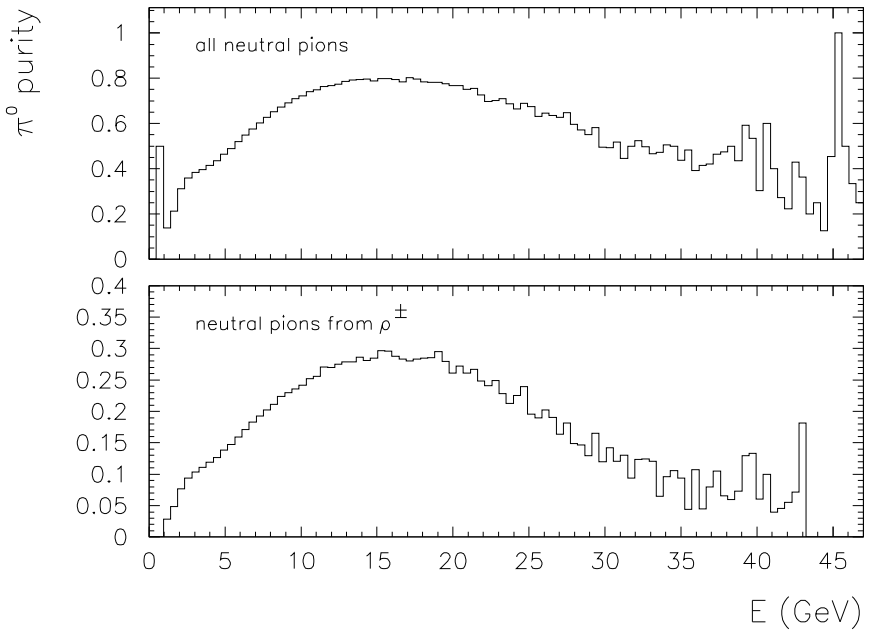

Figure 6.10: *Purity of reconstructed neutral pions as a function of energy for all pions and pions from the $\rho^{\pm}$ meson.*

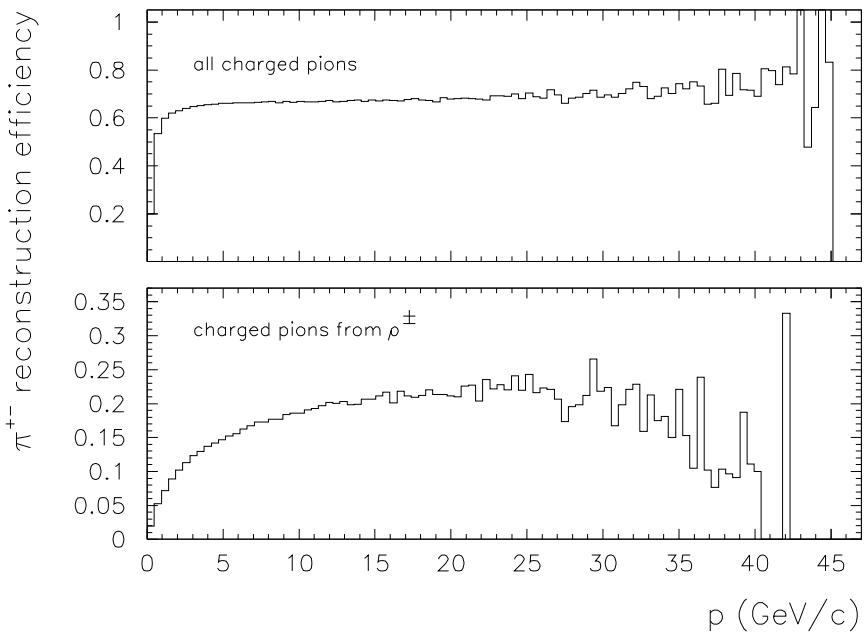

Figure 6.11: *Charged pion selection efficiencies.*

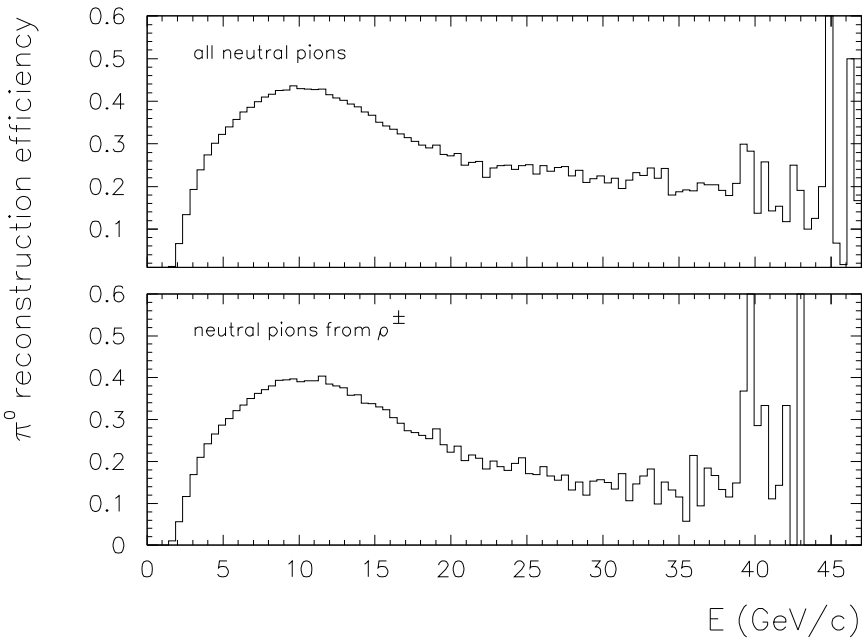

Figure 6.12: *Neutral pion selection efficiencies.*

6.4.4 Momentum and Energy Resolution

The momentum resolution, σ_p, for charged particles, is measured from the Monte Carlo and defined as the 'half width at half maximum' for the distribution p_{rec}/p_{tru}. The residual, δ_p , is defined as the displacement of the peak of the distributions from one. The results are shown in Figure 6.13. Resolution reduces at high momentum because the tracks become very straight, and at low momentum due to scattering of the particle with the gas in the TPC.

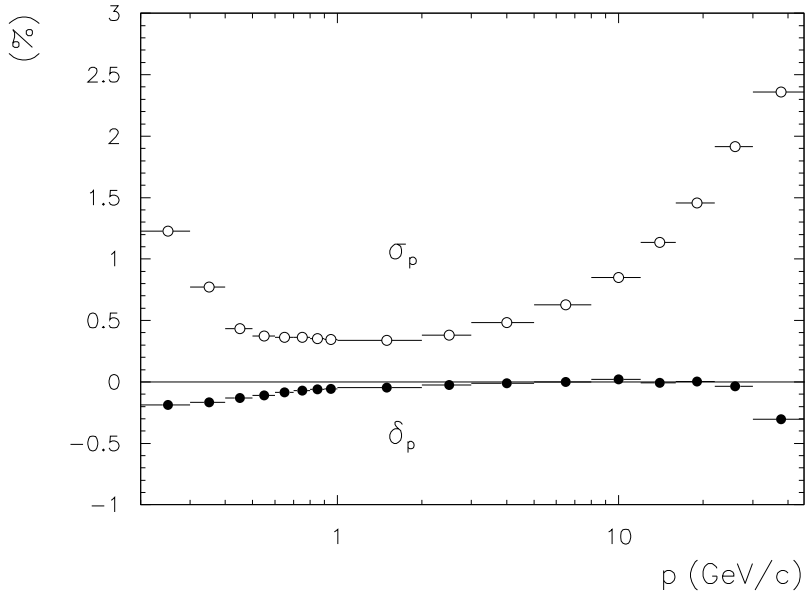

Figure 6.13: *Measured momentum resolution, σ_p, and residuals, δ_p, as a function of momentum for all reconstructed charged particles.*

Similarly, the energy resolution, σ_E, and the residual, δ_E, can be inferred from the distribution of E_{rec}/E_{tru} for π^0s. An example distribution before and after refitting is shown in Figure 6.14. The distribution before kinematic fit is wider and has larger residual. The plots for σ_E and δ_E as a function of π^0 energy are shown in 6.15. From these figures, improvement in the energy resolution and residuals, due to the mass constraint, are clearly seen.

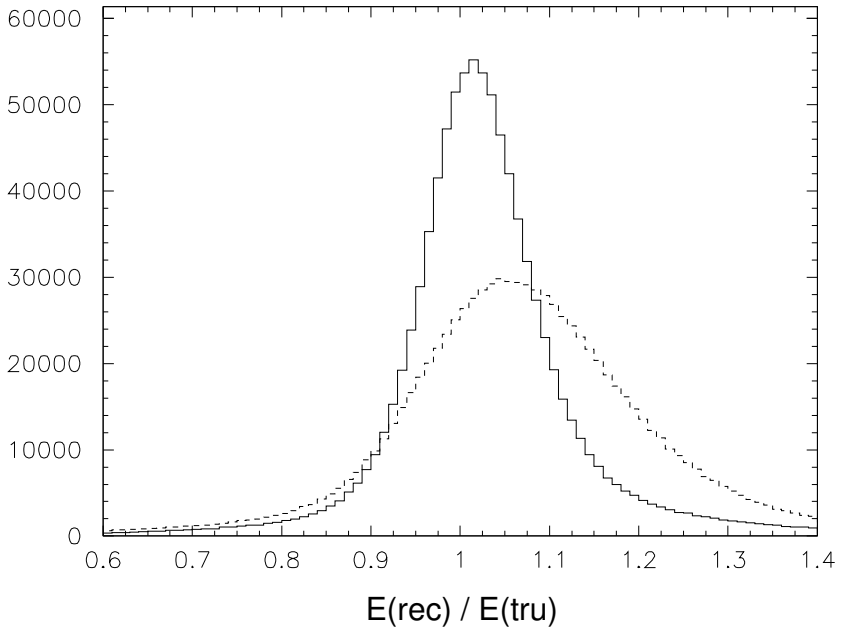

Figure 6.14: *An example of π^0 E_{rec}/E_{tru} distribution, before (dashed line) and after (solid line) the kinematic fit.*

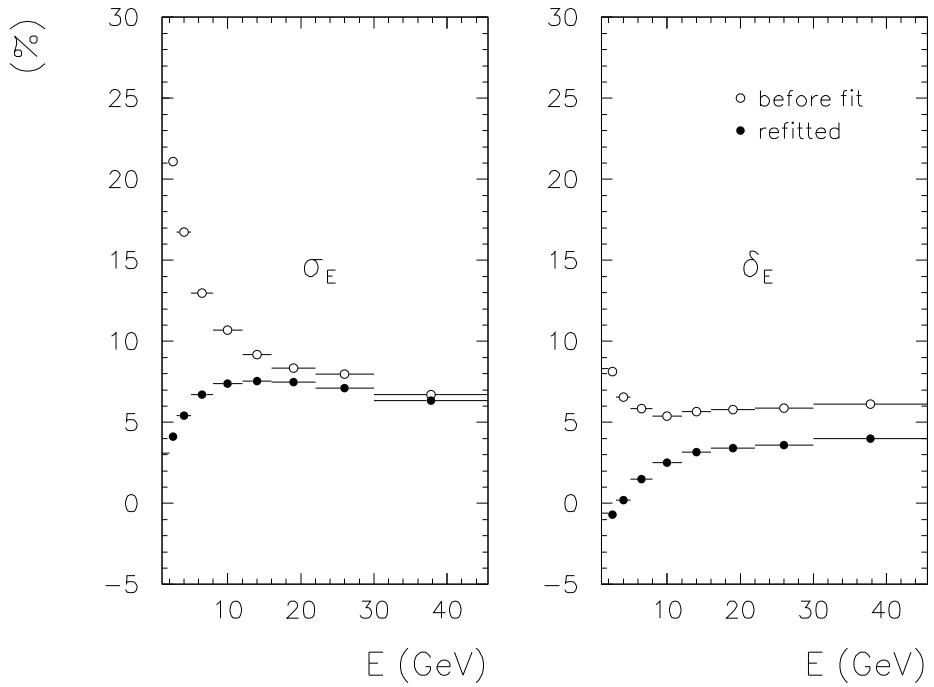

Figure 6.15: *Energy resolution, σ_E, and residuals, δ_E, as a function of energy for all reconstructed π^0s. The 'refitted' values (full circles) are results for π^0s after a mass constraint has been applied.*

CHAPTER 7

π^0 CALIBRATION

7.1 Introduction

π^0 candidates are built by combining pairs of photons. Selecting π^0s from a mass window around the reconstructed π^0 peak provides an initial rejection of most of the combinatorial background. To define a selection mass window, the signal peak and width needs to be defined. These parameters are seen to vary with π^0 energy and topology, therefore, a detailed calibration study has been performed for this analysis.

Figure 7.1 shows that the position of the peak and width change with increasing π^0 energy. The running of the peak position is due to detector effects [39]. The change in the width can be explained by a simple expression. Theoretically, the width of the signal, σ_M, varies with pion energy as follows[1]

$$\frac{\sigma_M}{M} = \frac{1}{2}\left[\frac{\sigma_{E_1}}{E_1} \oplus \frac{\sigma_{E_2}}{E_2} \oplus \frac{\sigma_{\theta_{12}}}{\tan(\theta_{12}/2)}\right] \tag{7.1}$$

where σ_{E_1} and σ_{E_2} are the energy resolution of the photons whose energies are E_1 and E_2, $\sigma_{\theta_{12}}$ is the spatial resolution of the calorimeter for the measured angular separation, θ_{12}, of the two photons. However, there are additional detector effects and so this formulation is only approximate.

The peak position and width depends not only on the energy but also topology due to clusterisation effects. Details of the mass window calibration are given next.

7.2 Calibration

Using Monte Carlo, we can flag the true π^0 signal and plot its mass spectra in energy intervals, E, and for different topologies, T. Studying the π^0 signal

[1] The derivation can be found in Appendix A.

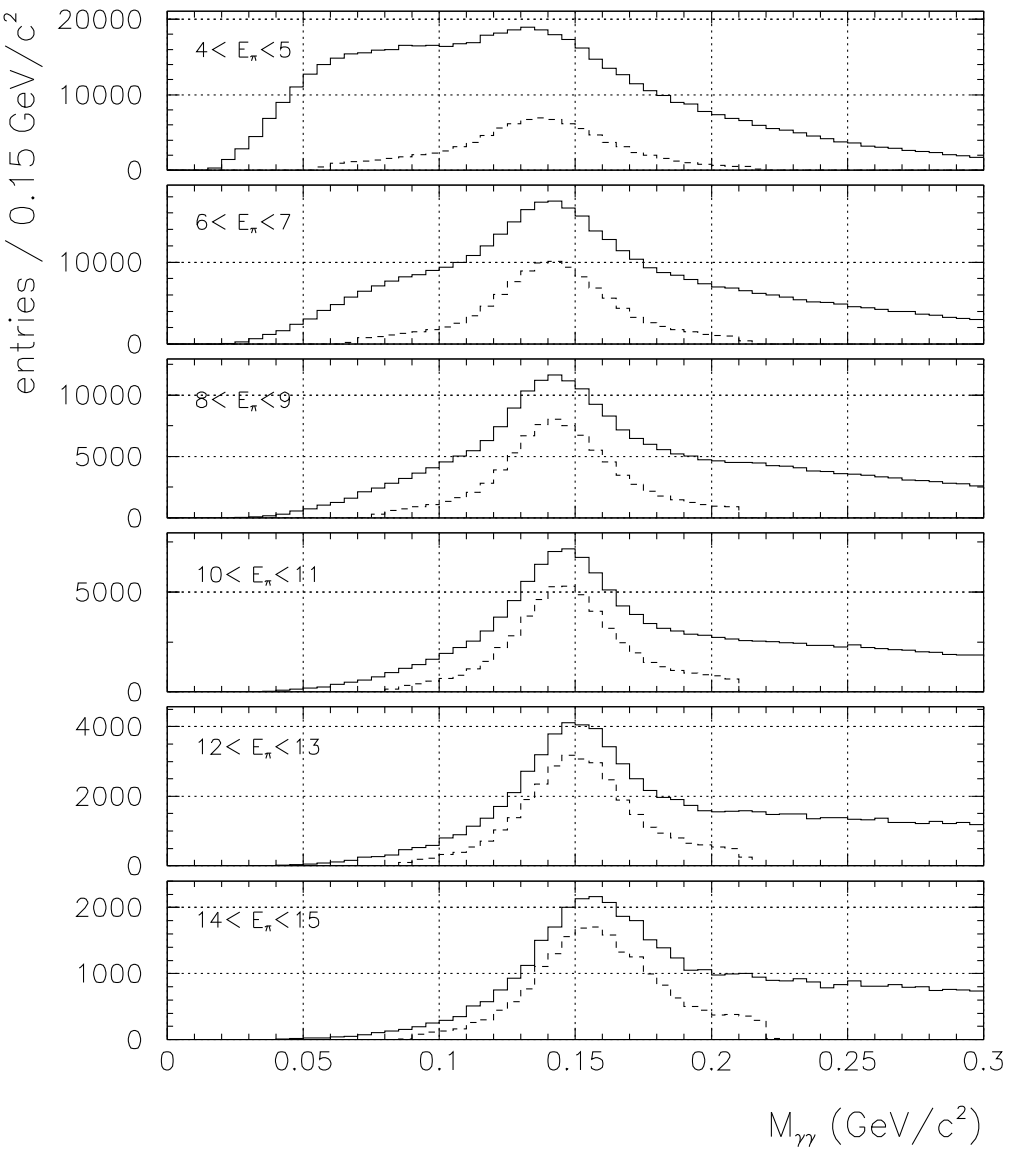

Figure 7.1: *Example π^0 peaks for reconstructed mass spectra (solid line) and Monte Carlo matched signal (dashed line): With increasing π^0 energy (from top plot to bottom plot), the position of the peak is seen to increase.*

peak position, m, and width, σ, we can calibrate (i.e. parametrise) two functions:

$$m(E,T) \text{ and } \sigma(E,T)$$

Figure 7.2 is an example of a Monte Carlo matched π^0 signal used for generating calibration fitting data.

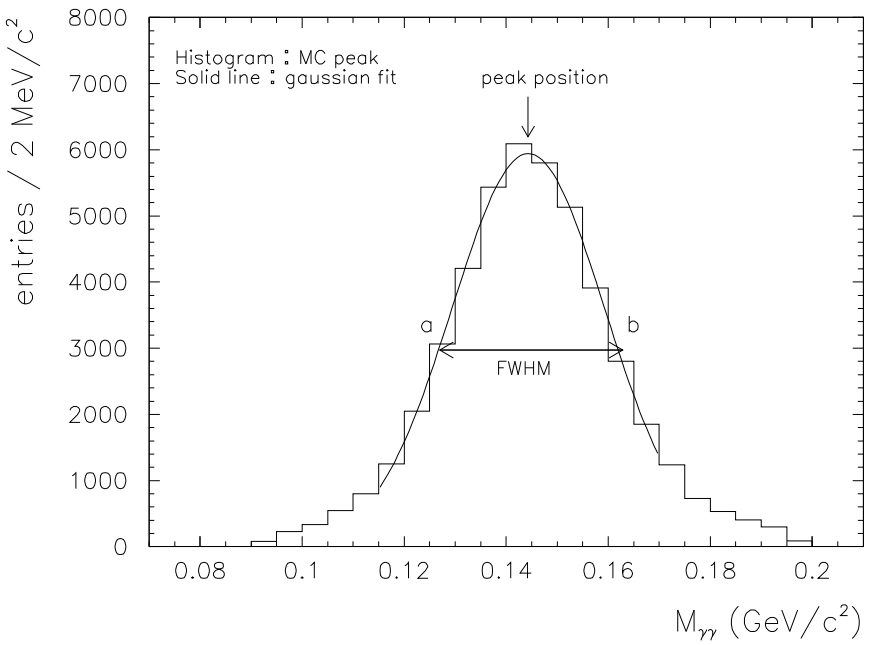

Figure 7.2: *Example of a Monte Carlo matched π^0 signal fitted with a Gaussian curve, used for generating calibration data.*

The calibration procedure is as follows:

1. The mass spectra is plotted for the matched π^0 signal for each topology in 1 GeV energy intervals.

2. The peak (signal) is fitted with a Gaussian from which the positions a and b, taken at half height, are measured.

3. The half width at half maximum (HWHM) $\sigma = (b-a)/2$, and the center of the mass window, $m = (b+a)/2$ are evaluated.

The results for all energy intervals are presented in Figures 7.3 and 7.4. A 4^{th} order polynomial fit function is selected for topology 1 and 2, and 3^{rd} order for topology 3 and 4, to parameterise the points. The functions have the general form:

$$\begin{aligned} P_4(E,T) &= a_0 + a_1E + a_2E^2 + a_3E^3 + a_4E^4 \quad (\text{for } T = 1,2) \\ P_3(E,T) &= a_0 + a_1E + a_2E^2 + a_3E^3 \quad (\text{for } T = 3,4) \end{aligned} \tag{7.2}$$

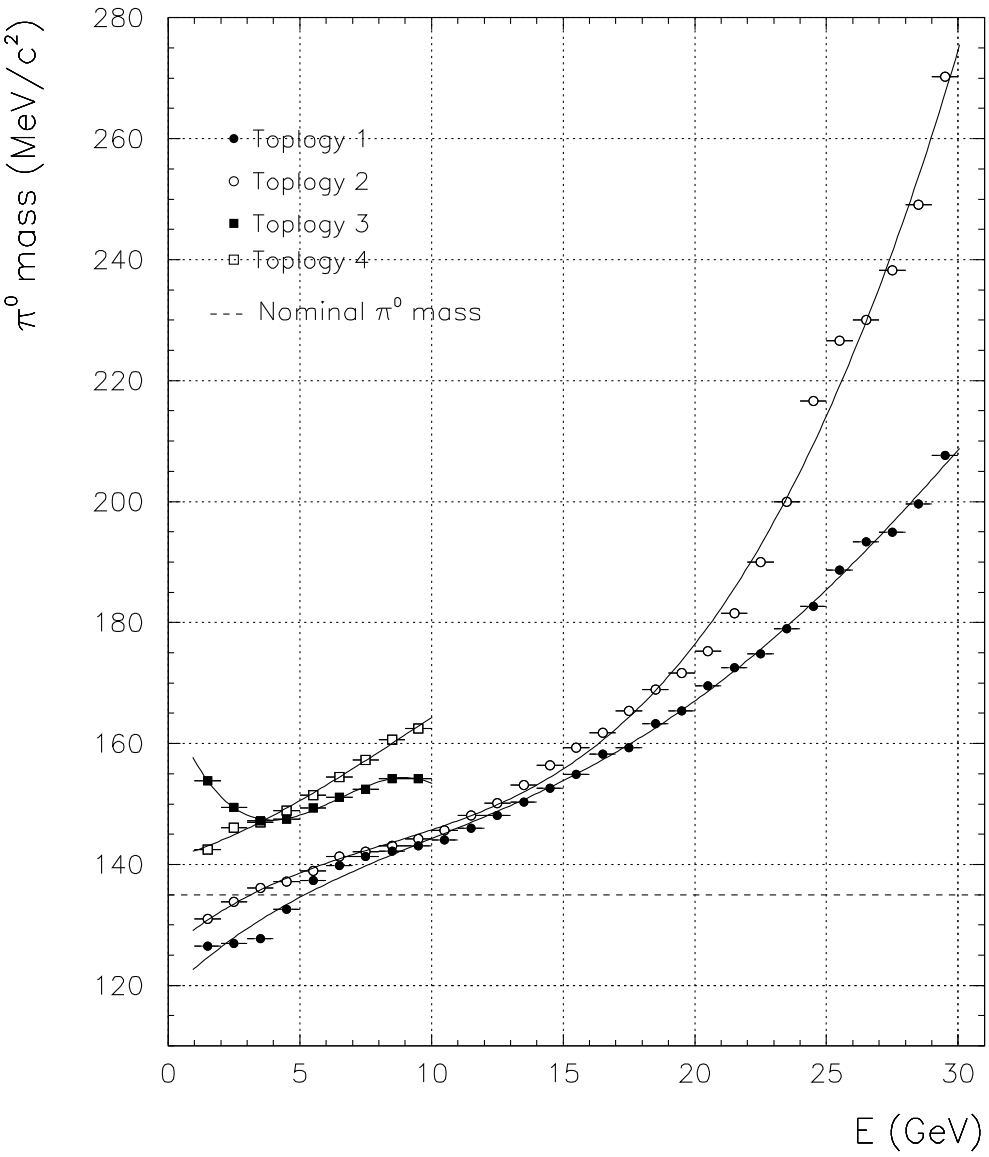

Figure 7.3: π^0 *mass vs energy for each topology and corresponding calibration functions.*

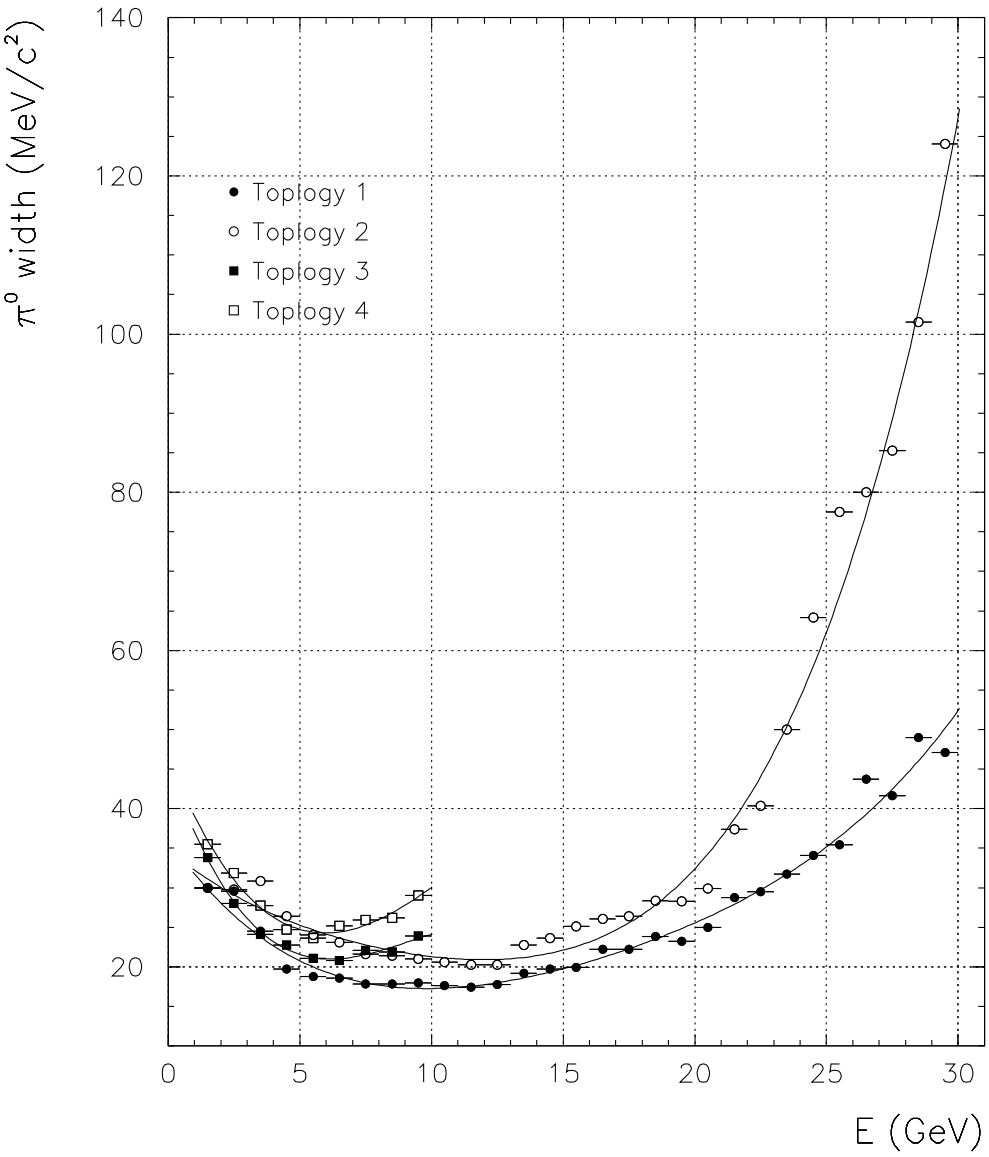

Figure 7.4: π^0 *width vs energy for each topology and corresponding calibration functions.*

The parameters (i.e. coefficients a_i of the polynomials) are determined by the least-square fitting method. The results are given in Table 7.1:

Table 7.1: *Results for the mass and width parameters obtained from the polynomial regression in the π^0 calibration.*

Mass parameters					
Toplogy	a_0	a_1	a_2	a_3	a_4
1	118.86	4.2403	-0.2767	0.0121	-0.00014
2	125.81	3.7536	-0.3050	0.0136	-0.00006
3	166.76	-11.539	2.1059	-0.1086	-
4	140.87	1.2325	0.1704	-0.0059	-
Width parameters					
Toplogy	a_0	a_1	a_2	a_3	a_4
1	36.203	-4.8385	0.4166	-0.01438	0.00021
2	34.801	-2.7759	0.2247	-0.01183	0.00036
3	45.590	-9.6605	1.1898	-0.04386	-
4	46.614	-8.4634	0.9544	-0.02736	-

7.3 Corrections

Two corrections are required in calibration related to topologies and the use of calibration functions in the real data.

Correction 1

In Figure 7.3 and 7.4, low statistics for energies above 10 GeV make it difficult to calibrate the peak positions and width for topology 3 and 4. Therefore, for energies above 10 GeV the functions from topology 1 and 2 are used for topology 3 and 4 respectively with a +10 MeV/c^2 shift.

Correction 2

The parameters of Equations 7.2 are calculated just for the Monte Carlo signal. In the reconstruction level, when we look at the comparison of the peak position between Monte Carlo and real data, we see that there is a small difference, δ, being nearly constant for all energies, in the the peak positions. An example is shown in Figure 7.5.

In general, the difference is of the order of a few MeV/c^2 and it is also dependent on the topology. Figure 7.6 shows all mass differences for each topology. Note that the real data values are always less than Monte Carlo values. Different constant correction factors are selected for different topologies. The factors are

shown as dashed lines in Figure 7.7. Numerically they are:

For topology 1 : 3.80 MeV/c^2
For topology 2 : 2.46 MeV/c^2
For topology 3 : 6.91 MeV/c^2
For topology 4 : 3.46 MeV/c^2

When we use real data we subtract these values from the mass functions obtained from Monte Carlo studies. However, the widths are assumed to be the same.

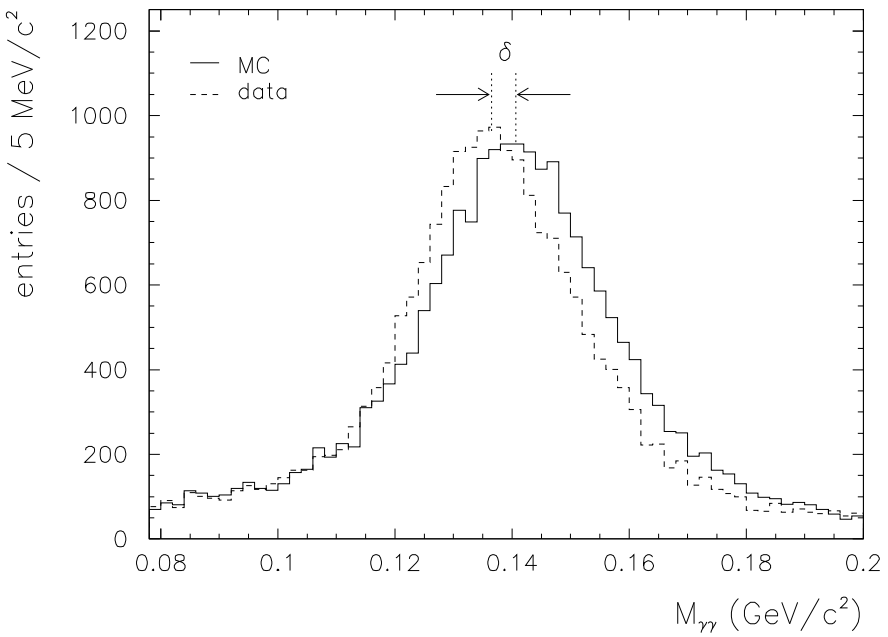

Figure 7.5: *An example of a mass difference, δ, between Monte Carlo and real data. It is required to make a small correction for real data with respect to the Monte Carlo.*

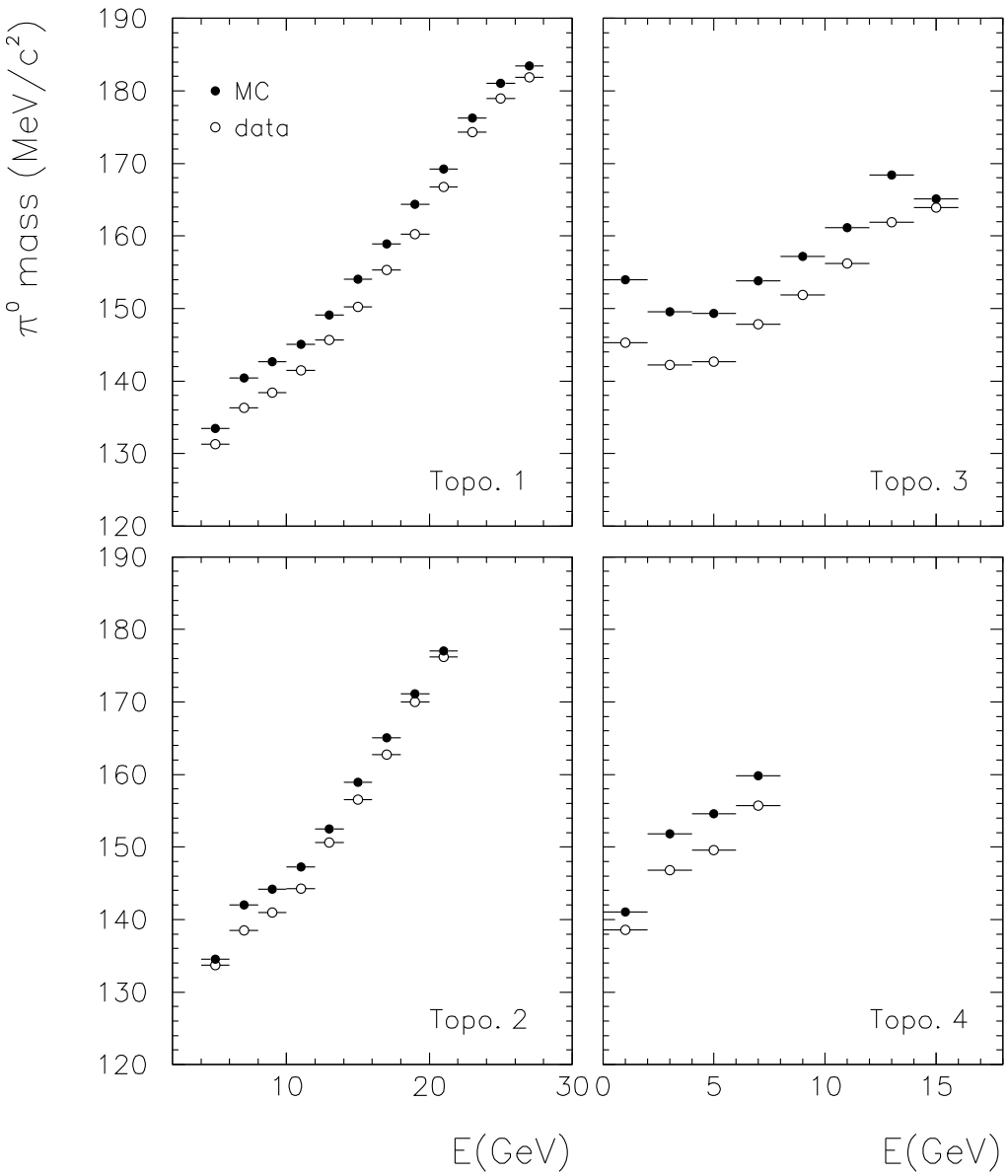

Figure 7.6: π^0 *peak mass vs energy for each topology. The peak mass in the real data is always less than that in the Monte Carlo by a few* MeV/c^2.

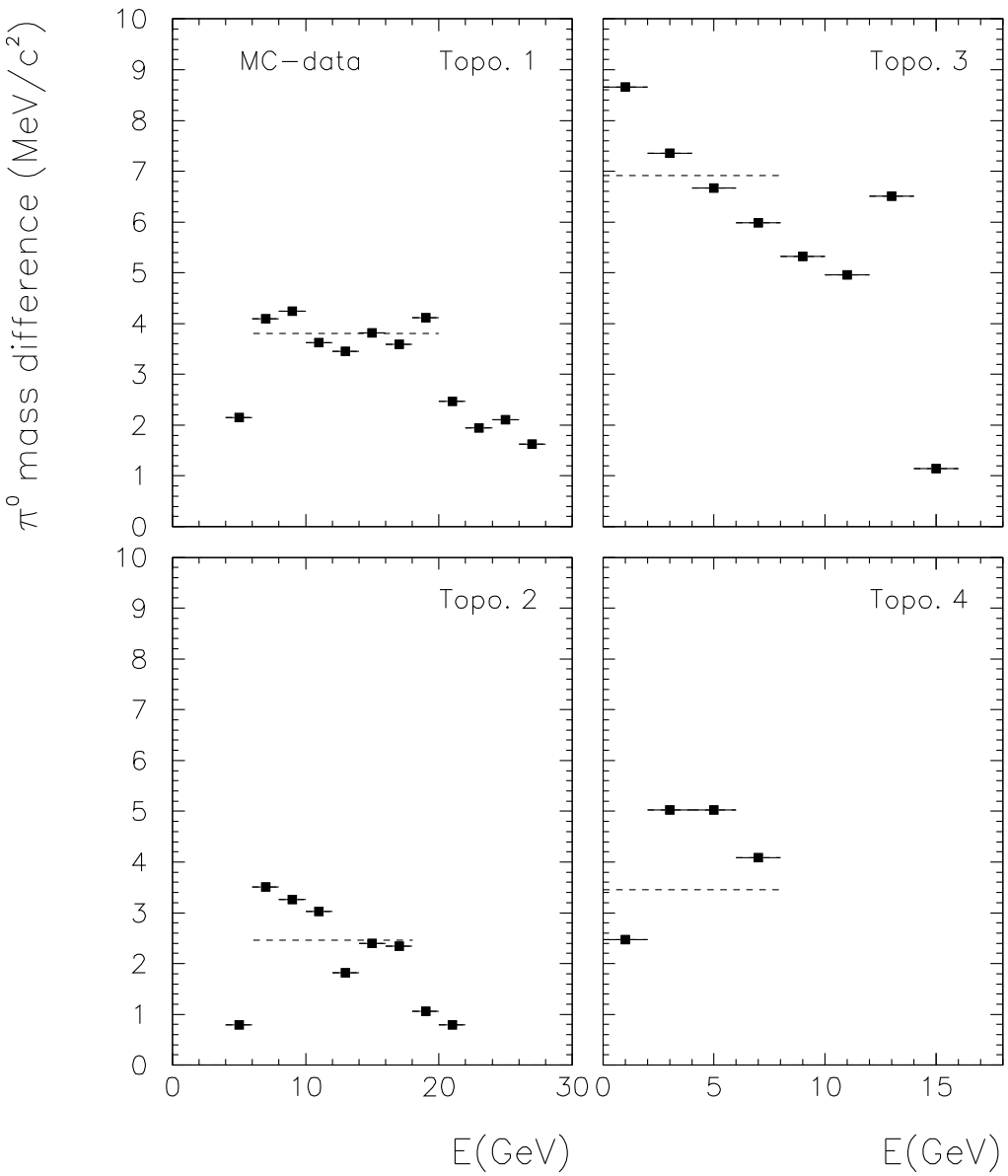

Figure 7.7: π^0 *peak mass vs energy difference between Monte Carlo and real data for each topology. The correction factors (shown as dashed line) are average values of the points in the selected regions.*

7.4 Calibration Performance

The selection algorithm is applied both to Monte Carlo and real data for each topology. The calibration functions appear to select properly the π^0 candidates around the peak positions for all energy intervals. Examples for a selected energy interval are shown in Figure 7.8.

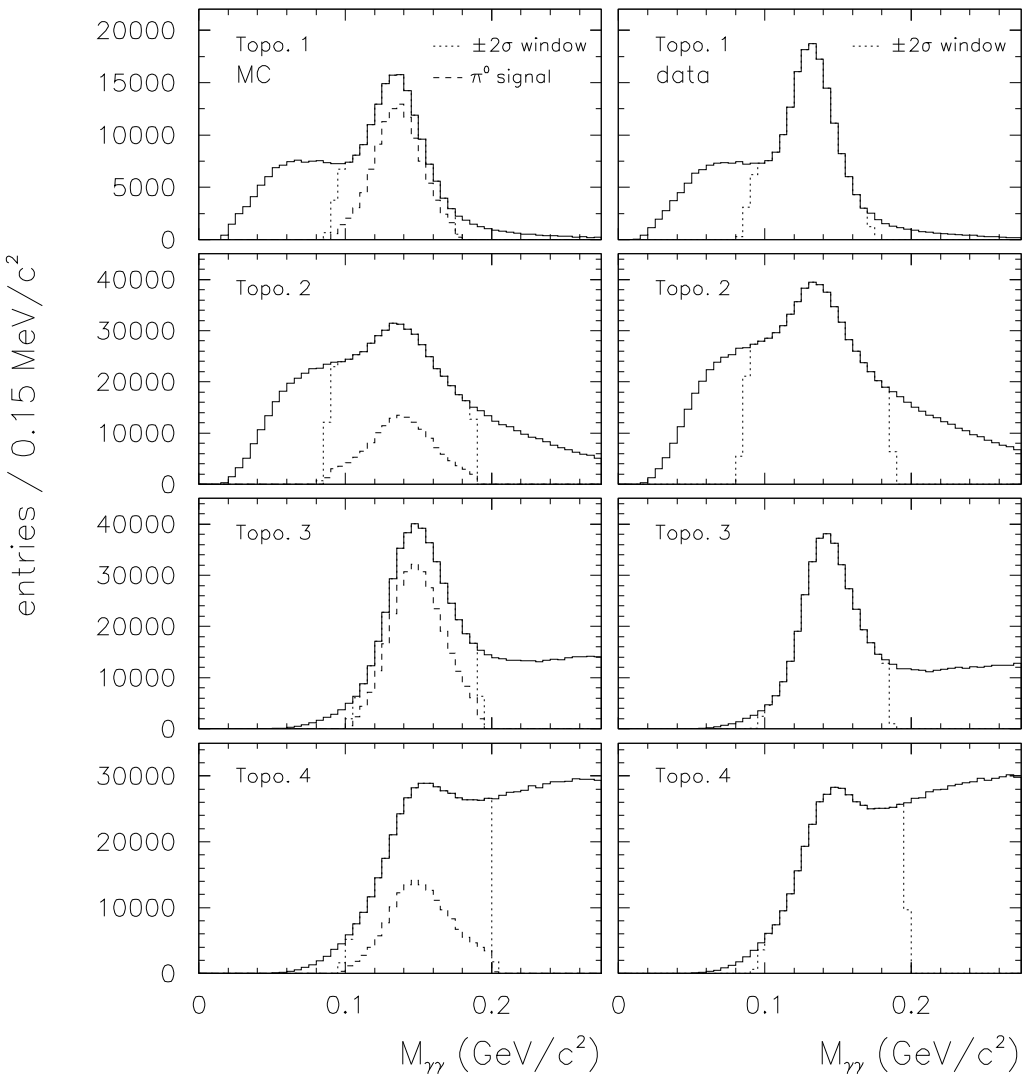

Figure 7.8: *An example to show the performance of the π^0 calibration for each topology. Two photon invariant mass spectra around the π^0 peak, for π^0 energy between 2 GeV $< E_{\pi^0} <$ 3 GeV, are plotted for reconstruction level (solid line), π^0 signal (dashed line) and $\pm 2\sigma$ mass window (dotted line). The plots in the left column are for Monte Carlo , and right column are for real data. These results indicate that the calibration functions give a correct selection of the π^0 peak.*

CHAPTER 8

THE RANKING METHOD

8.1 Introduction

The selection of π^0 mesons in the two photon decay mode in particle interactions can be a relatively simple task where candidates are selected from a mass window around the signal peaks. However, in environments where particle multiplicities are high, greater analysis and optimisation is required if one is to gain optimal selection efficiency and purity.

In this chapter, first, a statistical treatment of π^0 reconstruction is presented. Then, the standard method is introduced for the selection of π^0 candidates. Later, the π^0 estimators for distinguishing between background and signal are developed, and finally, the detailed study of a Ranking Method for increasing the purity of reconstructed π^0s is presented.

8.2 π^0 Reconstruction

Consider n photons that are taken (measured) from the ECAL. Assuming each photon originates from a π^0, we can form π^0 candidates by building photon pairs as follows:

```
PHOTONS  SELECTED PAIRS (combinations)
1        12  23  34  45 ... (n-1)n
2        13  24  35  .   .
3        14  25  .   .    .
4        15  .   .   .
5        .   .   .   4n
.        .   .   3n
.        .   2n
n        1n
```

The number of π^0 candidates obtained from n photons taken a pair at a time is:

$$C(n,2) = \frac{n!}{2!(n-2)!} = \frac{n(n-1)}{2} \tag{8.1}$$

Hence, $n(n-1)/2$ candidates form signal and background, $S+B$. But only $n/2$ of them are true forming S. From now on, the purity (or signal probability):

$$\mathcal{P} = \frac{S}{S+B} = \frac{n/2}{n(n-1)/2} = \frac{1}{n-1} \tag{8.2}$$

and signal-to-background ratio is:

$$\frac{S}{B} = \frac{n/2}{n(n-1)/2 - n/2} = \frac{1}{n-2} \tag{8.3}$$

The result indicates that the purity and S:B decreases approximately proportional to the number of pions in the event (e.g. for $n = 20$, $\mathcal{P} \approx 5\%$). The selection of neutral pions with a high purity and a high efficiency is important in the formation of $\rho^{\pm}$ mass spectra. The poor purity of low energy π^0s can be improved by removing some combinatorics: initially by selecting candidates from a mass window, and secondly by forming additional discriminators. This is discussed further in the following sections.

8.3 The Standard Method

In the standard method, π^0 candidates are directly selected from a mass window (around the π^0 peak) of the two-photon invariant mass spectra as illustrated in Figure 8.1.

The selection of π^0s with a high purity and efficiency is important. In this study, we define the purity ($\mathcal{P}$) and efficiency (ε) as follows:

$$\mathcal{P} = \frac{S}{S+B} \tag{8.4}$$

$$\varepsilon = \frac{S}{S_0} \tag{8.5}$$

Here, S is the number of selected signal, B is the number of background for the given mass window, and S_0 is the total number of signal within $\pm 6\sigma$ mass window, where σ, defined as half width at half maximum, represents the calibrated mass resolution.

The purity of the selected π^0s can be improved by tightening the mass window from, for example, $\pm 3\sigma$ to $\pm 2\sigma$ though with a reduction in efficiency. An optimal selection window, where both the purity and efficiency are maximised, can be determined. We define the optimisation condition such that the product $\varepsilon \times \mathcal{P}$ is maximum. This is equivalent to maximising the signal significance. Figure 8.2 shows the effect of varying the selection mass window between $\pm 1\sigma$ and $\pm 6\sigma$. The optimal width is about $\pm 2\sigma$ ($\pm 1.7\sigma$) where the product $\varepsilon \times \mathcal{P}$ is high; in some analyses a wide mass window of $\pm 3\sigma$ is preferred to avoid systematic uncertainties in the efficiency corrections.

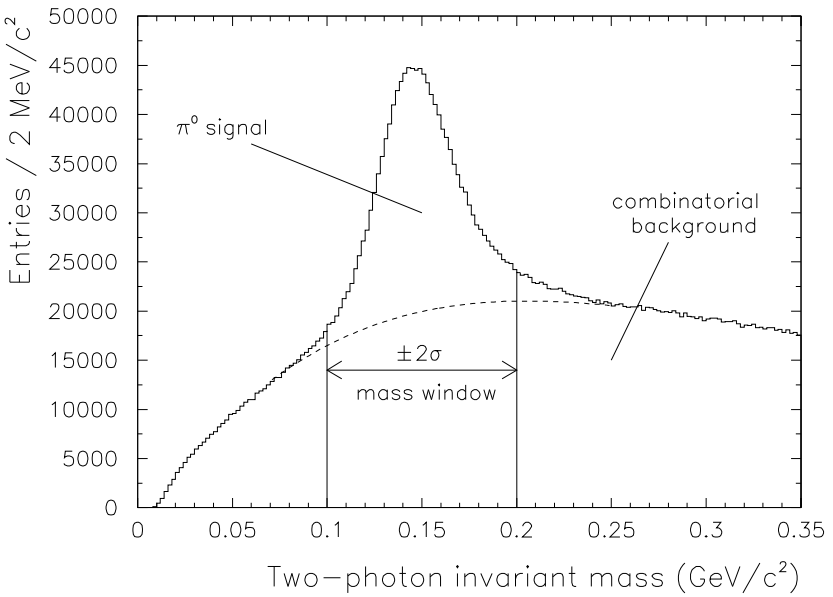

Figure 8.1: *A mass window around the pion peak can be selected to remove most of the background. The width of the window can be described in terms of a number of σs representing the mass resolution. A width of $\pm 2\sigma$ or $\pm 3\sigma$ is common selecting true pions while rejecting most of the background.*

8.4 π^0 Estimators

Initial mass window selection (e.g. $\pm 3\sigma$), forms the starting point to study a method for improving the signal significance. An estimator, obtained from kinematic properties of the π^0s, can be used to discriminate between π^0 signal and background. Three basic estimators are built from the following distributions:

- chi-square (χ^2) values from the mass constraint (Equation B.2)
- photon pair opening angles, θ_{12}
- 2D scatter distribution of χ^2 vs θ_{12}

The one-dimensional distributions are given in Figure 8.3a and Figure 8.3b. True π^0s tend to have smaller χ^2 values and smaller opening angles than false π^0s. The estimators, based on these distributions, can therefore be used to attempt to distinguish between correct combinations (signal) and wrong combinations (background) of photon pairs.

Combining the estimators into a two-dimensional distribution increases the potential for discrimination, this distribution is shown in Figure 8.3c. Various forms for a discriminating function have been investigated, including rectangular and triangular shapes and ellipses. For the data used in this study, an ellipse is found to perform the best. The solid curve shown in Figure 8.3c, and has the form:

$$(\chi^2/A)^2 + (\theta_{12}/B)^2 = 1 \tag{8.6}$$

The discriminating function (i.e. the parameters A and B in Equation 8.6) is optimised such that the product of efficiency and purity is maximum for the data. This function can be used directly in the selection of π^0 candidates. However, greater performance can be gained by using this function as an estimator in a Ranking method detailed in the next section.

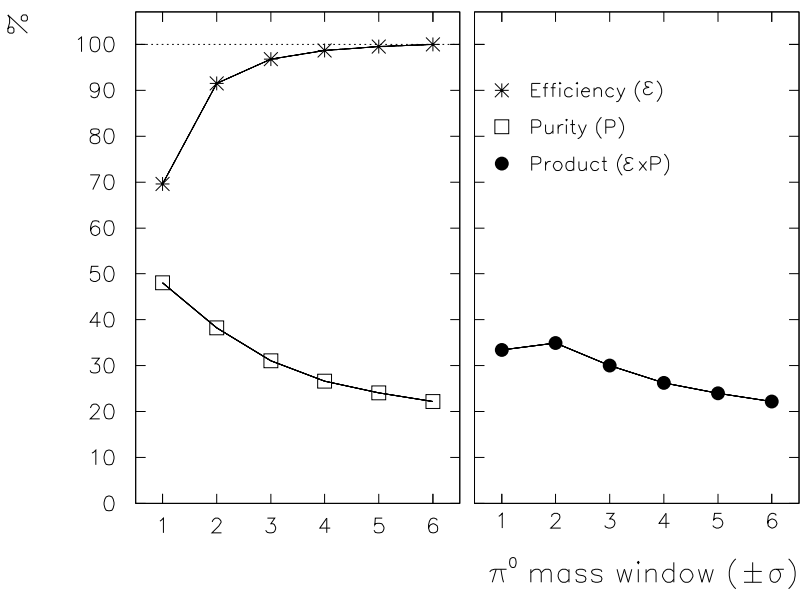

Figure 8.2: *Effect of varying the mass window on the π^0 selection efficiency, purity, and their product. The π^0 mass window width is varied from $\pm1\sigma$ to $\pm6\sigma$. The selection efficiency of the π^0s are calculated with respect to $\pm6\sigma$ window since 100% of the π^0 signal is inside in this window. Improvement in the purity can be gained by tightening the mass window though with a reduction in efficiency. Statistically, an optimal selection mass window can be found by maximising the product $\varepsilon \times \mathcal{P}$. The optimum value is around $\pm2\sigma$.*

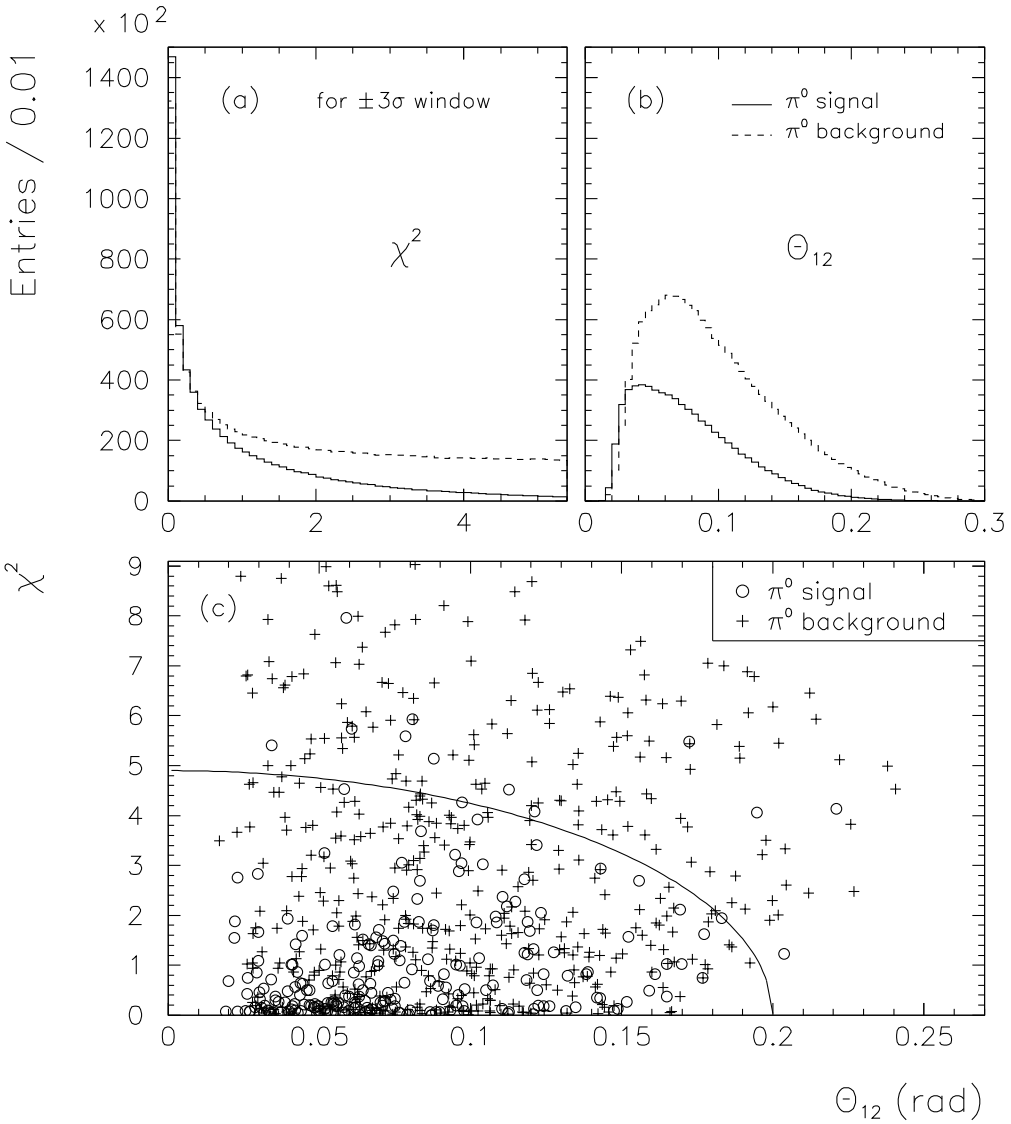

Figure 8.3: *Ranking estimators for π^0. (a) The distributions of χ^2 (from a mass constraint), (b) photon pair opening angle, θ_{12}. True pions are represented by solid lines, incorrect combinations of photons yield false pions (combinatorial background) are represented by dashed lines. (c) scatter plot of χ^2 versus θ_{12}, signals are represented by circles, backgrounds by crosses. The combinatorial background tends to have larger χ^2 and θ_{12} values than true pions, this feature is used to discriminate between pions and background.*

8.5 Ranking

After the initial mass window selection, additional improvement is achieved by applying the estimator indirectly with a 'Ranking' method. The algorithm is as follows:

1. Pion estimator values are calculated for each pion candidate in an event.
2. Pions are then ranked in order of their estimator with the smallest estimator values (most likely to be true pions) nearer the top of the list.
3. A scan is then made through the list for pairs of pions which share photons. When such a pair exists, one or both of the candidates must be false; the candidate with the largest estimator value is removed.

The Ranking method involves three main steps; first parameters for the Ranking estimator are found, then the Ranking estimator is optimised, and finally the Ranking and selection procedure is applied. More information about the Ranking method can be found in [40].

An example of the Ranking method is shown below for an event where five pions candidates, selected from a $\pm 3\sigma$ mass window, are reconstructed from the photons of four pions.

Selected candidates *before* Ranking				Selected candidates *after* Ranking			
	Pion	Photon	Truth		Pion	Photon	Truth
#	est.	1 2	info.	#	est.	1 2	info.
=	====	== ==	=====	=	====	== ==	=====
A	0.05	A1 A2	TRUE	A	0.05	A1 A2	TRUE
B	0.14	B1 B2	TRUE	B	0.14	B1 B2	TRUE
C	0.24	C1 C2	TRUE	C	0.24	C1 C2	TRUE
X	0.29	A1 B2	FALSE	D	0.33	D1 D2	TRUE
D	0.33	D1 D2	TRUE				
$P = S/(S+B) = 4/(4+1) = 0.80$				$P = S/(S+B) = 4/(4+0) = 1.00$			

The photons are labeled `A1`, `A2`, `B1`, `B2`, `C1`, `C2` and `D1`, `D2` representing the photons from the four true pions `A`, `B`, `C`, and `D`. The fifth false pion candidate is reconstructed from photons `A1` and `B2`. As the mass of this false pion is in the region of the pion mass signal and its pion estimator is small (less than 1.0) this candidate is not rejected by the standard method; it is however rejected in the Ranking method where in this example pion `A` removes pion `X` from the list as they both share photon `A1`. Note that you can compare the purities given at the

end of each table. In this example the Ranking algorithm has removed the false pion with no loss of true pions. This ideal behavior is not always the case as frequently true pions are removed and/or some false pions are preserved. This is illustrated in the next example containing 11 π^0 candidates.

Selected candidates *before* Ranking				Selected candidates *after* Ranking			
	Pion	Photon	Truth		Pion	Photon	Truth
#	est.	1 2	info.	#	est.	1 2	info.
=	====	== ==	=====	=	====	== ==	=====
A	0.01	A1 A2	TRUE	A	0.01	A1 A2	TRUE
	0.02	X C2	FALSE		0.02	X C2	FALSE
B	0.03	B1 B2	TRUE	B	0.03	B1 B2	TRUE
C	0.05	C1 C2	TRUE	D	0.46	D1 D2	TRUE
	0.08	Y C2	FALSE		0.55	C1 F2	FALSE
	0.10	X Y	FALSE	E	0.58	E1 E2	TRUE
D	0.46	D1 D2	TRUE				
	0.55	C1 F1	FALSE				
	0.55	C1 F2	FALSE				
E	0.58	E1 E2	TRUE				
F	0.64	F1 F2	TRUE				
	0.81	E2 F1	FALSE				
	0.84	Z E2	FALSE				
$\mathcal{P} = S/(S+B) = 6/(6+7) =$ **0.46**				$\mathcal{P} = S/(S+B) = 4/(4+2) =$ **0.67**			

Here, only four out of the six true pions are selected, and, two out of the seven false candidates are not rejected. The list contains six photon pairs from six pions (`A` to `F`) plus three solitary photons (`X`, `Y`, and `Z`) with their partner photons removed by a 1 GeV energy cut. Pion `C` is removed by the combination of photons `X` and `C2` which results, by chance, in a pion candidate with a smaller estimator value. Pion `F` having a relatively large estimator value is removed by the combination of photons `C1` and `F1` (this combination surviving due to the earlier removal of pion `C`).

On average however, Ranking greatly improves the selection purity relative to the standard method with some additional reduction in selection efficiency. For this example event, even with a loss of two signals, it is clear to see that the purity gain is about 20% after Ranking. More detailed comparisons of the standard and Ranking method are presented in the next section.

8.6 Performance of the Ranking Method

To investigate the performance of the Ranking method, the width of the mass window, and pion energy, are varied. The Ranking selection performance is compared to the performance of the standard method where the π^0 discrimination is based only on a mass window cut. Performance is measured in terms of the product efficiency ε and purity $\mathcal{P}$. Results of this study are discussed in detail below.

8.6.1 π^0 Estimator Effect

As described in Section 8.4, the χ^2 and θ_{12} can be used as discriminators. Figure 8.4 shows a comparison of these two discriminators used as Ranking estimators. Each estimator improves on the standard method. But the estimator obtained from the 2D distribution of χ^2 vs θ_{12} has the best performance for each value of the mass window, therefore, this estimator is used in our analysis. Note that, the 2D-estimator function, Equation 8.6, is re-optimised for the Ranking method, the optimal function is found to be:

$$R = (0.04\ \chi^2)^2 + \theta_{12}^2 \tag{8.7}$$

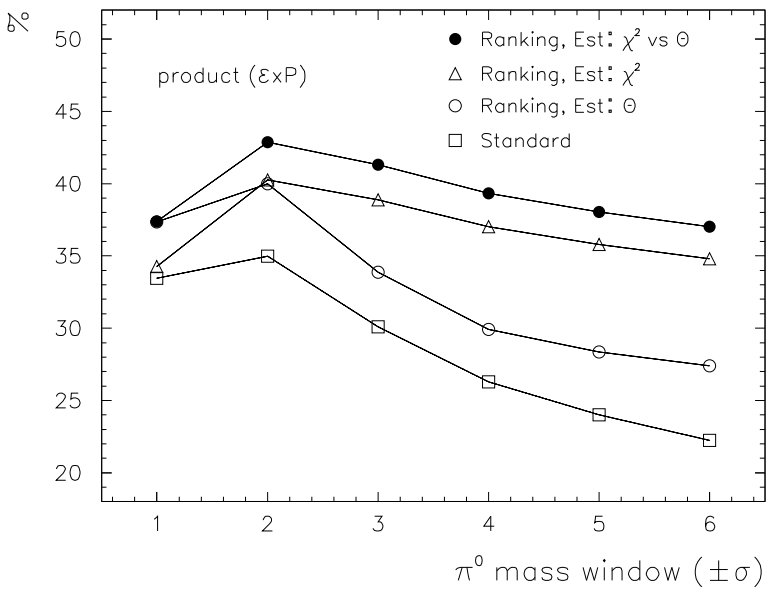

Figure 8.4: *Comparison of the product $\varepsilon \times \mathcal{P}$ values for three π^0 estimators and the standard method. Here the mass window width is varied. All of the Ranking estimators improve the product $\varepsilon \times \mathcal{P}$ values relative to the standard method.*

8.6.2 π^0 Energy

Figure 8.5 shows the response of the two selection methods with respect to pion energy. Purity and product $\varepsilon \times \mathcal{P}$ is improved with a small reduction in efficiency, when applying Ranking. Improvements are seen throughout the whole energy range, with the greatest improvements between 3 and 12 GeV.

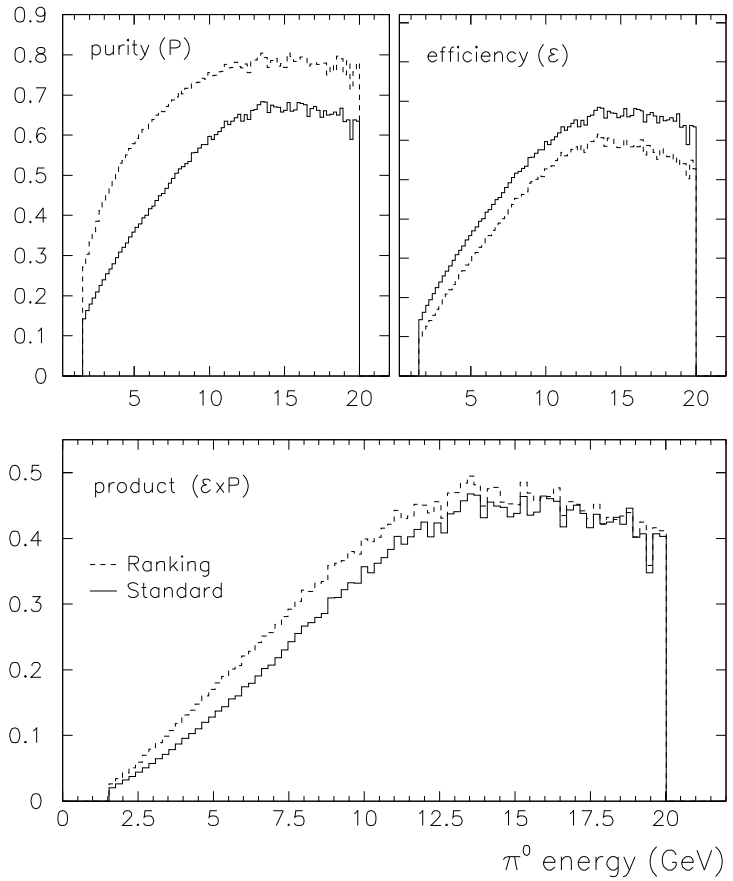

Figure 8.5: *Energy distribution of pions before and after Ranking. Ranking yields improvement in pion purity and product $\varepsilon \times \mathcal{P}$ with a small reduction in efficiency.*

8.6.3 Mass Window

Figure 8.6 shows the effect of varying the selection mass window between $\pm 1\sigma$ and $\pm 6\sigma$. Reducing the width of the window (cutting tighter into the signal peak) increases the signal-to-background ratio thereby increasing purity though at the expense of efficiency which falls rapidly for cuts below $\pm 2\sigma$. For both methods, the optimal width is typically around $\pm 2\sigma$ where $\varepsilon \times \mathcal{P}$ is maximum. While the Ranking method gives less efficiency, the improvement in purity results in a larger $\varepsilon \times \mathcal{P}$ value and therefore large signal significance. The fall in the

$\varepsilon \times \mathcal{P}$ value with increasing mass window is not sharp. This is an important feature allowing one to chose a wider mass window (e.g. $\pm 3\sigma$ or $\pm 4\sigma$) without a significant loss in $\varepsilon \times \mathcal{P}$, thus avoiding systematic errors relating to the selection of the π^0 peak.

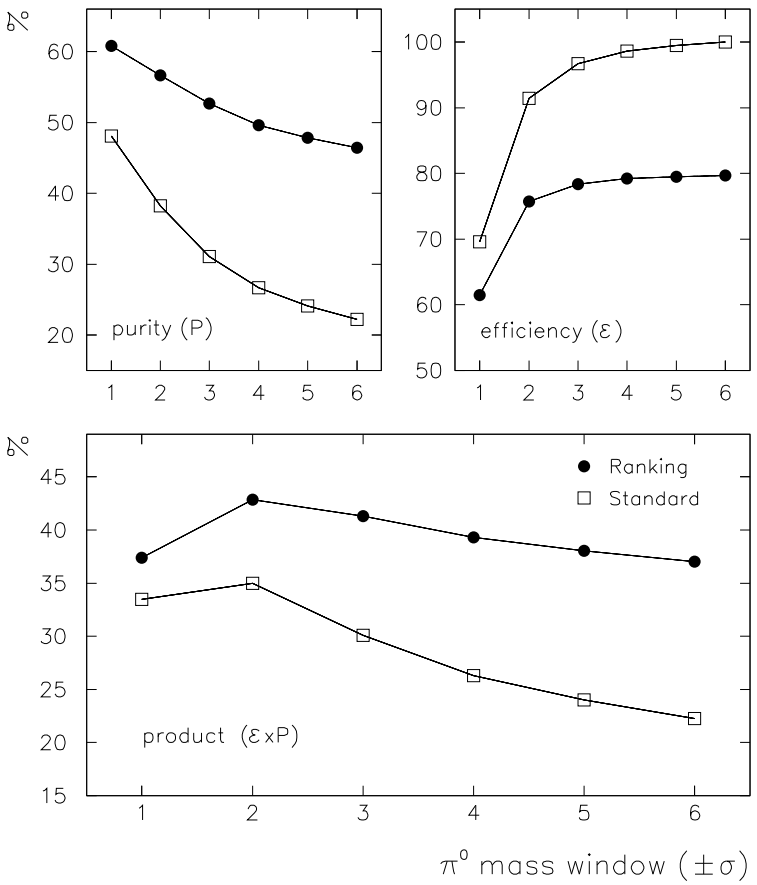

Figure 8.6: *Comparison of purity, efficiency, and product ($\varepsilon \times \mathcal{P}$) values for two pion selection methods as a function of mass window width. The improvement in the pion purity is about 21% with a loss in efficiency of 20% in the Ranking method. But, the $\varepsilon \times \mathcal{P}$ values are much better than the standard method. So, the Ranking method allows us to select a wider mass window.*

8.6.4 Invariant Mass

It is interesting to see shape of the two-photon invariant mass spectra before and after Ranking, Figure 8.7. Most of the background is killed by the Ranking method. So, the mass spectra within $\pm 3\sigma$ π^0 mass window contains a lot of signal and the Ranking mass spectra looks similar to the a signal peak.

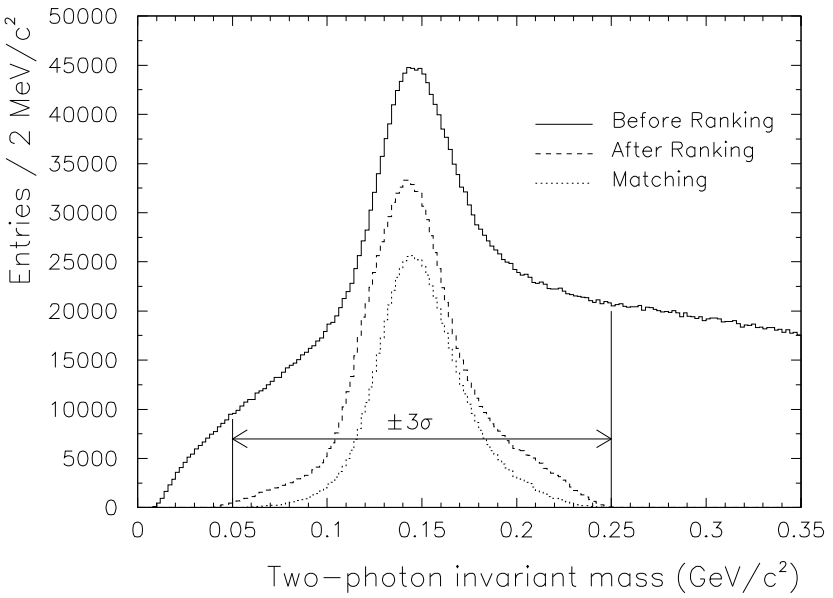

Figure 8.7: *Two-photon invariant mass spectra before and after Ranking. The Ranking method is applied to $\pm 3\sigma$ mass window. The Ranking method kills 66% of background and 18% of signal.*

8.7 Example Applications

The performance of the Ranking method for the selection of π^0 is demonstrated in two examples applied to the real data.

Example 1

One of the decay modes of the η and ω is three pions: $\eta \to \pi^+\pi^-\pi^0$, $\omega \to \pi^+\pi^-\pi^0$. Combinatorial background is very large in the three-pion mass spectra making extraction of an accurate value for the signal difficult. To attempt to reduce this background, the Ranking method is employed to improve the purity of π^0 selection. Figure 8.8 shows an example of one such mass spectra before and after Ranking. The Ranking method yields significant improvement in π^0 purity. After Ranking, η and ω signals seems to be clearer, fitting errors are reduced both statistically (less background) and systematically (more stable fits).

Example 2

The $\rho^\pm$ meson decays into two pions: $\rho^\pm \to \pi^0\pi^\pm$. The same procedure as in Example 1 is applied. Results are shown in Figure 8.9. The $\rho^\pm$ signal is clearer after Ranking.

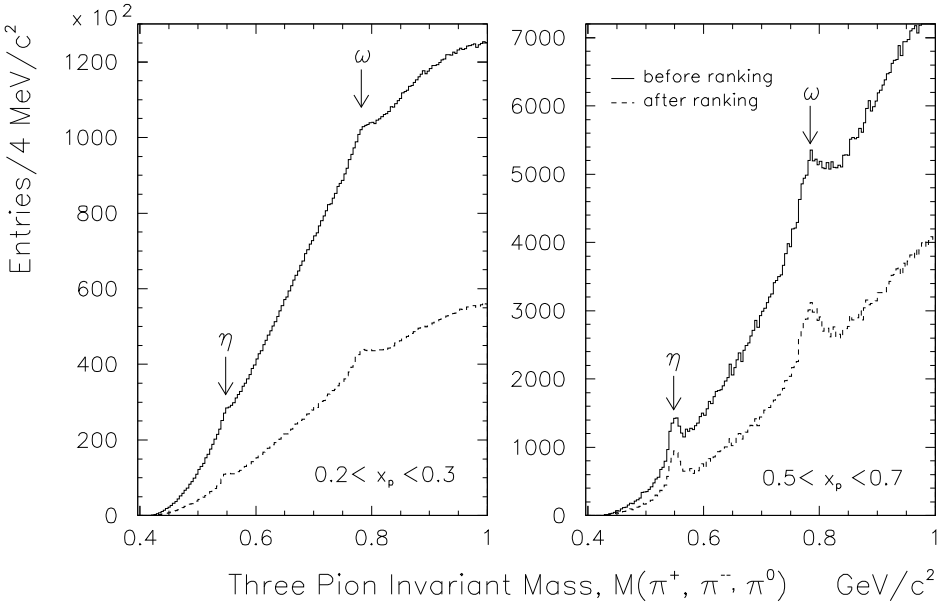

Figure 8.8: *Three-pion invariant mass spectra, for two different momentum intervals, $x_p = p_{particle}/p_{beam}$, before, and after, applying Ranking to improve the purity of π^0. All charged particles are assumed to be $\pi^{\pm}$ and π^0 candidates are selected from $\pm 3\sigma$ mass window. η and ω signals are seen around 548* MeV/c^2 *and 780* MeV/c^2*, respectively. After Ranking, the signals appear clearer. When fitting mass spectra whose background is very large Ranking both improves the statistical significance of the fit and the fit stability.*

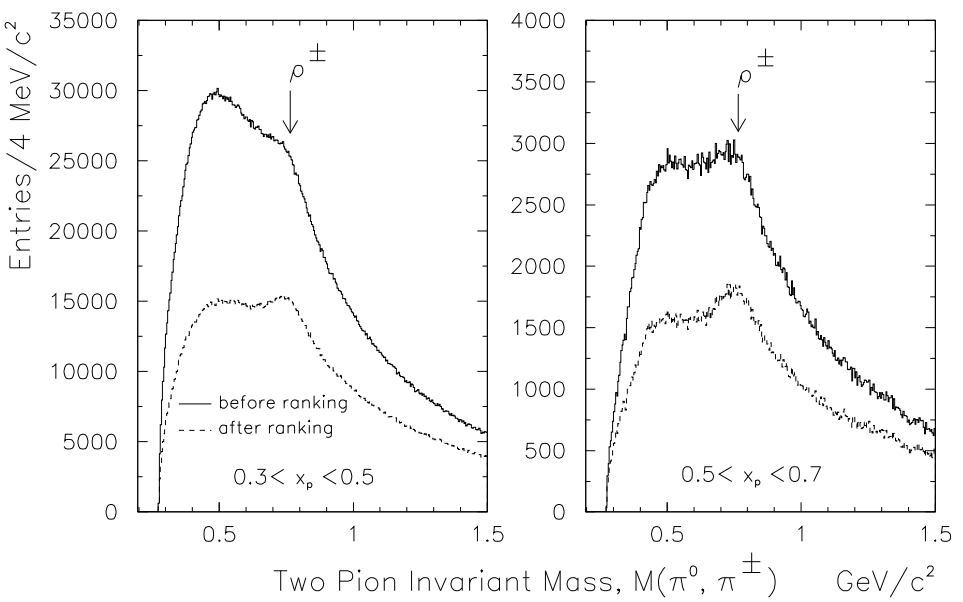

Figure 8.9: *Two-pion invariant mass spectra, before, and after Ranking. $\rho^{\pm}$ signals seen around 775* MeV/c^2*. After Ranking, the signal is clearer.*

CHAPTER 9

EXTRACTION OF THE $\rho^{\pm}(770)$ SIGNAL

9.1 Introduction

The rate and cross-section of the $\rho^{\pm}$ meson is extracted from the invariant mass distributions of their daughter pions, $\rho^{\pm} \rightarrow \pi^{\pm} + \pi^{0}$ (BR $\approx 100\%$), by fitting the invariant mass to a sum of a background and signal functions.

It is found that the extraction of the $\rho^{\pm}$ yield from mass spectra is complicated by the large width of the resonance, by the residual Bose-Einstein correlations that affects both signal and background shape, by the reflections from other mesons (especially $\omega \rightarrow \pi^{0}\pi^{+}\pi^{-}$), by the partially reconstructed signal, and by low signal-to-background ratio due to large combinatorics.

9.2 Two-Pion Invariant Mass

Charged and neutral pion candidates are selected as described in Chapter 6. The invariant mass, $m(\pi^{\pm}, \pi^{0})$, of the $\rho^{\pm}$ meson is calculated from:

$$\begin{aligned} m^2(\pi^{\pm}, \pi^{0}) &= E^2_{\rho^{\pm}} - p^2_{\rho^{\pm}} \\ &= (E_{\pi^{\pm}} + E_{\pi^{0}})^2 - (\vec{p}_{\pi^{\pm}} + \vec{p}_{\pi^{0}})^2 \end{aligned} \tag{9.1}$$

where $E^2_{\pi} = p^2_{\pi} + m^2_{\pi}$ with $m_{\pi^{\pm}} \approx 140\,\mathrm{MeV/c^2}$ and $m_{\pi^{0}} \approx 135\,\mathrm{MeV/c^2}$ for the charged and the neutral particles respectively, $\vec{p}_{\pi}$ are the measured momentum vectors, and E_{π} are the calculated particle energies. Combinations of the pions originating from $\rho^{\pm}$ mesons, yields a wide signal peak. Wrong combinations (one, or both, pions not originating from $\rho^{\pm}$) result in a smooth combinatorial background.

9.3 Signal Reconstruction

The data are analysed in

- six intervals of scaled momentum: $x_p = p_\rho / p_{beam}$
- nine intervals of scaled energy: $x_E = E_\rho / E_{beam}$

Here $p_{beam} \approx E_{beam}$ (about 45.6 GeV) is the LEP beam momentum or energy. The result of measurements in x_p intervals are compared with those of the ALEPH ρ^0 measurement in [7], and the result for x_E intervals are compared with the OPAL measurements in [8]. These intervals are shown in Table 9.1. Since signal to background is too small for lower momenta and energy, only $x_p > 0.05$ and $x_E > 0.05$ is considered.

Table 9.1: *Scaled momentum and scaled energy intervals and ranges.*

Interval	x_p range	x_E range
1	$0.05 \leq x_p < 0.10$	$0.050 \leq x_E < 0.100$
2	$0.10 \leq x_p < 0.20$	$0.100 \leq x_E < 0.125$
3	$0.20 \leq x_p < 0.30$	$0.125 \leq x_E < 0.150$
4	$0.30 \leq x_p < 0.40$	$0.150 \leq x_E < 0.200$
5	$0.40 \leq x_p < 0.50$	$0.200 \leq x_E < 0.300$
6	$0.50 \leq x_p < 1.00$	$0.300 \leq x_E < 0.400$
7		$0.400 \leq x_E < 0.600$
8		$0.600 \leq x_E < 0.800$
9		$0.800 \leq x_E < 1.000$

Using the Monte Carlo, one can study the theoretical shape of the momentum and energy distributions for the generated and reconstructed $\rho^\pm$ mesons. The scaled momentum and the scaled energy spectra, and reconstruction efficiencies for the measurement of the $\rho^\pm$ meson are shown in Figure 9.1.

Figure 9.1a shows Monte Carlo momentum distributions for generated $\rho^\pm$ mesons (dotted line) and for reconstructed $\rho^\pm$ mesons (solid line). Figure 9.1b shows the $\rho^\pm$ reconstruction efficiency calculated by dividing the reconstructed spectra by the generated one. The six momentum intervals are indicated as well. Similarly, the scaled energy distributions for generated and reconstructed $\rho^\pm$ mesons, and corresponding reconstruction efficiency together with the nine energy different intervals are shown in Figure 9.1c and 9.1d respectively. Note that, for $x_p = x_E > 0.05$, the two distributions are approximately the same.

The mean efficiency in each interval is used to correct the extracted signal in both Monte Carlo and real data.

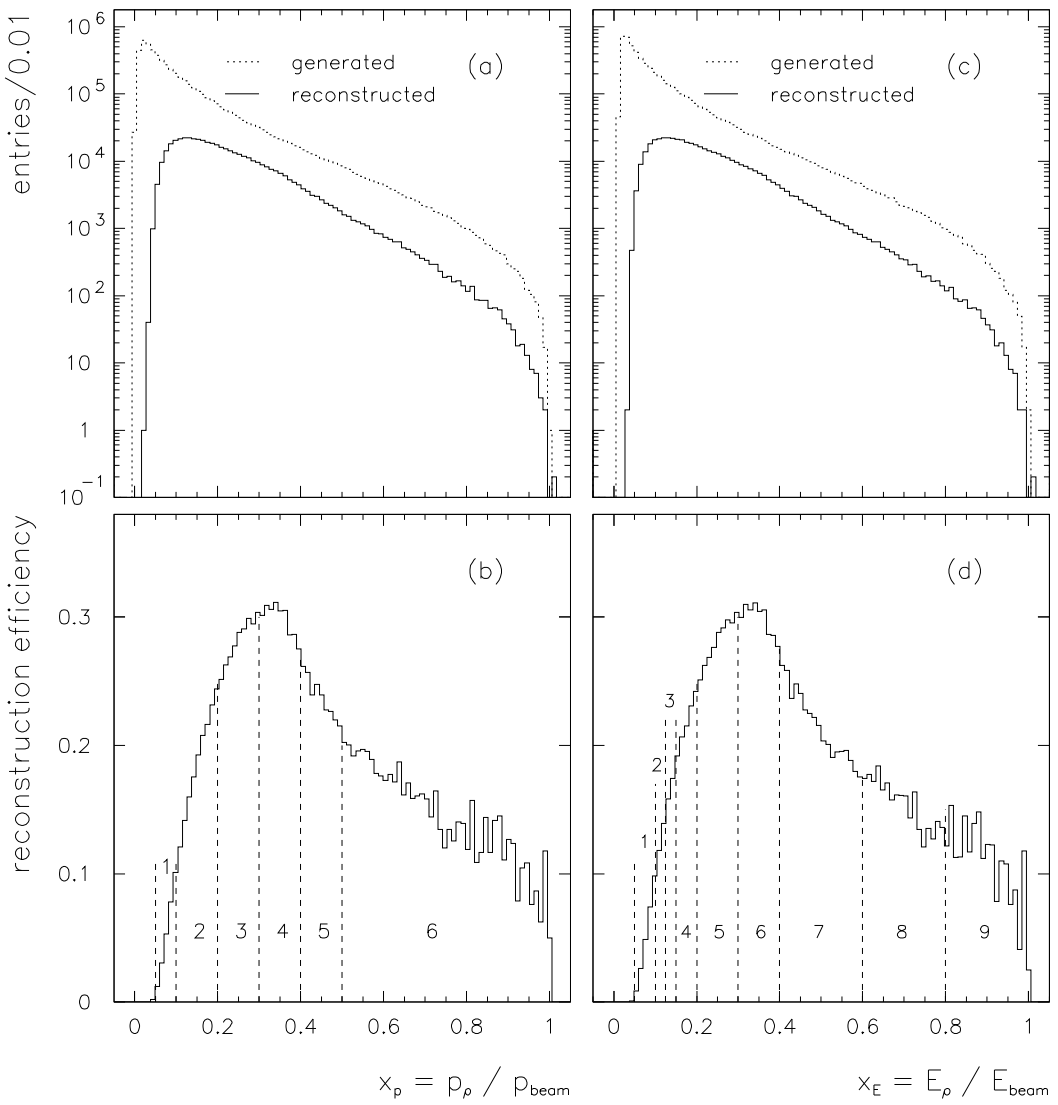

Figure 9.1: *Scaled momentum and energy spectra and reconstruction efficiencies for the $\rho^{\pm}$ meson in the Monte Carlo. (a) Distribution of x_p for generated $\rho^{\pm}$s (dotted line) and for reconstructed $\rho^{\pm}$s (solid line). (b) Reconstruction efficiency and the six momentum intervals used in extracting $\rho^{\pm}$ mesons. Similarly, x_E distributions and corresponding reconstruction efficiency together with the nine energy intervals are shown in Figure (c) and (d) respectively.*

9.4 Signal Extraction and Fitting Procedure

To extract the production rate of the $\rho^{\pm}$, the invariant mass distribution is fitted (using the method of least squares) as a sum of a background and signal function. In this section, Monte Carlo models for each component contributing to the $\pi^0\pi^{\pm}$ invariant mass will be described in detail.

9.4.1 Signal Shape

The basic line shape for the $\rho^{\pm}$ signal is a relativistic p-wave Breit-Wigner:

$$RBW(m) = \frac{m \cdot m_0 \cdot \Gamma(m)}{(m^2 - m_0^2)^2 + m_0^2 \cdot \Gamma^2(m)} \tag{9.2}$$

where m is the two-pion invariant mass evaluated from the Equation 9.1, m_0 is the resonance peak mass, and Γ is the mass dependent width. Various parameterisations for the Γ have been suggested in [16]. An example is:

$$\Gamma(m) = \Gamma_0 \cdot \left(\frac{q}{q_0}\right)^3 \frac{2q_0^2}{q_0^2 + q^2} \tag{9.3}$$

where Γ_0 is the nominal width (i.e. FWHM of the resonance), q is the momentum of the decay products in the rest frame of the parent, and q_0 is the momentum when $m = m_0$ [7]. q can be written in terms of the particle masses as follows:

$$q^2 = \frac{m^2 - m_{\pi^{\pm}}^2 + m_{\pi^0}^2}{4m^2} - m_{\pi^0}^2 \tag{9.4}$$

Monte Carlo studies can be used to check how well the fitting method reproduces the number of $\rho^{\pm}$s. However, JETSET uses a non-relativistic Breit-Wigner shape:

$$BW(m) = \frac{(\Gamma_0/2)^2}{(m - m_0)^2 + (\Gamma_0/2)^2} \tag{9.5}$$

with the tails of the distribution truncated outside the mass range 0.3 and 1.3 GeV/c^2. Therefore, the shape of the $\rho^{\pm}$ is determined separately for the real data and the Monte Carlo samples.

Figure 9.2 shows the BW and RBW function plots for the nominal values, $m_0 = 775.8 \pm 0.5$ MeV/c^2 and $\Gamma_0 = 151.5 \pm 1.2$ MeV/c^2 [9]. The BW function is symmetric, while the RBW is not. The lower tail of the RBW goes to zero at the mass threshold of $m = 0.28$ GeV/c^2. The upper tail, according to Equation 9.2, is endless, with about 90% of the signal is contained below the mass of 2 GeV/c^2.

An important consideration is the effect of partially reconstructed $\rho^{\pm}$ mesons where a π^0 is reconstructed from one photon originating from the $\rho^{\pm}$ signal and one that is not. Such a combination contains most of the kinematics of the $\rho^{\pm}$

signal and for this reason the partial signal has a similar, but wider shape. Note that π^0 Ranking reduces the number of partially reconstructed $\rho^{\pm}$s, and does not permit a signal to be reconstructed twice (once fully reconstructed, and again partially reconstructed).

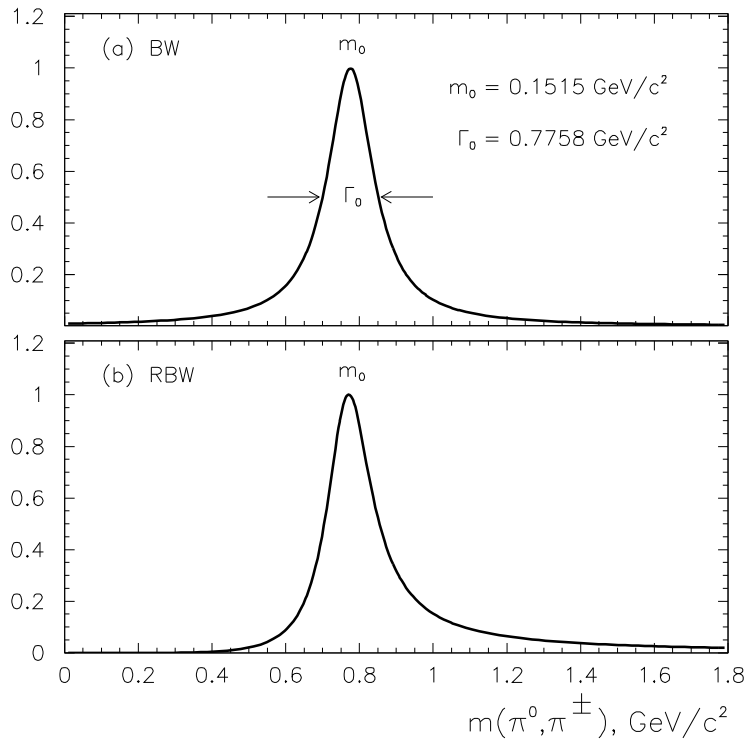

Figure 9.2: *Two normalised $\rho^{\pm}$ signal profiles for the nominal values m_0 and Γ_0. (a) The non-relativistic Breit-Wigner and resonance parameters, m_0 and Γ_0. (b) The relativistic Breit-Wigner is used to extract the real data signals.*

The width and peak mass of the resonance are different to the nominal values due to resolution effects, which is dominated by the π^0 component. The mass resolution Γ_{res} and the peak mass m_{res} parameters of $\rho^{\pm}$ mesons are determined in the Monte Carlo. An example of fits to the Monte Carlo for the fully and partially reconstructed signals are shown in Figure 9.3. The normalisation (H_F and H_P), the mass ($m_{res,F}$ and $m_{res,P}$) and the full width ($\Gamma_{res,F}$ and $\Gamma_{res,P}$) are free parameters.

Figure 9.4, for the Monte Carlo, shows the variation of the width and peak as a function of x_p and x_E for both fully and partially reconstructed $\rho^{\pm}$ signals. The position of the peak increases with increasing momentum of the $\rho^{\pm}$. m_{res} values evaluated for both have nearly the same behaviour, Figure 9.4a and 9.4b. Γ_{res} values for the fully reconstructed signal rises with increasing momentum, but the partial signal width is relatively wider and constant around 0.205 GeV/c^2, Figure 9.4c and 9.4d.

In general, the reconstruction resolution parameters are far from the generated values. In the fits, nominal m_0 and Γ_0 values are replaced by m_{res} and Γ_{res} respectively. However, the height of the partial signal is parameterised as a function of the fully reconstructed signal height, because the height of partial signal peak is correlated with fully reconstructed $\rho^{\pm}$. Consequently, only the height of the fully reconstructed signal is left as a free parameter. The Monte Carlo predictions for the ratio, $r = H_F/H_P$, of the fully and partially reconstructed signal heights are shown in Figure 9.5. The plot is only for default cuts. Note that the ratio r has a strong dependence on the photon energy cut, E_γ.

As a summary, the signal function is parametrised as a sum of two relativistic Breit-Wigner functions; $RBW_{\rm F}(m)$ for fully reconstructed signal and $RBW_{\rm P}(m)/r$ for partial signal. Each function is convoluted with its own mass resolution, Γ_{res}. Hence, the mathematical expression of the signal function is as follows:

$$f_s(m) = p_0[RBW_{\rm F}(m) + RBW_{\rm P}(m)/r] \tag{9.6}$$

where p_0 is the normalisation constant determined in the fits. Note that RBW in Equation 9.6 are replaced by BW in the Monte Carlo fits. An example of a fit to the Monte Carlo signal is shown in Figure 9.6, the signal function is truncated at 0.4 and 1.2 GeV/c^2.

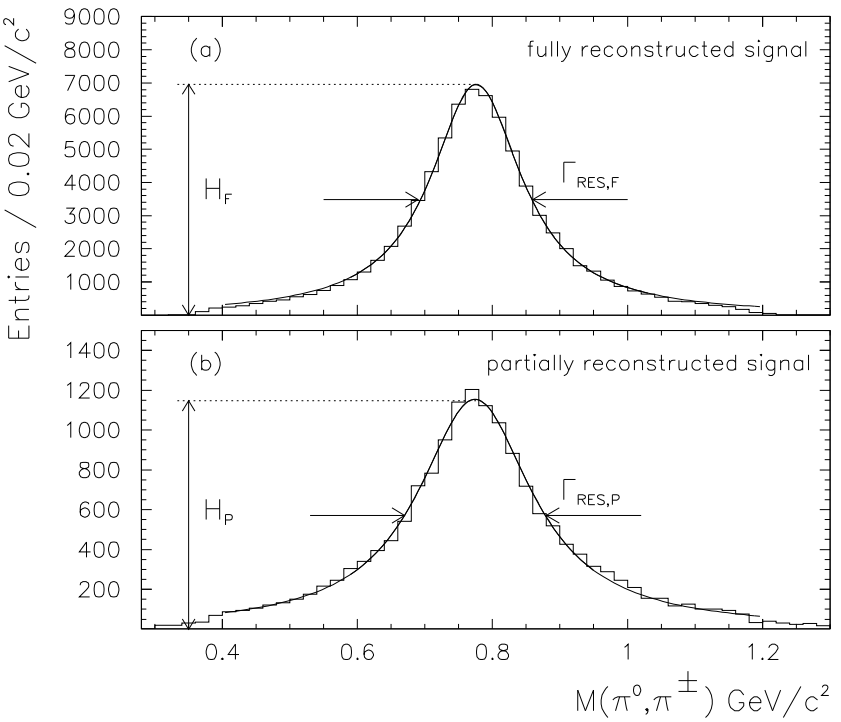

Figure 9.3: *Sample fits to the Monte Carlo for (a) fully and (b) partially reconstructed signals. The normalisation, mass and the width are free parameters. Their mass resolutions are indicated as well.*

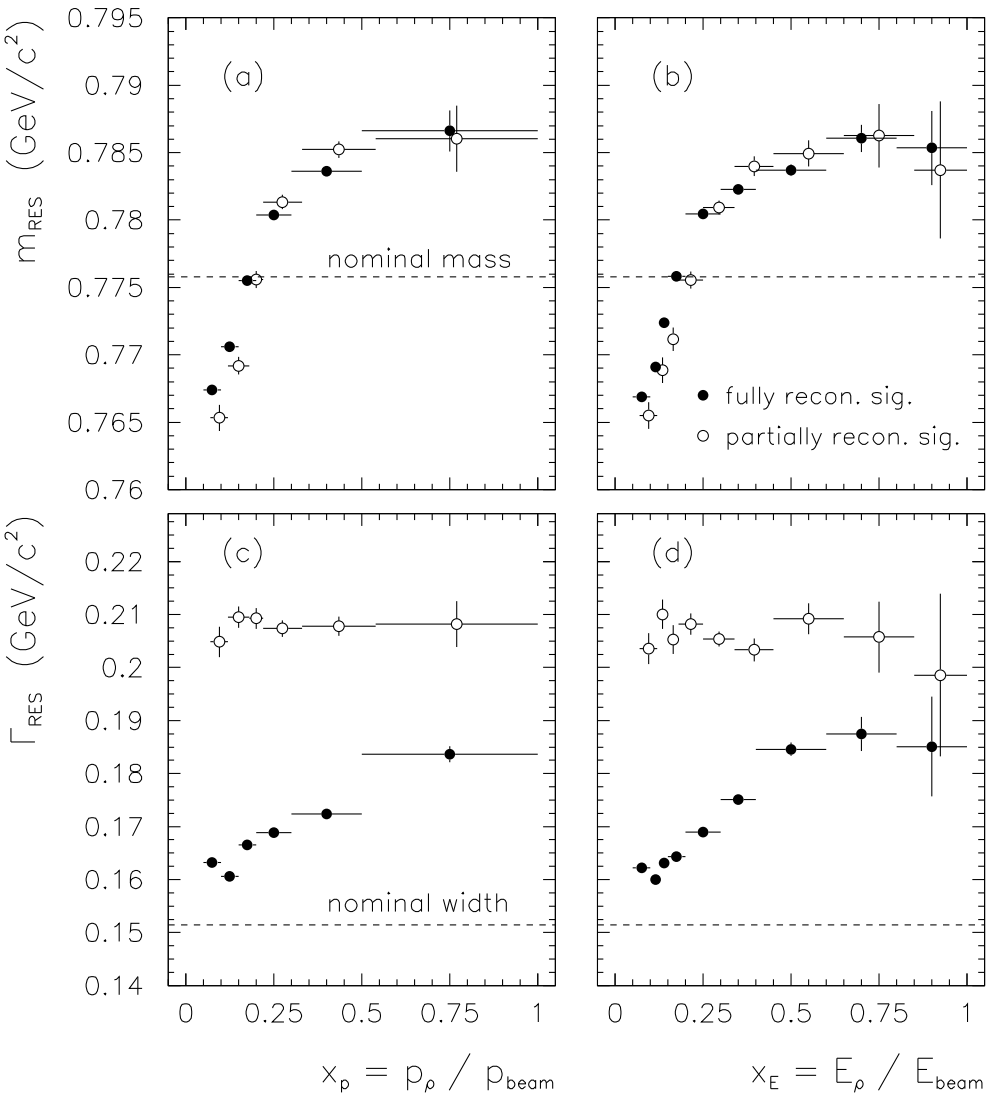

Figure 9.4: *Variations of the measured peak mass m_{res}, and mass resolution Γ_{res} as a function of x_p and x_E for fully and partially reconstructed signals. Figures (a) and (b) show the increase in the mass with increasing momentum. The measured masses are very close to each other. Figures (c) and (d) show that the measured mass resolution is always larger than the nominal width. Γ_{res} values for the fully reconstructed signal rise with increasing resonance momenta whereas the partial signal is constant at about 0.205* GeV/c^2. *The differences from the nominal values are due to detector effects.*

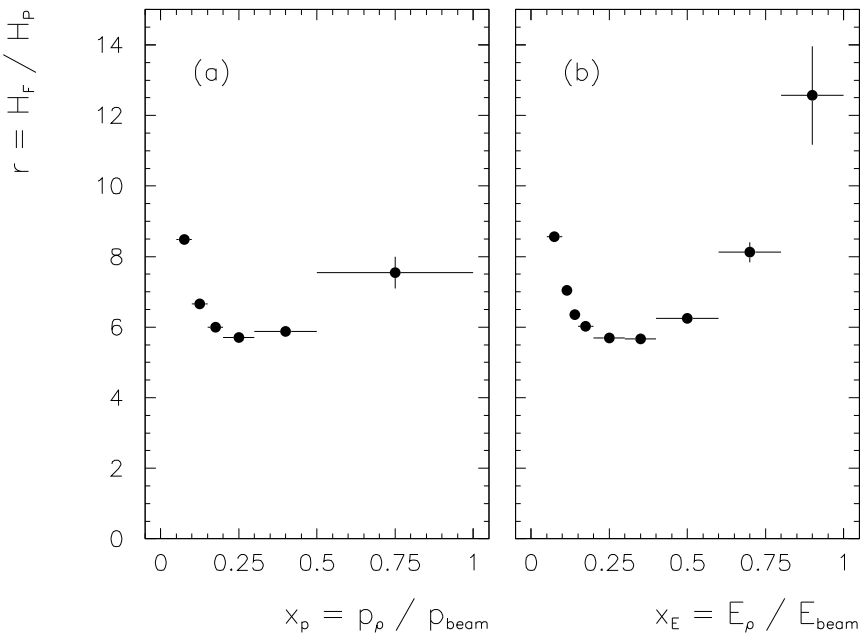

Figure 9.5: *Ratio of heights of the fully and partially reconstructed signals as a function of x_p and x_E for the default analysis cuts.*

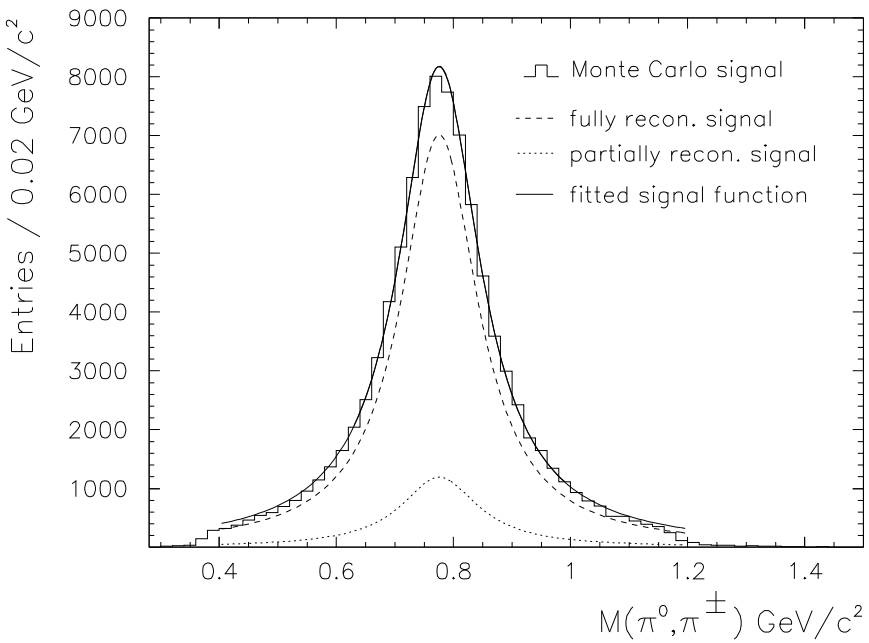

Figure 9.6: *An example of a fit to a Monte Carlo signal. The signal is composed of two Breit-Wigner functions with different mass resolutions. The height of the partial signal is parametrised as a function of the height of the fully reconstructed signal.*

9.4.2 Combinatorial Background

The combinatorial background is parameterised by the smooth function:

$$f_b(m) = p_1 m_t^{p_2} \times \exp(p_3 m_t + p_4 m_t^2 + p_5 m_t^3) \tag{9.7}$$

where $m_t = m - m_{\pi^0} - m_{\pi^\pm}$ is the cut off function, m is the invariant mass of $\pi^0\pi^\pm$ system, and p_1 to p_5 are free parameters adjusted by the fitting procedure. Figure 9.7a shows an example fit to the Monte Carlo.

9.4.3 Reflections

The $\pi^0\pi^\pm$ mass spectra contain reflections from $\omega(782) \to \pi^0\pi^+\pi^-$, $\eta(548) \to \pi^0\pi^+\pi^-$, and $K^{*\pm}(892) \to \pi^0 K^\pm$. Appropriate functions representing each reflection are selected and fitted to the Monte Carlo. While the height of the functions are fixed in the Monte Carlo, in real data the height of each reflection function is scaled by a value obtained from the measured ratio of the real data rate in Ref. [9] to the Monte Carlo rate. The scale parameters, s_p and s_E corresponding to x_p and x_E ranges, and their uncertainties, are listed in Table 9.2. Finally, these functions are added to the background function. The models for each reflection are described below.

Table 9.2: *Scale parameters s_p and s_E for each x_p and x_E bin. The values are obtained from the ratio of the real data rates to the Monte Carlo. Errors are the sum in quadrature of the statistical and systematic errors.*

	s_p *values*		
x_P *bin*	ω	η	$K^{*\pm}$
1	0.69 ± 0.11	1.05 ± 0.18	1.11 ± 0.20
2	0.75 ± 0.05	1.03 ± 0.17	1.12 ± 0.15
3	0.88 ± 0.05	1.14 ± 0.08	0.97 ± 0.18
4	0.89 ± 0.04	1.20 ± 0.08	0.89 ± 0.14
5	0.82 ± 0.03	1.38 ± 0.08	1.16 ± 0.15
6	0.56 ± 0.04	1.08 ± 0.07	1.05 ± 0.25
	s_E *values*		
x_E *bin*	ω	η	$K^{*\pm}$
1	0.64 ± 0.10	0.95 ± 0.15	0.99 ± 0.20
2	0.77 ± 0.05	1.02 ± 0.15	1.04 ± 0.16
3	0.82 ± 0.05	1.07 ± 0.10	1.06 ± 0.15
4	0.86 ± 0.05	1.13 ± 0.09	1.07 ± 0.14
5	0.87 ± 0.03	1.22 ± 0.08	1.07 ± 0.12
6	0.84 ± 0.04	1.33 ± 0.08	1.04 ± 0.16
7	0.76 ± 0.05	1.47 ± 0.10	1.00 ± 0.20
8	0.67 ± 0.06	1.63 ± 0.15	0.94 ± 0.21
9	0.58 ± 0.10	1.76 ± 0.20	0.89 ± 0.25

ω Reflection

The $\pi^0\pi^\pm$ mass distribution of $\omega \to \pi^0\pi^+\pi^-$ decays forms a broad peak at about 0.5 GeV/c^2. The ω reflection is modelled by the function:

$$f_\omega(m) = H_\omega \sin^2 \left[\pi \frac{m - m_L}{m_U - m_L}\right] \tag{9.8}$$

where $f_\omega(m)$ is restricted to the first half cycle, H_ω is the normalisation, m_L and m_U are the lower and upper intercept values of the function. An example fit to the Monte Carlo illustrating these parameters is shown in Figure 9.7b.

η Reflection

The η reflection distorts the $\pi^0\pi^\pm$ mass distribution close to $\pi^0\pi^\pm$ threshold. The model function can be choosen as:

$$f_\eta(m) = H_\eta \sin \left[\pi \frac{m - m_L}{m_U - m_L}\right] \tag{9.9}$$

where $f_\omega(m)$ is restricted to the first half cycle. An example fit to the Monte Carlo is given in Figure 9.7c.

$K^{*\pm}$ Reflection

The $K^{*\pm}$ signal in the $\pi^0 K^\pm$ mass spectra yields a peak in the $\pi^0\pi^\pm$ mass distribution close to $\rho^\pm$ peak. Assigning the pion mass to kaons results in a $K^{*\pm}$ reflection. The size of this reflection is reduced by the cuts applied to χ(dE/dx), consequently it is dominated at higher x_p and x_E ranges. The mathematical form of the model function is as follows:

$$f_{K^*}(m) = H_{K^*} \times \exp \left[m \cdot \left(\frac{m - m_{K^*}}{w_{K^*}}\right)^2\right] \tag{9.10}$$

An example fit to the Monte Carlo is given in Figure 9.7d.

9.4.4 Interference with Coherent Background

The real data mass spectra appears to be shifted to a lower mass with respect to Monte Carlo. An example of this is demonstrated in Figure 9.8.

The distortion in real data can be described succesfully by the interference effect, believed to originate from residual BECs, between the amplitudes of the $\rho^\pm$ and coherent (non-resonant) background. Note that this effect is not included in the Monte Carlo. A successful parameterisation is performed by the Söding model, used by [41] in the analysis of inclusive ρ^0 production, and by OPAL

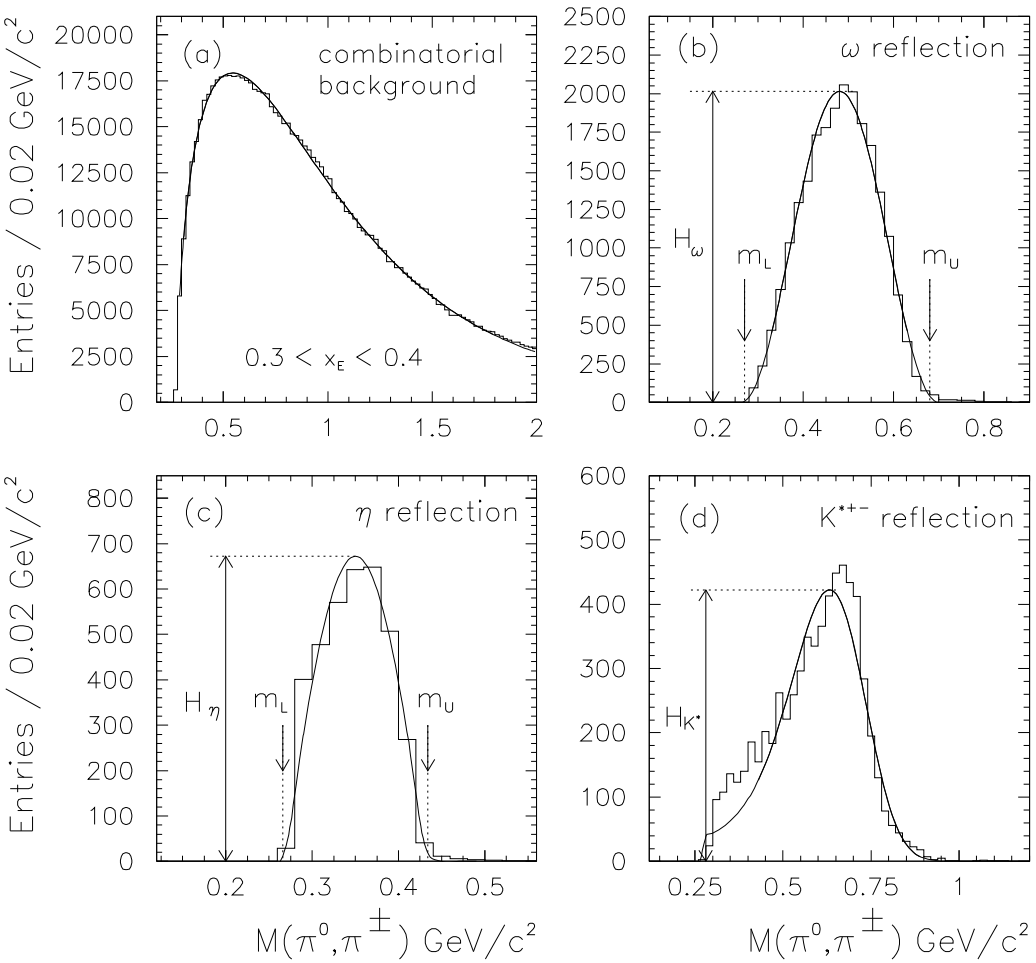

Figure 9.7: *Sample fits to Monte Carlo for (a) the combinatorial background (b) the ω reflection (c) the η reflection and (d) the $K^{*\pm}$ reflection. These model functions are fixed in the Monte Carlo. In real data fits, the height of each reflection is normalised to the real data measurements.*

group [8] in the analysis of $\rho^{\pm}$ production. To include the interference effect, the fit function is extended by adding the following term:

$$f_i(m) = C\left(\frac{m_{res}^2 - m^2}{m\Gamma(m)}\right) f_s(m) \tag{9.11}$$

where C is related to the strength of the interference and determined from data fits. Figure 9.9 shows the variation of the C value as a function of both x_p and x_E. C tends to have large values (0.7 or 0.8) at lower x_p and x_E corresponding to a large mass shift, and falls toward 0 at large x_p and x_E corresponding to no mass shift. This is consistent with the observations of [41] and [8].

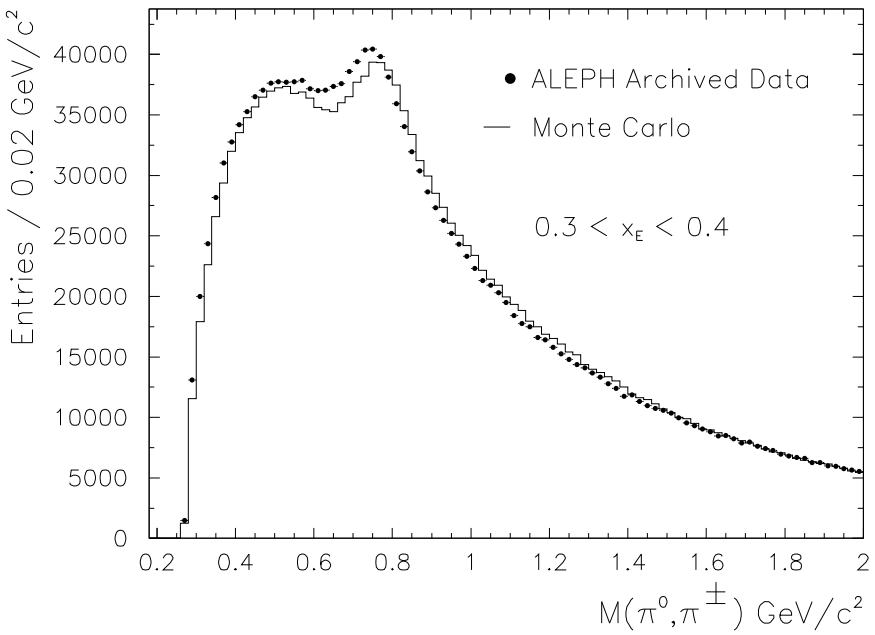

Figure 9.8: *An example two-pion mass spectra for real data and Monte Carlo. The real data mass spectra seems to be shifted to lower mass. The shift can be explained by residual BECs.*

The interference term (Equation 9.11) represents a model of the distortion that effects both the signal and backgound shapes. This can be shown by removing the interference term from the total invariant mass spectrum. Figure 9.10 shows the resulting shape of the interference term subtracted real data mass spectra for some C values. $C = 0.0$ corresponds to the original distribution. The Monte Carlo and real data disagree with each other for $C = 0.1$ and $C = 0.5$. However, the distributions are in good agreement for $C = 0.3$ which is close to its fitted value of 0.28 (see Figure 9.9). Therefore, the real data without the interference term has a similar distribution to the Monte Carlo.

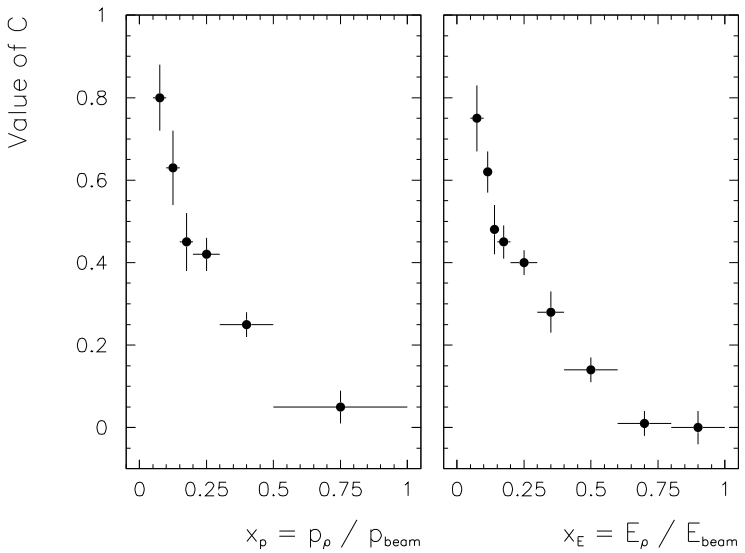

Figure 9.9: *Distribution of C values as a function of x_p and x_E. The error bars respresent the quadratic sum of statistical and systematic errors.*

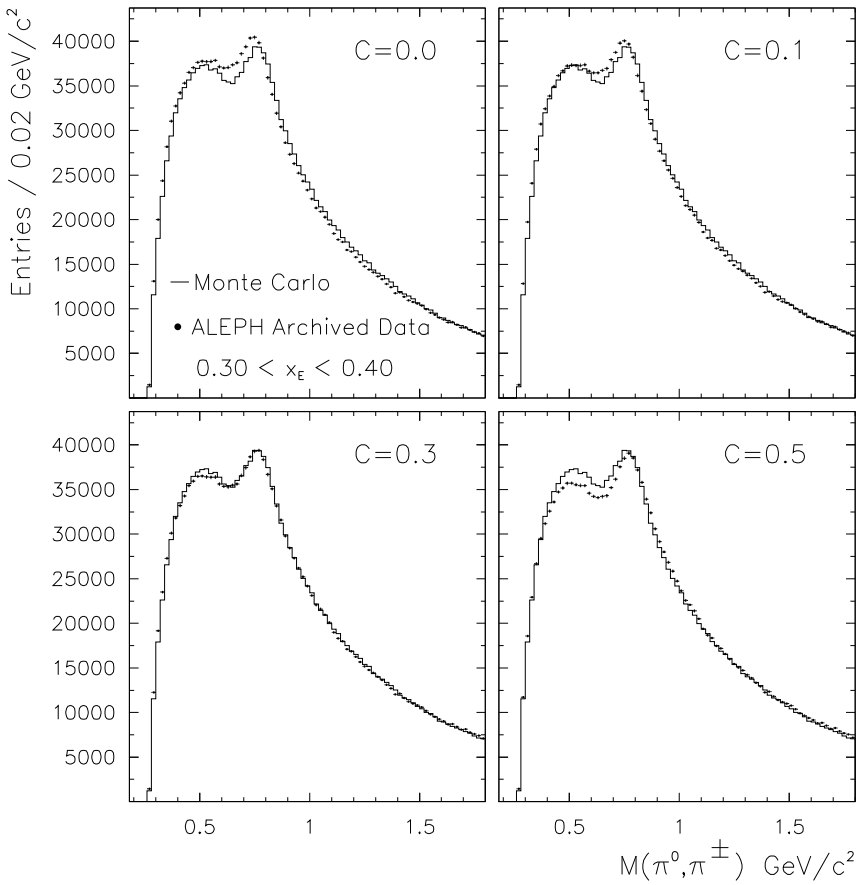

Figure 9.10: *Two pion invariant mass spectrum for the Monte Carlo, and the interference term subtracted real data for some values of the C parameter. C=0 corresponds to original spectra. Data and Monte Carlo disagree with each other for C=0.1 and 0.5. However, the real data spectra is in good agreement with the Monte Carlo for C=0.3 which is close to its fitted value of 0.28. It can be concluded that the mass shift in the data can be explained by the interference effect successfully.*

9.4.5 Total Fit Function

The total fit function is built by adding six model functions as follows:

$$\begin{aligned} F(m) &= f_s(m) + f_b(m) + f_i(m) + f_\omega(m) + f_\eta(m) + f_{K^*}(m) \\ &= p_0 \left[RBW_{\mathrm{F}}(m) + \frac{RBW_{\mathrm{P}}(m)}{r} \right] \left[1 + p_6 \left(\frac{m_{res}^2 - m^2}{m\Gamma(m)} \right) \right] \\ &+ p_1 m_t^{p_2} \times \exp(p_3 m_t + p_4 m_t^2 + p_5 m_t^3) \\ &+ H_\omega \sin^2 \left[\pi \frac{m - m_L}{m_U - m_L} \right] + H_\eta \sin \left[\pi \frac{m - m_L}{m_U - m_L} \right] \\ &+ H_{K^*} \times \exp \left[m \cdot \left(\frac{m - m_{K^*}}{w_{K^*}} \right)^2 \right] \end{aligned} \tag{9.12}$$

where p_i are free parameters. p_6 is equivalent to the C parameter in Equation 9.11. Note that, for the Monte Carlo, $f_i(m)$ is omitted, and the function RBW is replaced by BW. An example fit to real data mass spectra, illustrating each component, is shown in Figure 9.11. Figure 9.12 shows the extracted signal and the interference term for the same data in Figure 9.11. Details of the fit components and extracted functions for each momentum and energy bin are shown in Appendix D.

9.4.6 Signal Extraction

Figures 9.13 and 9.14 show the fits to the real data for each x_p and x_E range respectively. The fitting range is in general between 0.4-1.9 GeV/c^2. For each fit the normalisation of the signal is free while the width and mass are fixed to the values determined in the fit to the Monte Carlo signal. A statistical error is assigned from the uncertainty in the fitted normalisation parameter p_0.

9.5 Rates and the Differential Cross Section

The final results will be presented, for each measured momentum and energy intervals in the form of the $\rho^\pm$ production rate per event and the differential cross-section. These two quantities are calculated as follows.

The production rate, R, is calculated for each momentum and energy intervals by correcting the fitted signal S for the reconstruction efficiency ε and normalising to one event. The rates are corrected for the brancing ratio which is $BR(\rho^\pm \to \pi^\pm + \pi^0) \approx 0.9995$ for the $\rho^\pm$. The calculation is as follows:

$$R = \frac{S}{N} \frac{1}{\varepsilon} \frac{1}{BR} = \frac{S}{N} \frac{1}{\varepsilon} \tag{9.13}$$

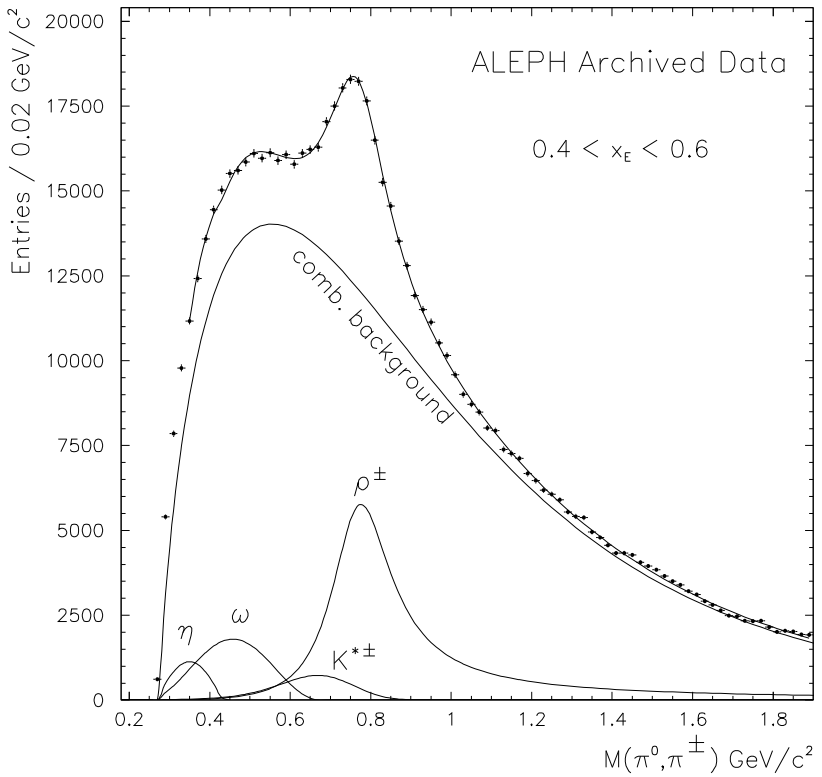

Figure 9.11: *Two-pion invariant mass spectrum. The data points are well described by the fit. The contributions from the signal, background and reflections are shown as well.*

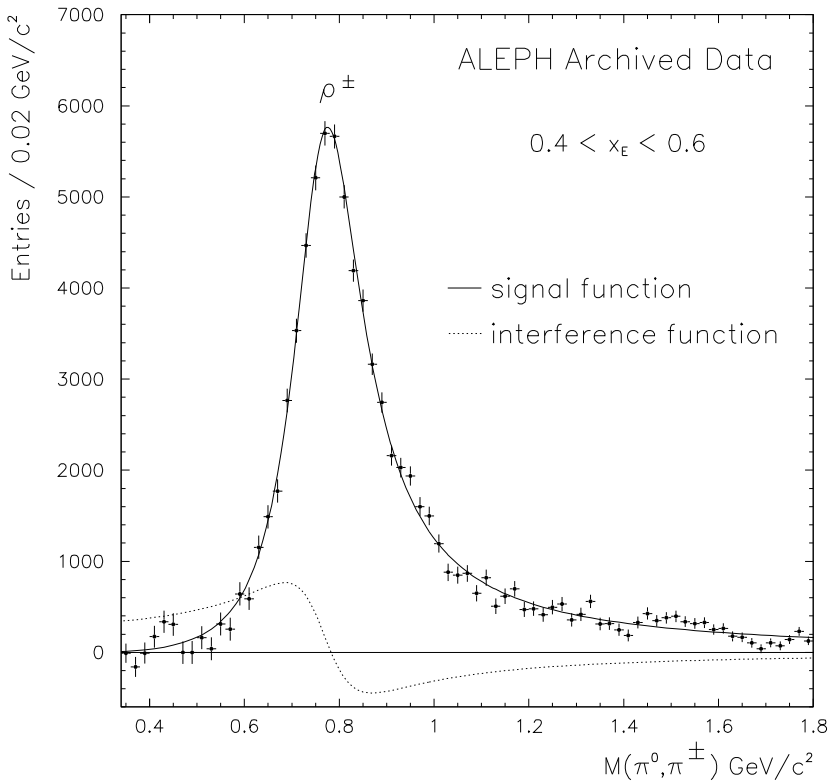

Figure 9.12: *The extracted signal, resonance curve and interference term found in the fit for the same data in Figure 9.11.*

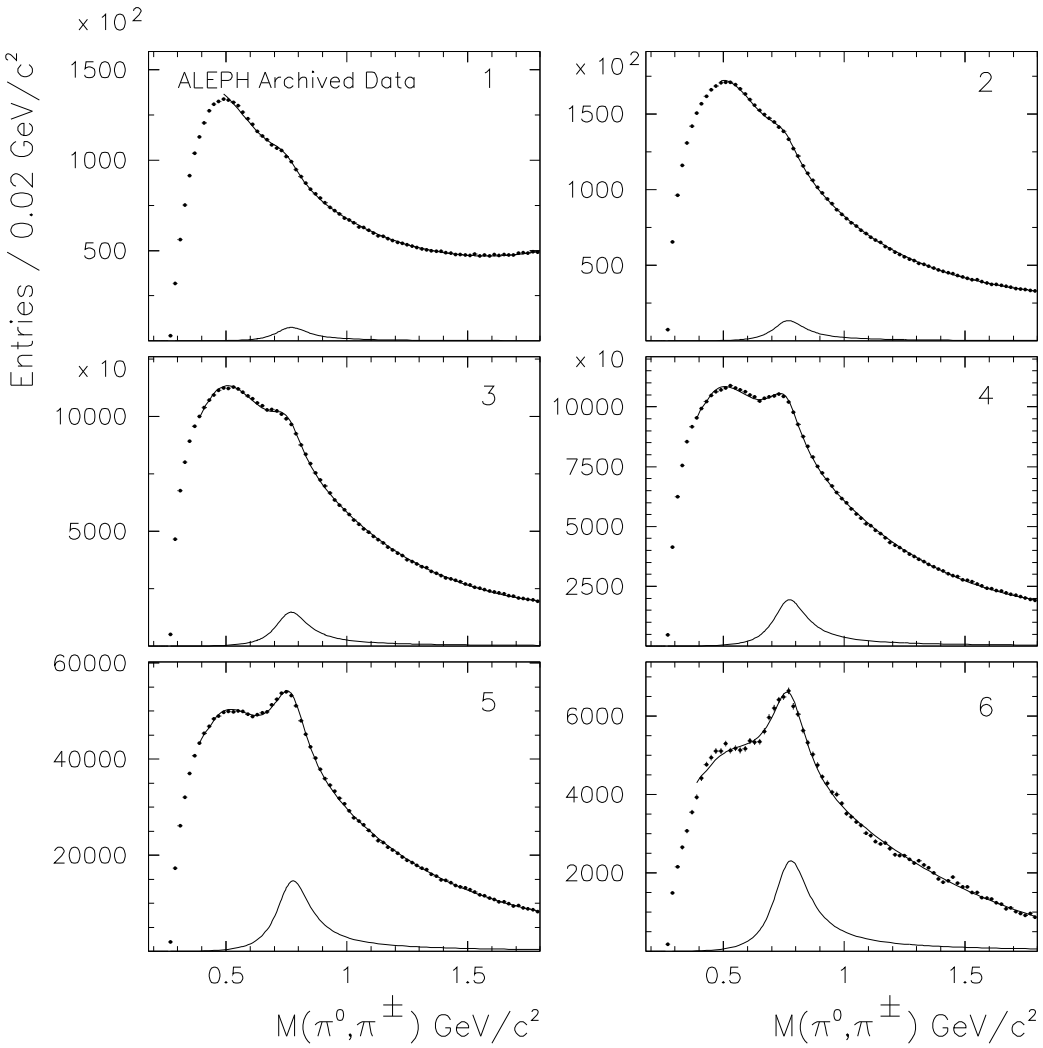

Figure 9.13: *Fits made to the real data invariant mass spectra for six x_p intervals. The extracted signal curve are also shown as well. The detail of the fit components are shown in Appendix D.*

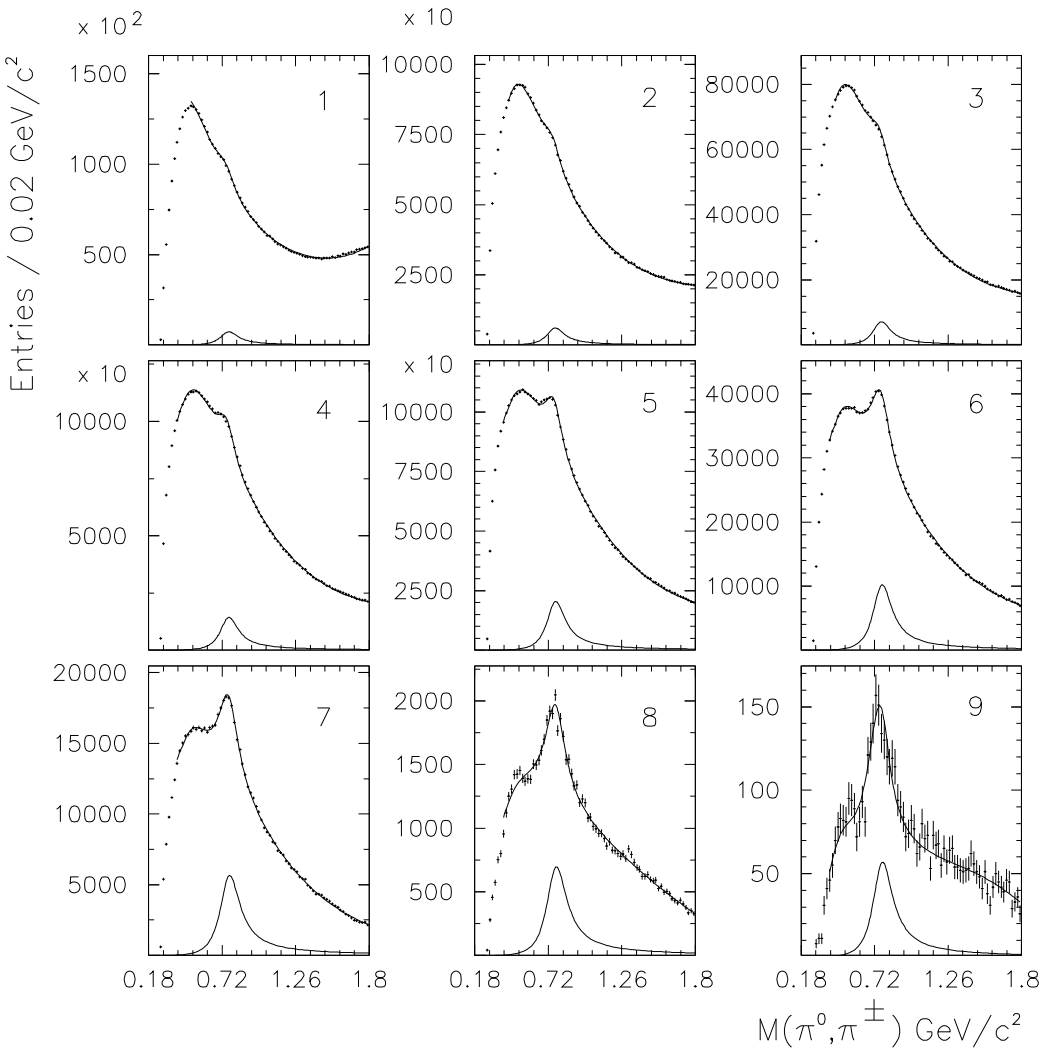

Figure 9.14: *Fits made to the real data invariant mass spectra for nine x_E intervals. The extracted signals are shown as well. The detail of the fit components are shown in Appendix D.*

where N is the total number of hadronic events obtained as:

$$N = N_{\text{gen}} \left(\frac{N_{\text{DA}}}{N_{\text{MC}}} \right) \tag{9.14}$$

where N_{gen} is the number of generated events before event selection in the Monte Carlo, N_{DA} and N_{MC} are the numbers of accepted events after preselection in data and Monte Carlo, respectively. The efficiency is defined as

$$\varepsilon = \frac{S_{\text{rec}}}{S_{\text{gen}}} \tag{9.15}$$

where S_{rec} is the number of reconstructed $\rho^{\pm}$ mesons in the Monte Carlo (macthed to the generated level) and S_{gen} is the number of generated $\rho^{\pm}$ mesons in the Monte Carlo (before event selection cuts).

Dividing the rates by the width of the momentum intervals, δx_p, gives the values for the differential cross-section, $1/\sigma_{tot} \cdot d\sigma/dx_p$, for each interval:

$$\frac{1}{\sigma_{tot}} \frac{d\sigma}{dx_p} = \frac{R}{\delta x_p} = \frac{1}{\delta x_p} \frac{S}{N} \frac{1}{\varepsilon} \tag{9.16}$$

Similarly for the energy intervals:

$$\frac{1}{\sigma_{tot}} \frac{d\sigma}{dx_E} = \frac{R}{\delta x_E} = \frac{1}{\delta x_E} \frac{S}{N} \frac{1}{\varepsilon} \tag{9.17}$$

Combining the above equations yields:

$$R = \left(\frac{S}{S_{\text{rec}}} \right) \left(\frac{S_{\text{gen}}}{N_{\text{gen}}} \right) \left(\frac{N_{\text{MC}}}{N_{\text{DA}}} \right) \quad \text{and} \quad \frac{1}{\sigma_{tot}} \frac{d\sigma}{dx} = \frac{R}{\delta x} \tag{9.18}$$

where x can be x_p or x_E. Tables 11.1 and 11.2 show the results of the above calculations together with statistical and systematic errors for x_p and x_E intervals respectively.

9.6 Comparison of Data and Monte Carlo

The ratio of the fitted signal S to the number of reconstructed $\rho^{\pm}$ mesons S_{rec} in the Monte Carlo as a function of both x_p and x_E are plotted in Figure 9.15. For comparison, the ratio of the ALEPH data measurements to OPAL data is given in Figure 9.16 as well. The error bars represent the quadratic sum of the statistical and systematic contributions.

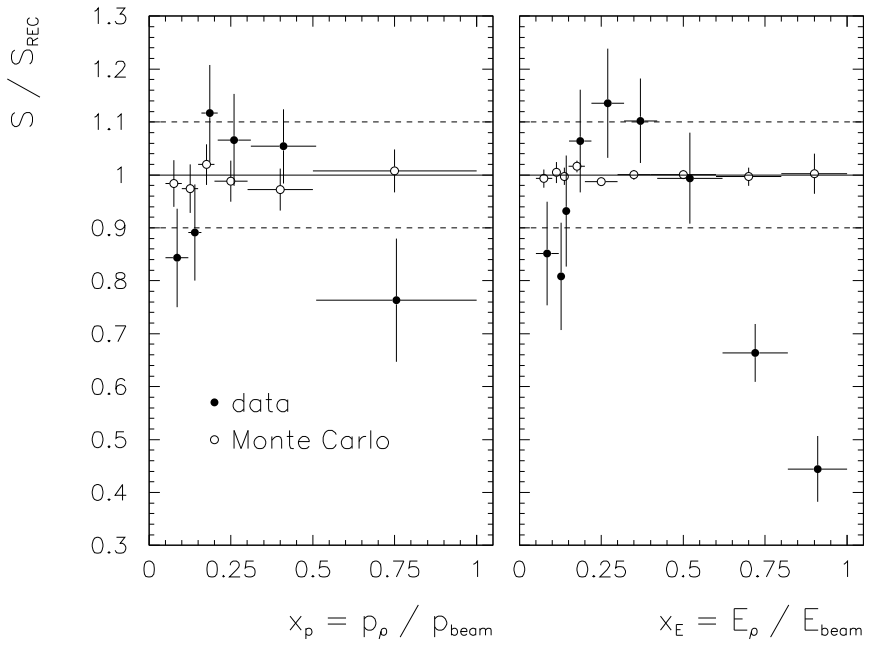

Figure 9.15: *Ratio of the fitted signal to the number of reconstructed $\rho^{\pm}$ mesons in the Monte Carlo. Error bars represent the sum in quadrature of the statistical and systematical errors. The dotted line shows a 10% disagreemnet.*

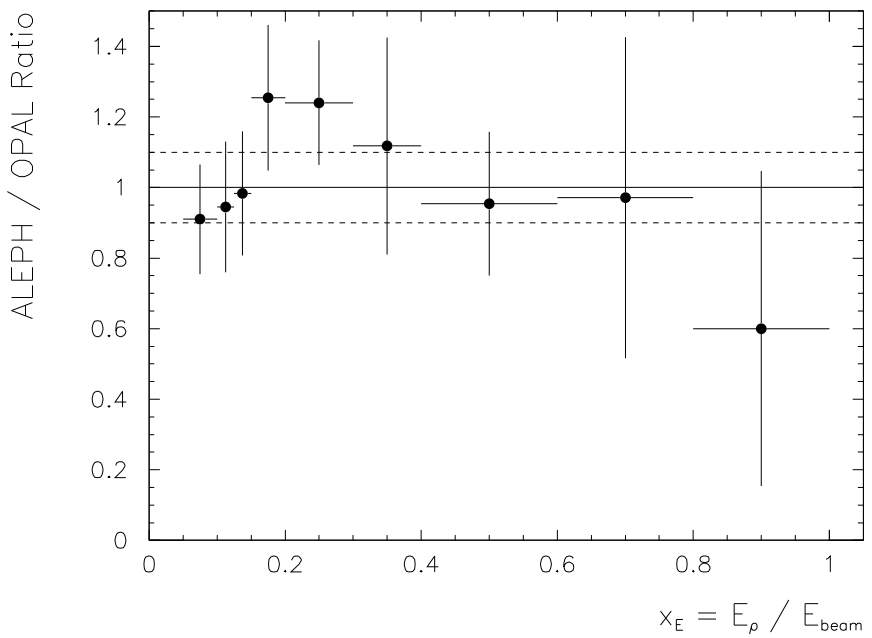

Figure 9.16: *Ratio of the ALEPH rates to the OPAL rates. The dotted line indicated a 10% disagreement.*

CHAPTER 10

SYSTEMATIC ERROR ANALYSIS

10.1 Introduction

While statistical errors originate from counting uncertainties (statistical uncertainties) that result in measured values being randomly high or low, systematic errors originate from detector effects, uncertainties in models and measurement procedures that result in measured values being systematically high or low.

The study of systematic uncertainties for this analysis takes various forms; the details are given in the following sections. The results, including statistical errors, are summarised in Tables 10.4 and 10.5 at the end of this chapter.

10.2 Source of Systematic Errors

In this study, the possible source of systematic errors are categorised into five groups; track selection cuts, fitting procedure, reflection models, signal function and efficiency correction. An additional systematic error due to the uncertainty in the extraploation to full x_p and x_E ranges is included in the final results.

10.2.1 Track Selection Cuts

The calculation of the efficiency corrections relies on an adequate reproduction of the detector acceptances by the Monte Carlo. Repeating the measurement with different (though reasonable) values of cuts applied to the track selection results in variations in the measured $\rho^{\pm}$ rate. Such variations can be interpreted as discrepancies between the calculated efficiency and the true efficiency for the reconstruction of the $\rho^{\pm}$ signal. However, it is expected that varying cuts will also give rise to statistical variations that are already accounted for in the assignment

of statistical errors. This is supported by the observation that, variations due to track selection cuts are seen to be random in magnitude and sign in general. Therefore the following results for systematic errors due to track selection cuts are considered to be over-estimates (conservative).

All default values of the cuts and their variations are summurised at the end of this section in Table 10.1. The largest variation in the measured rate for each cut in each x_p and x_E interval is assigned to the systematic error.

Photon Energy, E_γ

A cut of 1.0 GeV is applied on the energy of photons. The cut is increased to 1.2 GeV and decreased to 0.8 GeV. The largest contribution in the track selection cuts comes from this cut which dominates especially at low x_p and x_E (about 6%). The fluctuations tend to be larger in the real data with respect to Monte Carlo.

π^0 Energy, E_{π^0}

A cut of 18 GeV is applied on the energy of neutral pion candidates. The cut is increased to 20 GeV and decreased to 16 GeV. The maximum variations are observed at low and highest x_p and x_E (about 4%).

π^0 Mass Window, σ

A mass window of $\pm 2.0\sigma$ is used to select π^0 candidates from the two-photon invariant mass spectra. The cut is varied to $\pm 1.5\sigma$ and $\pm 3.0\sigma$. Maximum fluctuations are less than 5% for each momentum and energy bins.

π^0 Matching, λ

In π^0 matching, a search for the best match between the generated and reconstructed candidates is performed. The procedure of π^0 matching is described in Appendix C in detail. A λ parameter discriminating between the the best matches and true matches is defined in the matching procedure.

A cut of $\lambda < 0.3$ is applied to a π^0 candidate to flag it as a true match. Changing the value of the cut results in a systematic error since it affects the calculation of the efficiency correction for the $\rho^\pm$ meson. The cut is increased to 0.4 and decreased to 0.2. The maximum difference in the number of matched π^0s is taken as the systematic error. The variations are nearly constant and less than 1% for each momentum and energy bin.

Transverse Impact Parameter, d_0

The cut applied to the transverse impact parameter of charged tracks is 0.5 cm. This cut is decreased to 0.3 cm and increased to 1.0 cm. The largest variation is found to be about 5%, occuring in the lowest x_p bin.

Ionisation Energy Loss, χ(dE/dx)

A cut of $-2 < \chi(\mathrm{dE/dx}) < 3$ is applied on energy loss for charged tracks. The rate extraction procedure is repeated after omitting the cuts completely. The difference is taken as a systematic error.

Table 10.1: *Summary of the applied track cuts and variations in their values, used in the systematic error analysis.*

Source of error	*Default value*	*Changes*
E_γ	1.0 GeV	0.8, 1.2 GeV
E_{π^0}	18 GeV	16, 20 GeV
σ	± 2.0	± 1.5, ± 3.0
λ	0.3	0.2, 0.4
d_0	0.5 cm	0.3, 1.0 cm
$\chi(dE/dx)$	$[-2, 3]$	removed

10.2.2 Fitting Procedure

Uncertainties in the fitting procedure are a significant source of systematic errors. The fluctuations in the extracted rates are found to be random in magnitude and sign. In the fitting procedure, the mass range covered by the fits in general is 400-1900 MeV/c^2. The mass range is varied by ± 40 MeV/c^2. These fitting ranges are given in Table 10.2.

Table 10.2: *The default and modified fit ranges used in the systematic error analysis.*

x_p *or* x_E *bin*	*Default range* MeV/c^2	*Increased range* MeV/c^2	*Decreased range* MeV/c^2
1	500 - 1900	496 - 1940	540 - 1860
2	440 - 1900	400 - 1940	480 - 1860
3-9	400 - 1900	360 - 1940	440 - 1860

10.2.3 Reflection Models

As described in Section 9.4.3, reflections from ω, η and $K^{*\pm}$ mesons are modelled and their shapes are fixed in the Monte Carlo. In real data fits, the height of each reflection is normalised, by the scale parameters s_p and s_E, to the real data measurements. The value of s_p (and s_E) for each momentum bin is varied by its corresponding uncertainty, i.e. $\pm$ one standard deviation taken from Table 9.2. The procedure is repeated for each reflection independently, the largest variations in the measured rate are taken as the systematic error. The fluctuations are mainly due to the ω reflection.

10.2.4 Signal Function

The width and mass of the resonance are taken from the Monte Carlo. In the fits the width is varied by $\pm 5\%$. The largest variations in the values for the extracted signals are taken as the systematic uncertainties. Maximum fluctuations are about 3% for each momentum and energy bin.

One of the significant contributions to the systematic errors comes from the consideration of the partially reconstructed signal which can be considered either a part of signal or background. The difference in the evaluated rates are taken as a systematic error. Maximum fluctuations are less than 4%.

10.2.5 Efficiency Correction

Efficiency ε, defined in Equation 9.15, has a statistical uncertainty due to counting of the reconstructed Monte Carlo signals S_{rec}. Consequently, the uncertainty in S_{rec} causes a variation in the calculated rate and therefore a systematic error. The fluctuations are about 0.2% for all momentum and energy bins except for highest bins.

10.2.6 Extrapolation to $x_p = 0$ and $x_E = 0$

The measurement covers only the regions where $x_p > 0.05$ and $x_E > 0.05$. To estimate the total production rate, the total measured rate is extrapolated to $x_p = 0$ and $x_E = 0$ using the fragmentation function in the Monte Carlo. The unmeasured fraction of the total rate in the real data is about 40% for $x_p < 0.05$ and 38% for $x_E < 0.05$. The procedure relies on the Monte Carlo to give the correct scale factor for the extrapolation. To estimate the uncertainty in the scale factor the calculation is repeated for different Monte Carlos, the results are listed in Table 10.3. The largest difference, about 1.6%, is between JETSET and PYTHIA. This value is taken as an additional systematic uncertainty.

Table 10.3: *Estimated values of unmeasured fraction and corresponding scale factors for different Monte Carlo programs.*

Monte Carlo Program	*Unmeasured Fraction*		*Scale Factor*	
	$x_p < 0.05$	$x_E < 0.05$	$x_p = 0$	$x_E = 0$
JETSET 7.4 (ALEPH tuning)	40.0 %	37.9 %	1.666	1.610
PYTHIA 6.4 (default tuning)	40.9 %	38.8 %	1.693	1.635
HERWIG 6.5 (default tuning)	40.2 %	38.1 %	1.673	1.615

10.3 Summary of Errors

Table 10.4 and 10.5 summarise the statistical and systematic errors for the $\rho^{\pm}$ measurement in x_p and x_E intervals respectively. For the systematic errors, the individual errors from each source are shown for each measured momentum and energy intervals.

The total error 'e_{all}' for the total measured ranges, calculated for each error source, is taken as the sum of the errors, e_i, in each interval (horizontally in the table) weighted by the rate, R_i, in each interval. For this, the quadratic sum

$$e_{all} = \frac{\sqrt{\sum (e_i R_i)^2}}{\sum R_i} \tag{10.1}$$

is taken in the cases where systematic errors are considered to be uncorrelated between momentum or energy intervals, i.e. they are considered to be dominated by statistical variations. However, the linear sum

$$e^*_{all} = \frac{\sum e_i R_i}{\sum R_i} \tag{10.2}$$

is used for the cases (flagged by a '$*$' symbol) where the errors are considered to be correlated.

The total systematic error, e_{tot}, for each momentum and energy interval, including the summed interval '*all*', is calculated by taking the quadratic sum of each error source e_k (vertically in the table). Hence

$$e_{tot} = \sqrt{\sum e_k^2} \tag{10.3}$$

The last row of each table shows the total error for all, and each momentum and energy interval, calculated as the quadratic sum of the total systematic error and the statistical error.

The systematic errors dominate the uncertainty in the measured $\rho^{\pm}$ rate. However, a large component of these errors are considered to be mostly due to the instability of the fitting procedure in the presence of varyng signal and background. The assignment of systematic errors is therfore considered to be conservative.

Table 10.4: *Systematic and statistical errors for the $\rho^{\pm}$ rate in each measured momentum interval. All values are expressed in % rounded to one decimal place.*

Source of error		*measured x_p interval*					
	e_{all}	1	2	3	4	5	6
Fit range	1.9	0.4	2.4	2.1	4.4	0.8	6.8
Eff. correction	0.1	0.2	0.2	0.2	0.2	0.2	0.4
Signal width	1.6	3.6	3.2	2.1	2.8	3.5	5.6
Partial signal	*3.0	2.7	3.4	3.5	3.3	3.0	2.1
ω rate	*1.5	2.0	1.7	1.5	0.7	0.3	0.8
η rate	*0.3	0.0	0.0	0.5	1.1	0.2	0.0
$K^{*\pm}$ rate	*0.7	0.0	1.2	2.7	0.1	0.1	2.8
π^0 matching	*0.7	0.6	0.7	0.8	0.7	0.9	0.6
E_γ	2.6	6.0	6.1	3.1	3.2	3.2	3.0
E_{π^0}	1.5	3.5	3.7	2.4	1.5	1.6	4.6
π^0 mass window	1.3	2.6	3.1	2.7	3.5	2.3	3.3
$\chi(dE/dx)$	1.1	2.8	1.3	1.7	0.7	1.6	2.6
d_0	2.0	5.2	1.9	2.7	0.8	0.4	3.7
Systematic error (e_{tot})	5.7	10.7	10.0	8.0	8.1	6.5	12.3
Statistical error	1.1	2.5	2.2	1.6	0.9	0.9	2.2
Total error	5.8	11.0	10.2	8.1	8.1	6.6	12.5

Table 10.5: *Systematic and statistical errors for the $\rho^{\pm}$ rate in each measured energy interval. All values are expressed in % rounded to one decimal place.*

Source of Error		*measured x_E interval*								
	e_{all}	1	2	3	4	5	6	7	8	9
Fit range	1.9	4.7	2.6	3.9	3.3	1.5	2.2	3.7	2.8	2.5
Eff. correction	0.1	0.2	0.2	0.2	0.2	0.2	0.2	0.3	0.6	1.8
Signal width	1.6	3.4	3.9	3.8	3.4	3.5	3.3	3.4	3.6	2.8
Partial signal	*3.2	2.9	3.6	3.5	3.7	3.4	3.0	2.7	1.3	1.9
ω rate	*1.7	1.6	2.9	3.2	1.0	2.2	0.3	0.4	0.2	0.1
η rate	*1.5	1.7	2.3	2.5	2.2	0.3	0.2	0.2	1.2	0.0
$K^{*\pm}$ rate	*0.5	0.0	2.7	1.6	0.3	0.1	0.1	0.3	1.9	2.6
π^0 matching	*0.7	0.6	0.7	0.7	0.8	0.7	0.8	0.8	0.6	0.5
E_γ	2.8	6.3	5.0	4.0	4.5	6.4	3.8	4.3	2.5	4.4
E_{π^0}	1.2	3.0	2.4	3.5	0.7	0.4	1.0	3.1	0.2	8.8
π^0 mass window	2.0	4.7	4.7	4.3	3.8	2.8	2.2	3.0	2.2	5.9
$\chi(dE/dx)$	1.1	2.3	4.9	2.5	1.7	0.6	2.1	1.0	4.1	5.7
d_0	0.8	1.7	4.0	2.5	0.7	0.4	0.2	0.4	1.1	3.2
Systematic error (e_{tot})	6.1	11.3	12.3	11.0	9.0	9.0	7.1	8.5	7.6	14.2
Statistical error	1.0	2.3	2.7	2.4	1.2	0.9	1.2	1.2	3.4	6.3
Total error	6.2	11.5	12.6	11.3	9.1	9.1	7.2	8.6	8.3	15.5

CHAPTER 11

RESULTS AND CONCLUSION

11.1 Results

In this section, the results obtained from the ALEPH measurement for $\rho^{\pm}$ meson are presented, and compared with the OPAL measurement in [8] and Monte Carlo event generator programs.

11.1.1 Rates and Differential Cross-sections

Table 11.1 and 11.2 shows the results for the $\rho^{\pm}$ rates and differential cross-sections in each measured momentum and energy intervals respectively. The errors correspond to statistical and systematic errors respectively. The result of summing over the measured x_p and x_E intervals is shown; the final row in each table gives the result of extrapolating this to $x_p = 0$ and $x_E = 0$ together with an extra error of about 1.6% representing the uncertainty in the extrapolation.

The differential cross-sections as a function of x_p are compared to Monte Carlo predictions in Figure 11.1. A similar plot is constructed for the x_E intervals to compare the ALEPH results with OPAL measurements in Figure 11.2. The errors shown are the quadratic sum of statistical and systematic contributions. Note that while the first interval shown in Figure 11.2 is unmeasured for ALEPH, OPAL presents in [8] measurements down to $x_E = 0.016$.

11.1.2 Total Multiplicity

The ALEPH result for the total multiplicity per hadronic event, $N(\rho^{\pm})$, is compared with the OPAL result and Monte Carlo programs in the second column of Table 11.3 and in Figure 11.3a.

Table 11.1: *Measured multiplicities and differential cross-sections for the $\rho^{\pm}$ in x_p intervals. The result of summing over the measured x_p intervals is also given, including extrapolation to full x_p range with an additional error due to the uncertainty in the extrapolation.*

x_p *range*	*Multiplicity* $\rho^{\pm}(770)$*/ Z decay*	$1/\sigma_{had} d\sigma/dx_p$
0.05-0.10	$0.5622 \pm 0.0142 \pm 0.0603$	$11.2434 \pm 0.2840 \pm 1.2069$
0.10-0.15	$0.3162 \pm 0.0068 \pm 0.0315$	$6.3246 \pm 0.1364 \pm 0.6299$
0.15-0.20	$0.2338 \pm 0.0037 \pm 0.0187$	$4.6756 \pm 0.0736 \pm 0.3731$
0.20-0.30	$0.2335 \pm 0.0022 \pm 0.0189$	$2.3347 \pm 0.0216 \pm 0.1889$
0.30-0.50	$0.1663 \pm 0.0015 \pm 0.0109$	$0.8316 \pm 0.0073 \pm 0.0545$
0.50-1.00	$0.0412 \pm 0.0009 \pm 0.0051$	$0.0823 \pm 0.0018 \pm 0.0102$
0.05-1.00	$1.5532 \pm 0.0164 \pm 0.0880$	
all x_p	$2.5872 \pm 0.0273 \pm 0.1466 \pm 0.0428$	

Table 11.2: *Measured multiplicities and differential cross-sections for the $\rho^{\pm}$ in x_E intervals. The result of summing over the measured x_E intervals is also given, including extrapolation to full x_E range with an additional error due to the uncertainty in the extrapolation.*

x_E *range*	*Multiplicity* $\rho^{\pm}(770)$*/ Z decay*	$1/\sigma_{had} d\sigma/dx_E$
0.050-0.100	$0.6050 \pm 0.0137 \pm 0.0683$	$12.0992 \pm 0.2740 \pm 1.3650$
0.100-0.125	$0.1679 \pm 0.0046 \pm 0.0206$	$6.7153 \pm 0.1840 \pm 0.8237$
0.125-0.150	$0.1450 \pm 0.0035 \pm 0.0160$	$5.7990 \pm 0.1400 \pm 0.6407$
0.150-0.200	$0.2258 \pm 0.0027 \pm 0.0204$	$4.5151 \pm 0.1090 \pm 0.4072$
0.200-0.300	$0.2506 \pm 0.0023 \pm 0.0226$	$2.5056 \pm 0.0230 \pm 0.2259$
0.300-0.400	$0.1151 \pm 0.0014 \pm 0.0082$	$1.1511 \pm 0.0140 \pm 0.0820$
0.400-0.600	$0.0820 \pm 0.0010 \pm 0.0070$	$0.4102 \pm 0.0050 \pm 0.0349$
0.600-0.800	$0.0146 \pm 0.0005 \pm 0.0011$	$0.0729 \pm 0.0025 \pm 0.0055$
0.800-1.000	$0.0016 \pm 0.0001 \pm 0.0002$	$0.0078 \pm 0.0005 \pm 0.0011$
0.050-1.000	$1.6076 \pm 0.0154 \pm 0.0981$	
all x_E	$2.5878 \pm 0.0248 \pm 0.1579 \pm 0.0408$	

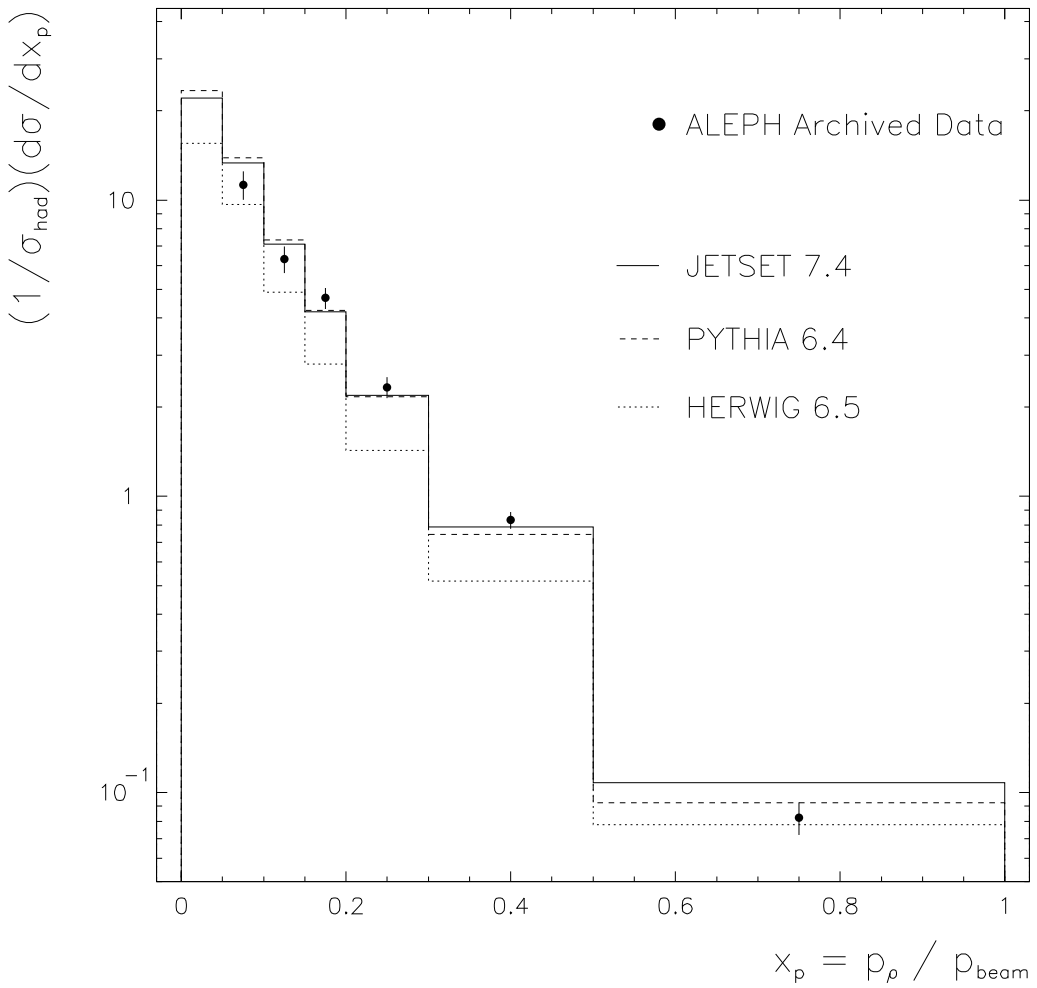

Figure 11.1: *Differential cross-sections for the $\rho^{\pm}$ as a function of x_p in comparision with the Monte Carlo predictions. The errors shown are the quadratic sum of the statistical and systematic contributions.* Jetset *7.4 is ALEPH tuned, while* Pythia *and* Herwig *have default tuning. The first interval is unmeasured for ALEPH.*

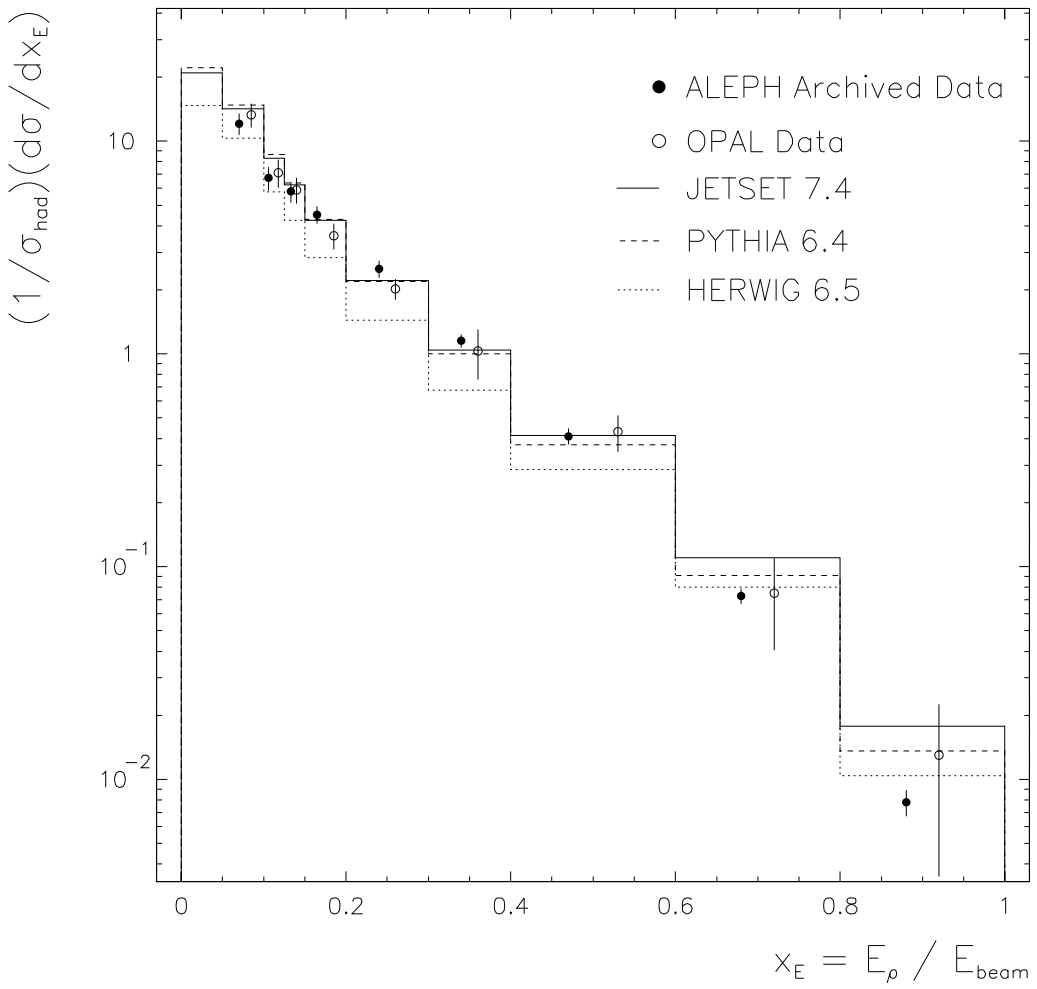

Figure 11.2: *Differential cross-sections for the $\rho^{\pm}$ as a function of x_E in comparision with OPAL measurements and the Monte Carlo predictions. The errors shown are the quadratic sum of the statistical and systematic contributions.* JETSET *7.4 is ALEPH tuned, while* PYTHIA *and* HERWIG *have default tuning. The first interval is unmeasured for ALEPH. OPAL measurements below $x_E = 0.05$ are omitted.*

11.1.3 Isospin Dependence

The production rates of $\rho^{\pm}$ can be compared with its isospin partner, the ρ^0. The ratio of the rates, $2N(\rho^0)/N(\rho^{\pm})$, is expected to be one, since $I = 1$ for ρ triplet. The value of the $2N(\rho^0)/N(\rho^{\pm})$ is obtained using the ALEPH measurement in [7] and the result is compared with the OPAL value in [8] and Monte Carlo predictions in the last column of the Table 11.3 and in Figure 11.3b. The deviation from unity comes from heavy flavour decays such as $\eta' \to \rho^0\gamma$.

Table 11.3: *Comparison of the total multiplicity of the $\rho^{\pm}$, $N(\rho^{\pm})$ and the ratio $2N(\rho^0)/N(\rho^{\pm})$ as measured by ALEPH to OPAL and Monte Carlo predictions. Errors are statistical and systematic respectively.*

Data set	$N(\rho^{\pm})$	$2N(\rho^0)/N(\rho^{\pm})$
ALEPH data	$2.59 \pm 0.03 \pm 0.15$	$1.12 \pm 0.05 \pm 0.17$
OPAL data	$2.40 \pm 0.06 \pm 0.43$	$1.08 \pm 0.04 \pm 0.20$
JETSET 7.4	2.77	1.06
PYTHIA 6.4	2.85	1.07
HERWIG 6.5	1.93	1.04

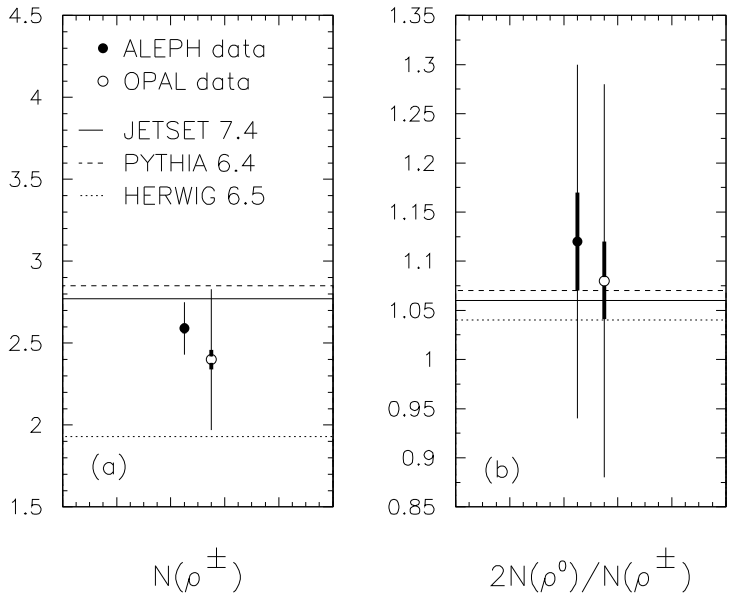

Figure 11.3: *Comparison of ALEPH measurement of (a) $N(\rho^{\pm})$ and (b) $2N(\rho^0)/N(\rho^{\pm})$ with the OPAL data and Monte Carlo models. The values are taken from Table 11.3. The error bars in bold are statistical errors.*

11.1.4 The Cross-Section as a Function of ξ_p

In Figure 11.4 the measured cross-section for the $\rho^{\pm}$, in comparison with the OPAL data and Monte Carlo predictions, is given as a function of $\xi_p = \ln(1/x_p)$. The modified leading logarithm approximation combined with the local parton-hadron duality model [42] predicts that the position of the maximum is correlated with the mass of the particle, i.e. the momentum spectrum is expected to be harder for particles with higher masses. However, this position may be modified by heavy flavour decays.

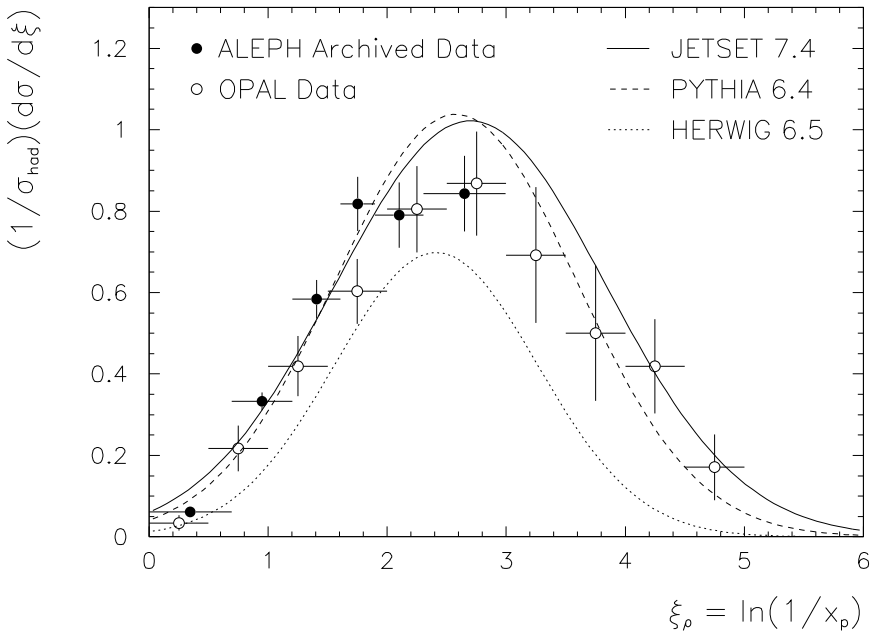

Figure 11.4: *Differential cross-section for the $\rho^{\pm}$ as a function of ξ_p. For comparision, OPAL data and the Monte Carlo models are shown as well. The errors shown are the quadratic sum statistical and systematic contributions.*

11.2 Summary

The inclusive production of the $\rho^{\pm}(770)$ vector meson in 3,239,746 selected hadronic Z decays has been studied. The results obtained from ALEPH data fits are presented and compared with the OPAL measurements and Monte Carlo predictions. $\rho^{\pm}$ mesons are reconstructed from the decay mode $\rho^{\pm} \rightarrow \pi^0 + \pi^{\pm}$ ($BR \approx 1$). The measurement covers a momentum interval of $x_p > 0.05$ and energy interval $x_E > 0.05$ where $x_p = p/p_{beam}$ and $x_E = E/p_{beam}$; these exclude $\sim 40\%$ of $\rho^{\pm}$s from measurement.

Charged track cuts and neutral pion selection via the Ranking method has been optimised to increase the signal significance of the $\rho^{\pm}$ meson.

Distortions in the invariant mass spectra caused by residual Bose-Einstein Correlations are found to be important in the extraction of $\rho^{\pm}$ rates from two pion invariant mass spectra. This effect is not included in the Monte Carlo programs. The Söding Model, used elsewhere [41] to describe background interference effects, appears to work well as a model of these distortions and is used successfully in this analysis.

The measured $\rho^{\pm}$ multiplicities and cross-sections are given in Tables 11.1 and 11.2, and the cross-sections are compared to Monte Carlo models in Figures 11.1 and 11.2 including a comparison to the OPAL meaurements in Figure 11.2.

11.3 Conclusion

Inclusive production of $\rho^{\pm}$ mesons in hadronic Z decays has been observed with the ALEPH detector after a suitable treatment of background and BECs. A Ranking method, to improve π^0 purity, is found significantly increase signal significance, and reduce partially reconstructed signal.

The measured differential cross-section of $\rho^{\pm}$ are in good agreement with OPAL measurements within the error bars. While the ALEPH analysis is unable to measure below $x_E = 0.05$, OPAL successfully measures down to $x_E = 0.016$. However, ALEPH provides a significantly more accurate measurement at high x_E (above $x_E = 0.3$). Except for HERWIG (default tuning), Monte Carlo rates obtained from ALEPH tuned JETSET and default tuned PYTHIA are consistent with real data measurements of the two independent experiments. The calculated total rate (2.59 per event) lies between the OPAL measurement (2.40 per event) and prediction of JETSET (2.77 per event).

For the ratio $2N(\rho^0)/N(\rho^{\pm})$ the predictions lie about one standard deviation from the measured value, PYTHIA giving the closest agreement.

The model for residual Bose-Einstein Correlations used in this analysis is the same as the OPAL experiment. This model successfully describes the distortion in two pion invariant mass spectra, that is dominated below 1 GeV/c^2.

11.4 Future Work

The skill and experiences gained from performing this Ph. D. study can be applied to future work in a number possible of areas:

- Particle production involving π^0 decay products where careful calibration and application of Ranking can improve on, or make possible new measurements at LEP and LHC.

- A measurement of $a_0^{\pm}(980) \rightarrow \eta\pi^{\pm}$, a decay that is difficult due to its low rate and large combinatorial background. Similar treatments of the π^0 can be made to η selection. Presently only OPAL has measured the $a_0^{\pm}$ at LEP with a poor accuracy, $N(a_0^{\pm}) = 0.27 \pm 0.11$.

- Bose-Einstein correlations have shown to be important at LEP where particle multiplicities are high. It is therefore important for Bose-Einstein correlations to be implemented correctly in Monte Carlo models. Much work needs to be done in this area.

While there are more possibilities for studies at LEP, the center of attention is now on LHC where pp collisions at $\sqrt{s} = 14$ TeV will soon begin. The possibility of the discovery of new physics is exciting, and, at least in the absence of new physics, there is an opportunity for the study of Standard Model in greater detail.

LIST OF REFERENCES

[1] S. Weinberg, *A Model of Leptons*, Phys. Rev. Lett. 19, 1264 (1967)

[2] A. Salam, *Elementary Particle Theory*, (1969)

[3] S.L. Glashow et al., *Weak Interactions with Lepton-Hadron Symmetry*, Phys. Rev. Lett. D2, 1285 (1970)

[4] S. Eidelman et al. *Review of Particle Physics*, Phys. Lett. B V592 1 (2004)

[5] G.D. Lafferty et al. *A compilation of inclusive particle production data in e^+e^- annihilation*, J.Phys.G.Nucl.Part.Phys: 21 A1-A151 (1995)

[6] *Statement on use of ALEPH data for long-term analyses* (`http://aleph.web.cern.ch/aleph/alpub/archive_data.pdf`)

[7] D. Buskulic et al. (ALEPH collab.), *Inclusive production of neutral vector mesons in hadronic Z decays*, Z. Phys. C 69, 379-392 (1996)

[8] K. Ackerstaff et al. (OPAL collab.), *Photon and light meson production in hadronic Z decays*, Eur. Phys. J. C 5, 411-437 (1998)

[9] W-M Yao et al. (Particle Data Group) J. Phys. G: Nucl. Part. Phys. 33 1 (2006) (`http://pdg.lbl.gov`)

[10] T. Sjöstrand, *The Lund Monte Carlo for jet fragmentation and e^+e^- physics - jetset version 6.2*, Comp. Phys. Comm. V39 347 (1986)

[11] R. D. Field and R. P. Feynman, *A Parameterization of the properties of Quark Jets*, Nucl. Phys. B136 1 (1978)

[12] T. Meyer, *A Monte Carlo model to produce baryons in e^+e^-*, Z. Phys. C12 77 (1982)

[13] B. Andersson et al., *Parton fragmentation and string dynamics*, Phys. Rep. V97 31 (1983)

[14] C. D. Buchanan and S. B. Chun, *Simple predictive model for flavor production in hadronization* Phys. Rev. Lett. 59, 1997 (1987)

[15] Yu. L. Dokshitzer, V. A. Khoze, S. I. Troyan, Sov. J. Nucl. Phys. 47 1384, (1988)

[16] G.D. Lafferty, *Residual Bose-Einstein Correleations in inclusive $\pi^+\pi^-$ systems and $\rho^0(770)$ line shape in Hadronic Z decays*, Z.Phys. C 60, 659-666 (1993)

[17] A. Heister, (ALEPH Collab.) *Two Dimensional Analysis of Bose-Einstein Correlations in Hadronic Z decays at LEP*, CERN-EP/2003-079 (2003)

[18] G. Lönnbard, *Modelling Bose-Einstein Correlations at LEP 2*, Eur. Phys. J. C 2, 165-180 (1998)

[19] O. Simirnova, *Tests of the JETSET Bose-Einstein Model in the e^+e^- annihiliation process*, arXiv:hep-ex/9808032 v1 (1998)

[20] Official web site of the CERN, `http://www.cern.ch`

[21] M. Banner et al., *Inclusive charged particle production at the CERN $p\overline{p}$ collider*, Physics Letters B V122 322 (1983)

[22] P. Bagnaia et al., *Evidence for $Z^0 \rightarrow e^+e^-$ ant the CERN $p\overline{p}$ collider*, Physics Letters B V129 130 (1983)

[23] D. Buskulic et al. (ALEPH Collab.), *Inclusive $\pi^\pm$, $K^\pm$ and $p\overline{p}$ differential cross-sections at the Z resonance*, Z. Phys. C66 355 (1995)

[24] D. Decamp et al., (ALEPH Collab.), *ALEPH: A detector for electron-positron annihilations at LEP*, Nucl. Instr. Meth. A294 121 (1990)

[25] D. Buskulic et al., (ALEPH Collab.), *Performance of the ALEPH Detector at LEP*, Nucl. Instr. Meth. A360 481 (1995)

[26] D. Schlatter, *ALEPH in Numbers*, ALEPH reports (1996)

[27] J. Knobloch and P. Norton, (ALEPH Collab.), *Status of Reconstruction Algorithms for ALEPH* Draft ALEPH notes.

[28] D. Buskulic et al. (ALEPH collab.), *First measurement of the quark-to-photon fragmentation function*, Z. Phys. C 69, 365-377 (1996)

[29] S. Schael (ALEPH Collab.), *Identification of low energetic converted photons in ALEPH* , ALEPH note 94-104 SOFTWE 94-008.

[30] A. Bencheikh, S. Schael (ALEPH Collab.), *B^* production in Z^0 decays*, ALEPH note 94-105 PHYSIC 94-090.

[31] D. Buskulic et al. (ALEPH Collab.), *Inclusive π^0 results*, Contribution to the 1995 International Europhysics Conference on High Energy Physics, Brussels, Belgium, 27/7 - 2/8 (1995)

[32] T. Sjöstrand, *High-energy-physics event generation with PYTHIA 5.7 and JETSET 7.4* Comp. Phys. Com. V82, 74-89 (1994)

[33] T. Sjöstrand, *ALEPH and OPAL Tuning of generators and models*, (`http://www.physics.carleton.ca/~ryh/opaltune/opal.html`)

[34] T. Sjöstrand, et al. *PYTHIA 6.4 physics and manual* J. High Energy Phys. 026 (2006)

[35] G. Corcella, *HERWIG 6.5*, JHEP 0101 010 (2001)

[36] CERN Program Library, long writeup W5013

[37] D. Parker. (ALEPH Collab.), *A study of Hadronic Events and the Measurement of α_s at the Z^0 Resonance.* PhD Thesis, University of Sheffield, UK. (1991)

[38] G. Batignani et al., *QPI0DO: Improvement in π^0 momentum resolution using the constraint of π^0 mass.* ALEPH note 93-095 PHYSIC 93-078.

[39] A. Rouge, *GAMPEX Calibration: On the reconstrunction of Photon Energy.* ALEPH note 94-57 PHYSIC 94-51 (1994)

[40] A. Beddall et al., *A Ranking Method for Neutral Pion Selection in High Multiplicity Hadronic Events*, Nucl. Instr. Meth. A 482 520-527 (2002)

[41] R.J. Apsimon et al., (OMEGA photon Collab.) *Comparison of photon and hadron induced production of ρ^0 mesons in the energy range of 65 to 175 GeV*, Z.Phys. C 53, 581-594 (1992)

[42] Y.I. Azimov et al., *Hump-backed QCD plateau in hadron spectra* Z. Phys. C 31 213 (1986)

APPENDIX A

π^0 FORMULAE

A.1 Two-Photon Invariant Mass Formula

Consider the decay process of the neutral pion, $\pi^0 \rightarrow \gamma_1 + \gamma_2$. Using natural units, the invariant mass of the photon pairs can be calculated from:

$$\begin{aligned} M^2 &= E^2 - p^2 \\ &= (E_1 + E_2)^2 - (\vec{p_1} + \vec{p_2})^2 \\ &= (E_1 + E_2)^2 - (p_{x_1} + p_{x_2})^2 - (p_{y_1} + p_{y_2})^2 - (p_{z_1} + p_{z_2})^2 \end{aligned} \quad (A.1)$$

where E_1 and E_2 are the energies of photons that can be found by:

$$E_i^2 = p_i^2 + m_\gamma^2 \quad (A.2)$$

here $i = 1, 2$ and $p_i^2 = p_{x_i}^2 + p_{y_i}^2 + p_{z_i}^2$. $p_{x,y,z}$ is the momentum components of sum of the photons. m_γ is assumed to be the mass of the photon, thus $m_\gamma = 0$. For the π^0 we can perform reconstruction from two photons. From the conservation of momentum:

$$\vec{p}_{\pi^0} = \vec{p} = \vec{p_1} + \vec{p_2} \quad (A.3)$$

Now we can find p^2 via A.3 and definition of dot product of two vectors:

$$\vec{p}.\vec{p} = p^2 = p_1^2 + p_2^2 + 2p_1 p_2 \cos\theta_{12} \quad (A.4)$$

where θ_{12} is the angle between two photons. γ_1 and γ_2 are assigned to zero mass, so $E = p$. Thus Equation A.4 becomes:

$$p^2 = E_1^2 + E_2^2 + 2E_1 E_2 \cos\theta_{12} \quad (A.5)$$

If we substitute the final result of p^2 into Equation A.1, then:

$$M^2 = 2E_1 E_2 (1 - \cos\theta_{12}) \quad (A.6)$$

We obtain measurements of E_1, E_2 and θ_{12} from the electromagnetic calorimeter.

A.2 π^0 Mass Resolution Formula

Mass resolution formula can be derived directly from the invariant mass relation. Equation A.6 can be re-arranged as follows:

$$M = \sqrt{2E_1E_2(1-\cos\theta_{12})} \tag{A.7}$$

If we assume that E_1, E_2 and θ_{12} are independent variables, then statistically the mass resolution σ_M can be found from:

$$\begin{aligned}\sigma_M &= \frac{\partial M}{\partial E_1}\sigma_{E_1} \oplus \frac{\partial M}{\partial E_2}\sigma_{E_2} \oplus \frac{\partial M}{\partial \theta_{12}}\sigma_{\theta_{12}} \\ &= \sqrt{\left(\frac{\partial M}{\partial E_1}\right)^2\sigma_{E_1}^2 + \left(\frac{\partial M}{\partial E_2}\right)^2\sigma_{E_2}^2 + \left(\frac{\partial M}{\partial \theta_{12}}\right)^2\sigma_{\theta_{12}}^2}\end{aligned} \tag{A.8}$$

where the square of partial derivatives are:

$$\begin{aligned}\left(\frac{\partial M}{\partial E_1}\right)^2 &= \left(\frac{2E_2(1-\cos\theta_{12})}{2\sqrt{2E_1E_2(1-\cos\theta_{12})}}\right)^2 = \frac{E_2(1-\cos\theta_{12})}{2E_1} \\ \left(\frac{\partial M}{\partial E_2}\right)^2 &= \left(\frac{2E_1(1-\cos\theta_{12})}{2\sqrt{2E_1E_2(1-\cos\theta_{12})}}\right)^2 = \frac{E_1(1-\cos\theta_{12})}{2E_2} \\ \left(\frac{\partial M}{\partial \theta_{12}}\right)^2 &= \left(\frac{2E_1E_2\sin\theta_{12}}{2\sqrt{2E_1E_2(1-\cos\theta_{12})}}\right)^2 = \frac{E_1E_2\sin^2\theta_{12}}{2(1-\cos\theta_{12})}\end{aligned} \tag{A.9}$$

One can set up the ratio σ_M/M, after substituting Equations A.9 into A.8.

$$\begin{aligned}\frac{\sigma_M}{M} &= \sqrt{\frac{\sigma_{E_1}^2}{4E_1^2} + \frac{\sigma_{E_2}^2}{4E_2^2} + \frac{\sigma_{\theta_{12}}^2}{4}\frac{\sin^2\theta_{12}}{(1-\cos\theta_{12})^2}} \\ &= \frac{1}{2}\sqrt{\frac{\sigma_{E_1}^2}{E_1^2} + \frac{\sigma_{E_2}^2}{E_2^2} + \frac{\sigma_{\theta_{12}}^2}{\tan^2(\theta_{12}/2)}} \\ &= \frac{1}{2}\left[\frac{\sigma_{E_1}}{E_1} \oplus \frac{\sigma_{E_2}}{E_2} \oplus \frac{\sigma_{\theta_{12}}}{\tan(\theta_{12}/2)}\right]\end{aligned} \tag{A.10}$$

The trigonometric expression in Equation A.10 can be transformed as follows:

$$\frac{\sin^2\theta_{12}}{(1-\cos\theta_{12})^2} = \frac{1-\cos^2\theta_{12}}{(1-\cos\theta_{12})^2} = \frac{(1-\cos\theta_{12})(1+\cos\theta_{12})}{(1-\cos\theta_{12})(1-\cos\theta_{12})} = \frac{1+\cos\theta_{12}}{1-\cos\theta_{12}}$$

Using half-angle formula, $\cos\beta = \cos^2(\beta/2) - \sin^2(\beta/2)$, we can write:

$$\frac{1+\cos\theta_{12}}{1-\cos\theta_{12}} = \frac{1+\cos^2(\theta_{12}/2)-\sin^2(\theta_{12}/2)}{1-\cos^2(\theta_{12}/2)+\sin^2(\theta_{12}/2)} = \frac{\cos^2(\theta_{12}/2)}{\sin^2(\theta_{12}/2)} = \frac{1}{\tan^2(\theta_{12}/2)}$$

Hence:

$$\frac{\sin^2\theta_{12}}{(1-\cos\theta_{12})^2} = \frac{1}{\tan^2(\theta_{12}/2)}$$

APPENDIX B

DESCRIPTION OF THE π^0 REFITTING METHODS

B.1 Refitting Low Energy π^0s

If we let ω_1, ω_2 be measured energies of the two photons, and $\theta_{\gamma\gamma}$ the opening angle between their directions, the reconstructed squared invariant mass of the π^0 is given by:

$$\mu^2 = 2\omega_1\omega_2(1 - \cos\theta_{\gamma\gamma}) \tag{B.1}$$

We can look for E_1 and E_2 minimising the chi-square form:

$$\chi^2 = \left(\frac{E_1 - \omega_1}{\sigma_1}\right)^2 + \left(\frac{E_2 - \omega_2}{\sigma_2}\right)^2 + \lambda(m^2 - 2E_1E_2(1 - \cos\theta_{\gamma\gamma})) \tag{B.2}$$

where σ_1 and σ_2 are the errors on the photon energies, m is the true π^0 mass and λ is the Lagrange Multiplicator (see Appendix B.3.1). We can minimise the χ^2 for E_1 and E_2 as:

$$E_1 = \omega_1 + (\frac{m^2 - \mu^2}{\mu^2}) \times \frac{\omega_1\omega_2}{\omega_1 + \omega_2} \tag{B.3}$$

$$E_2 = \omega_2 + (\frac{m^2 - \mu^2}{\mu^2}) \times \frac{\omega_1\omega_2}{\omega_1 + \omega_2} \tag{B.4}$$

These equations are used in our computer program to re-define the photon energies. Then, we evaluate again the π^0 invariant mass and iterate until nominal mass π^0 within $\pm$ 0.0001 MeV/c^2. Usually only 2 or 3 iterations are needed. Note that, no effects of σ_1 and σ_2 are shown in equations B.3 and B.4 because $\sigma_{1,2} = R\sqrt{(E_{1,2})}$ where R is the resolution parameter of the ECAL.

B.2 Refitting High Energy π^0s

At high energy, the angular resolution is no longer negligible compared to the energy resolution, and one has to take it into account in the fitting procedure.

Therefore, in this case one must be minimise the chi-square form:

$$\chi^2 = (\frac{E_1 - \omega_1}{\sigma_1})^2 + (\frac{E_2 - \omega_2}{\sigma_2})^2 + (\frac{\cos\theta_{\gamma\gamma} - K}{\sigma_{\cos\theta_{\gamma\gamma}}})^2 \tag{B.5}$$

with the mass constraint on the opening angle

$$M^2_{\pi^0} = 2E_1E_2(1 - K) \tag{B.6}$$

Here the fitted parameters are E_1 and E_2, the best evaluation of the energies of the photons; other parameter K, which is the best evaluation of the cosine of the opening angle, is obtained from the π^0 mass constrained. The minimisation is performed by the Newtonian Method which is described in Section B.3.2.

B.3 Multidimensional Optimisation

B.3.1 The Method of Lagrange Multipliers

A method for obtaining the relative maximum or minimum values of a function $F(x, y, z)$ subjected to a constraint condition $\phi(x, y, z) = 0$, consists of the formation of the auxiliary function:

$$G(x, y, z) = F(x, y, z) + \lambda\phi(x, y, z) \tag{B.7}$$

subject to the conditions:

$$\frac{\partial G}{\partial x} = 0, \frac{\partial G}{\partial y} = 0, \frac{\partial G}{\partial z} = 0 \tag{B.8}$$

which are necessary conditions for relative maximum or minimum. The parameter λ, which is independent of x, y, z, is called a *Lagrange Multiplier*.

The method can be generalised. If we wish to find the relative maximum or minimum values of a function $F(x_1, x_2, x_3, \ldots, x_n)$ subject to the constraint conditions $\phi_1(x_1, \ldots, x_n) = 0$, $\phi_2(x_1, \ldots, x_n) = 0$,... , $\phi_k(x_1, \ldots, x_n) = 0$, we form the auxiliary function:

$$G(x_1, x_2, \ldots, x_n) = F + \lambda_1\phi_1 + \lambda_2\phi_2 + \cdots + \lambda_k\phi_k \tag{B.9}$$

subject to the (necessary) conditions:

$$\frac{\partial G}{\partial x_1} = 0, \frac{\partial G}{\partial x_2} = 0, \ldots, \frac{\partial G}{\partial x_n} = 0 \tag{B.10}$$

where λ_1, λ_2, ..., λ_k, which are independent of x_1,x_2, ..., x_n, are the Lagrange Multipliers.

B.3.2 The Newtonian Method

The Newton-Raphson method is an open method that finds the roots x of a function such that $f(x) = 0$. Taylor's expansion about $x = x_i$ gives:

$$x_{i+1} \approx x_i - \frac{f(x_i)}{f'(x_i)} \tag{B.11}$$

A similar open approach can be used to find an optimum of $f(x)$ by defining a new function, $g(x) = f'(x)$. Thus because the same optimal value x^* satisfies both $g(x^*) = f'(x^*) = 0$. We can use the following:

$$x_{i+1} \approx x_i - \frac{f'(x_i)}{f''(x_i)} \tag{B.12}$$

as a technique to find the maximum or minimum of $f(x)$.

This method can be extended to multivariate cases. Write a second order Taylor series for $f(\mathbf{x})$ near $\mathbf{x} = \mathbf{x}_i$,

$$f(\mathbf{x}) = f(\mathbf{x}_i) + \nabla f^T(\mathbf{x}_i)(\mathbf{x} - \mathbf{x}_i) + \frac{1}{2}(\mathbf{x} - \mathbf{x}_i)^T H_i(\mathbf{x} - \mathbf{x}_i) \tag{B.13}$$

where H is the Hessian matrix. Hessian of f is evaluated from:

$$Hf(x_1, x_2, \ldots, x_n) = \begin{vmatrix} \frac{\partial^2 f}{\partial x_1^2} & \frac{\partial^2 f}{\partial x_1 \partial x_2} & \frac{\partial^2 f}{\partial x_1 \partial x_3} & \cdots & \frac{\partial^2 f}{\partial x_1 \partial x_n} \\ \frac{\partial^2 f}{\partial x_2 \partial x_1} & \frac{\partial^2 f}{\partial x_2^2} & \frac{\partial^2 f}{\partial x_2 \partial x_3} & \cdots & \frac{\partial^2 f}{\partial x_2 \partial x_n} \\ \frac{\partial^2 f}{\partial x_3 \partial x_1} & \frac{\partial^2 f}{\partial x_3 \partial x_2} & \frac{\partial^2 f}{\partial x_3^2} & \cdots & \frac{\partial^2 f}{\partial x_3 \partial x_n} \\ \vdots & \vdots & \vdots & \ddots & \vdots \\ \frac{\partial^2 f}{\partial x_n \partial x_1} & \frac{\partial^2 f}{\partial x_n \partial x_2} & \frac{\partial^2 f}{\partial x_3 \partial x_n} & \cdots & \frac{\partial^2 f}{\partial x_n^2} \end{vmatrix} \tag{B.14}$$

At the minimum:

$$\frac{\partial f(\mathbf{x})}{\partial \mathbf{x}_j} = 0 \quad (\text{for } j = 1, 2, 3, \ldots, n)$$

Thus,

$$\nabla f = \nabla f(\mathbf{x}_i) + H_i(\mathbf{x} - \mathbf{x}_i) = 0 \tag{B.15}$$

if H is nonsingular:

$$\mathbf{x}_{i+1} = \mathbf{x}_i - H_i^{-1} \nabla f \tag{B.16}$$

which can be shown to converge quadratically near the optimum.

APPENDIX C

π^0 MATCHING

Matching reconstructed π^0 candidates to the generated π^0s is done on a spatial basis, taking advantage of the high granularity of the ECAL. The energy resolution is relatively poor and so the energy measurements are not used in the procedure. The procedure, which considers only selected π^0 candidates, is as follows:

1. Each photon, R_1 and R_2, from a reconstructed π^0 is presented with photons, G_1 and G_2, from a generated π^0.

2. The opening angles, α_{RG}, between the reconstructed photons and generated photons is calculated. Four combinations are possible: α_{11}, α_{12}, α_{21}, and α_{22}.

3. From these angles two sums are calculated: $\beta_a = \alpha_{11} + \alpha_{22}$, and $\beta_b = \alpha_{12} + \alpha_{21}$, representing the two possible matching orientations. The orientation, a or b, giving the smallest value of β is taken as the match.

4. The above procedure is repeated until all generated π^0s have been presented to the reconstructed π^0. The candidate with the smallest value of β is flagged the best matching candidate.

5. Finally the best matching candidates, one for each reconstructed π^0, are flagged as a true match if the value of β is less than 1.4°.

In Figure C.1 distributions of $\lambda = 1000\,(1 - \cos\beta)$ are shown in four energy intervals for best and all matches. A clear spike is seen for low values of λ where true matches are expected to be found. At higher values of λ a background appears corresponding to the incorrect orientation of true matching π^0s, the background becomes closer to the spike for higher energy π^0s due to the smaller opening angles. These features demonstrate the spatial resolving power of the

ECAL, for example photons are clearly resolved to much better than a λ value of $0.3 = 1.4°$.

A cut of $\lambda < 0.3 = 1.4°$ is applied to a π^0 candidate to flag it as a true match. A continuum extends to large values of λ representing the matching of generated π^0s to fake reconstructed π^0s. It is this continuum which forms the background to correctly matched π^0s and therefore is responsible for the uncertainties in the matching procedure. The chosen value of λ is an attempt to minimise the background whilst keeping all the correctly matched π^0s. An additional problem occurs for very high energy π^0s where the opening angles are very small. For these the background begins to merge with the spike and the matching becomes ambiguous. To eliminate this problem an upper limit of 18 GeV is placed on the selection of π^0 candidates.

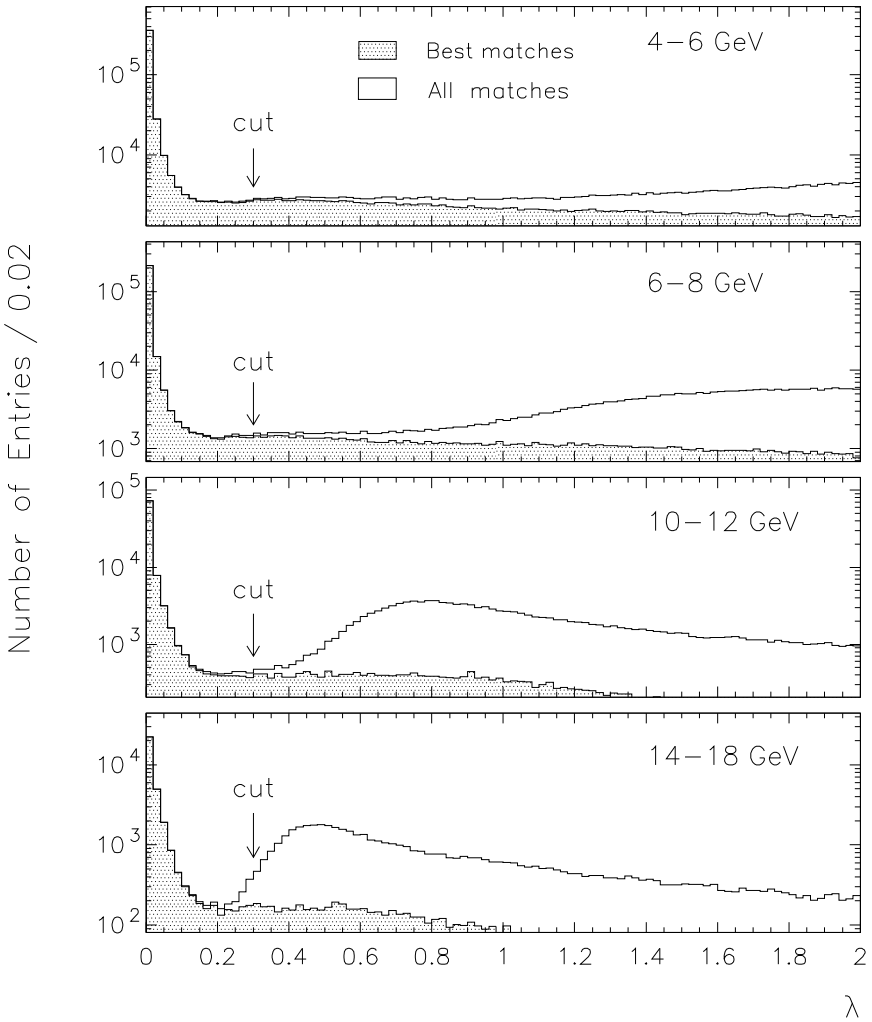

Figure C.1: *The distribution of* $\lambda = 1000\,(1 - \cos\beta)$ *in four energy intervals for the all and best matches. A cut of* $\lambda < 0.3 = 1.4°$ *is applied to a* π^0 *candidate to flag it as a true match.*

APPENDIX D

DETAILED REAL DATA FITS

The detail of the fit components contributing $\pi^0\pi^\pm$ invariant mass spectra and corresponding extracted signal and interference functions for all x_p and x_E intervals are shown in Figures from D.1 to D.4.

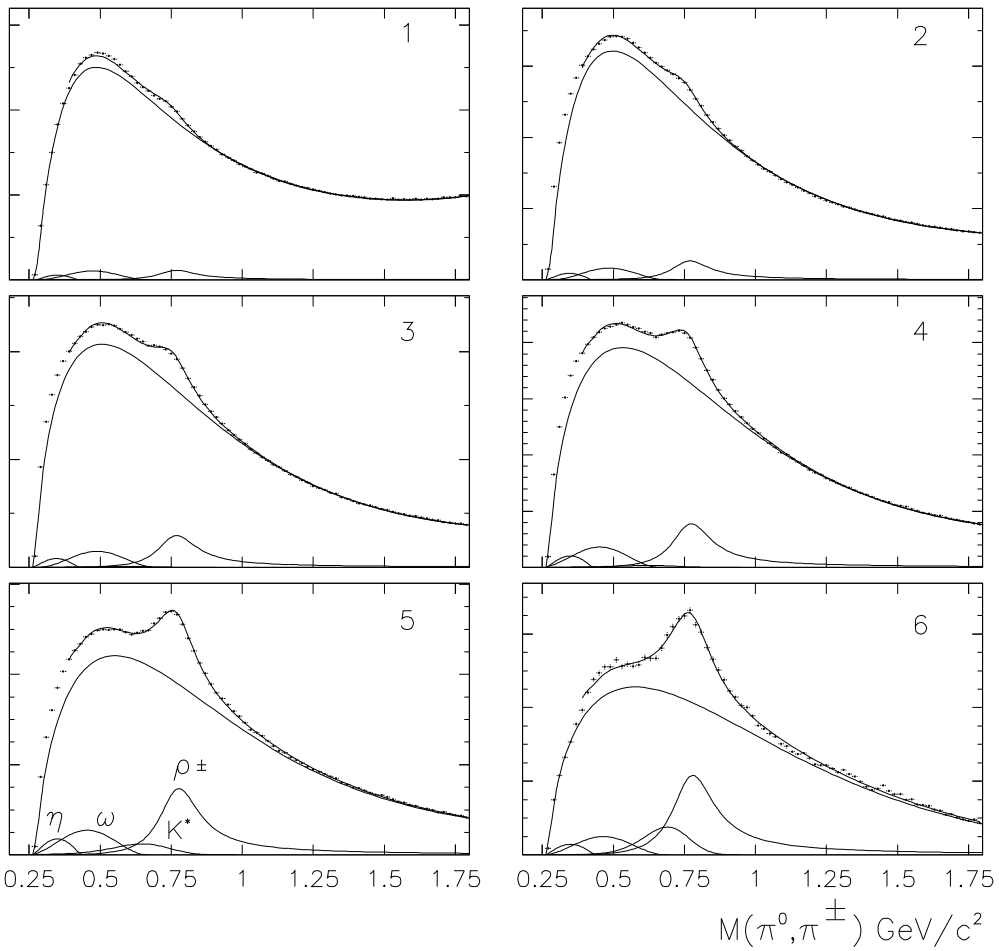

Figure D.1: *Fits made to the real data invariant mass spectra for all x_p intervals and the detail of the fit components.*

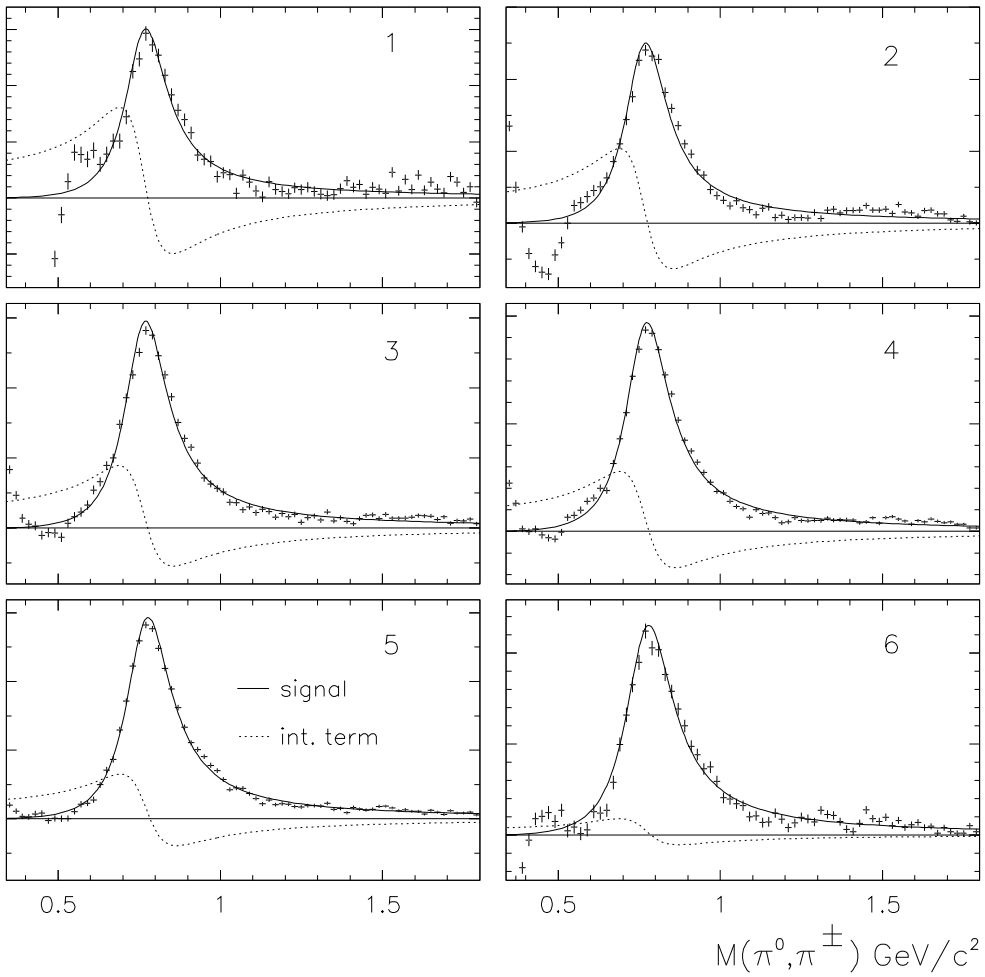

Figure D.2: *The extracted signal, resonance curve and interference term for all x_p intervals corresponding to the data in Figure D.1.*

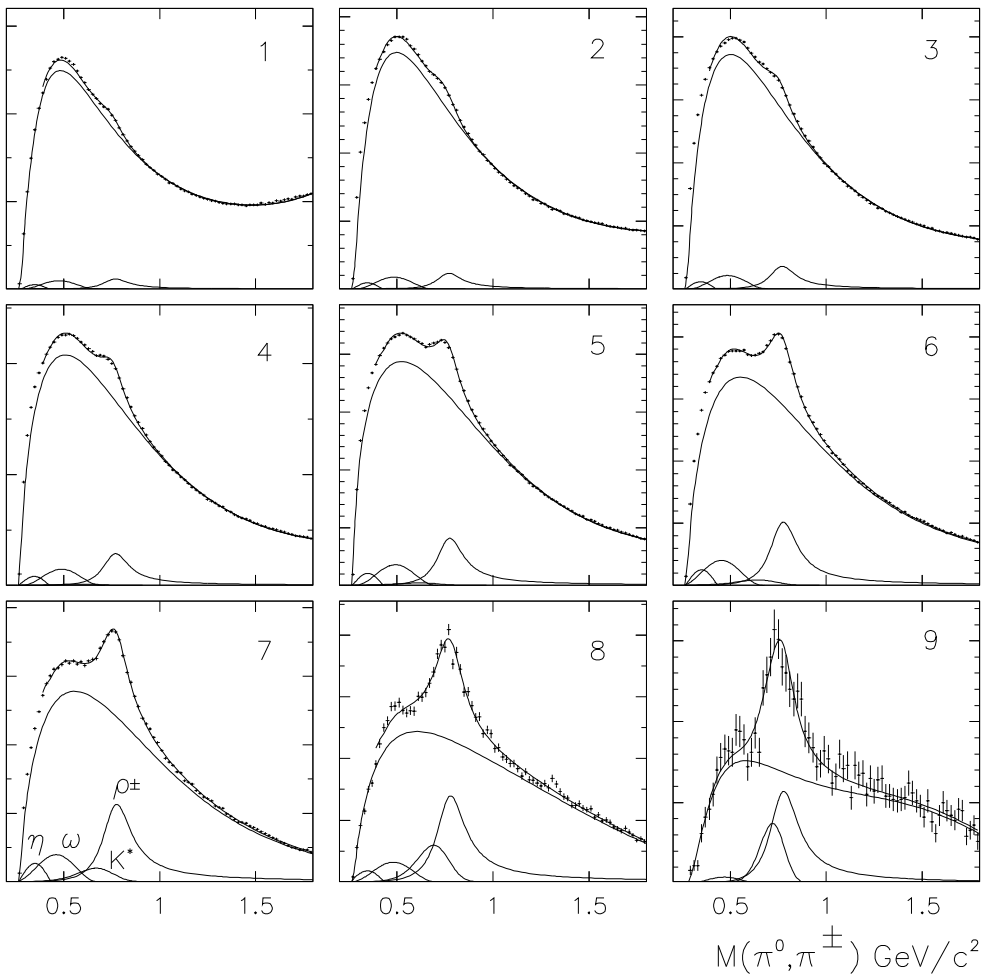

Figure D.3: *Fits made to the real data invariant mass spectra for all x_E intervals and the detail of the fit components.*

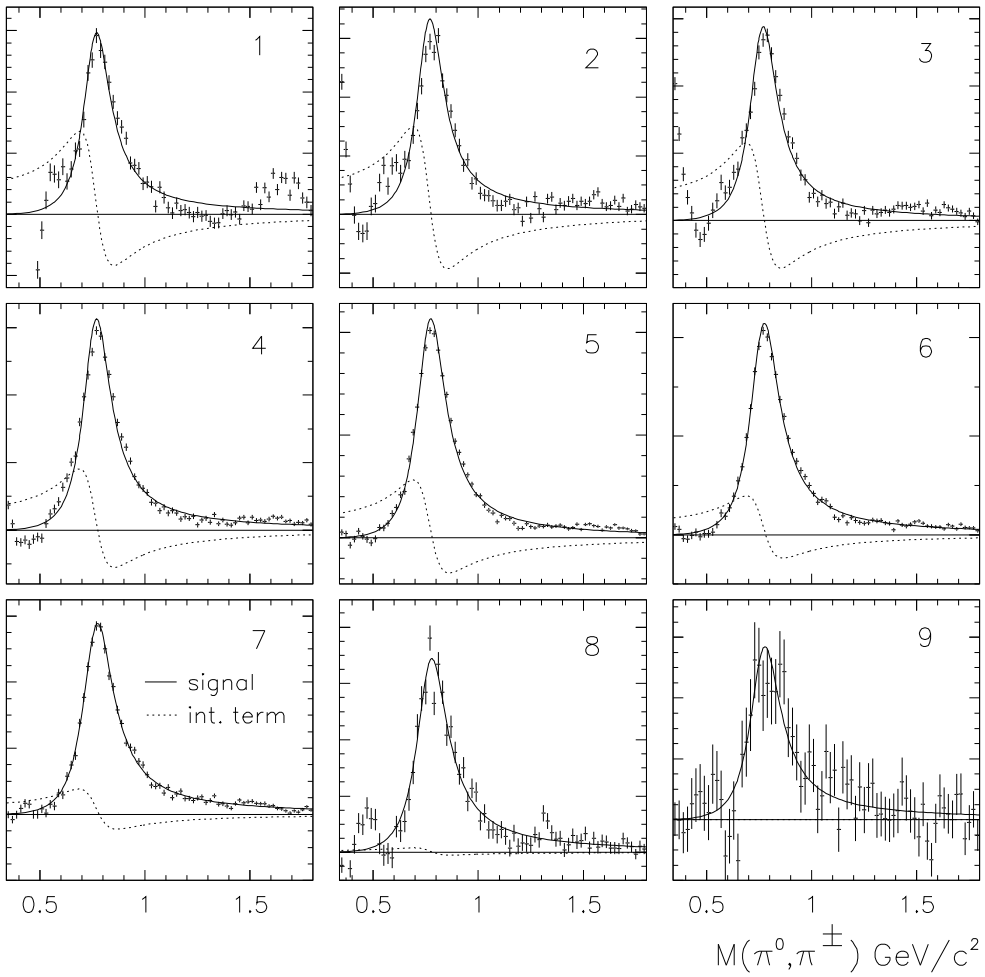

Figure D.4: *The extracted signal, resonance curve and interference term for all x_p intervals corresponding to the data in Figure D.3.*